Ladderane phospholipids form a densely packed membrane with normal hydrazine and anomalously low proton/hydroxide permeability

Frank R. Moss III[a,1], Steven R. Shuken[a,1], Jaron A. M. Mercer[a], Carolyn M. Cohen[a], Thomas M. Weiss[b], Steven G. Boxer[a,2], and Noah Z. Burns[a,2]

[a]Department of Chemistry, Stanford University, Stanford, CA 94305; and [b]Stanford Synchrotron Radiation Laboratory, Stanford Linear Accelerator Center, Stanford University, Menlo Park, CA 94025

Contributed by Steven G. Boxer, July 30, 2018 (sent for review June 24, 2018; reviewed by Erick Carreira and Marjorie Longo)

Ladderane lipids are unique to anaerobic ammonium-oxidizing (anammox) bacteria and are enriched in the membrane of the anammoxosome, an organelle thought to compartmentalize the anammox process, which involves the toxic intermediate hydrazine (N_2H_4). Due to the slow growth rate of anammox bacteria and difficulty of isolating pure ladderane lipids, experimental evidence of the biological function of ladderanes is lacking. We have synthesized two natural and one unnatural ladderane phosphatidylcholine lipids and compared their thermotropic properties in self-assembled bilayers to distinguish between [3]- and [5]-ladderane function. We developed a hydrazine transmembrane diffusion assay using a water-soluble derivative of a hydrazine sensor and determined that ladderane membranes are as permeable to hydrazine as straight-chain lipid bilayers. However, pH equilibration across ladderane membranes occurs 5–10 times more slowly than across straight-chain lipid membranes. Langmuir monolayer analysis and the rates of fluorescence recovery after photobleaching suggest that dense ladderane packing may preclude formation of proton/hydroxide-conducting water wires. These data support the hypothesis that ladderanes prevent the breakdown of the proton motive force rather than blocking hydrazine transmembrane diffusion in anammox bacteria.

ladderane | anammox | lipid bilayer | proton permeability | membrane structure

Lipid membranes are universal features of living systems. Along with membrane proteins, they form the internal and peripheral barriers of cells and organelles and maintain nonequilibrium states necessary for life. Cells produce a diverse array of lipid structures and expend considerable energy to tightly control the lipid compositions of their membranes (1). In conventional phospholipid bilayers, it is known that longer hydrocarbon tails and fewer degrees of unsaturation reduce fluidity and slow lateral diffusion, as well as affecting phase behavior (Fig. 1*A*) (2, 3). However, the physical properties and biological functions of lipids with unconventional structures (*SI Appendix*, Fig. S1) are mostly unexplored.

The ladderane lipids, containing lipid tails terminating in either a [3]-ladderane motif (highlighted in blue in Fig. 1*B*) or a [5]-ladderane motif (highlighted in red in Fig. 1*B*), occur uniquely in anaerobic ammonium-oxidizing (anammox) bacteria and are some of the most structurally exotic lipids known (4–9). Anammox bacteria are not available as a pure culture, and enrichment cultures have doubling times of 1–2 wk (10, 11). Isolation of lipids from anammox enrichment cultures yields a complex and inseparable mixture, preventing biophysical characterization of individual ladderane species (12, 13). To enable experiments on ladderane lipids, we developed de novo enantioselective chemical syntheses of both [3]- and [5]-ladderane lipid tails and ladderane phospholipids (14). We prepared a [5]-ladderane–[3]-ladderane phosphatidylcholine (**[5]\[3]PC**; Fig. 1*B*) and a di-[3]-ladderane phosphatidylcholine (**[3]\[3]PC**; Fig. 1*B*), two of the most common ladderane phospholipids across a range of anammox genera (8). Additionally, we prepared di-[5]-ladderane phosphatidylcholine (**[5]\[5]PC**; Fig. 1*B*), which is not known to occur naturally.

Ladderanes are enriched in the membrane of the anammoxosome, a specialized organelle within which anammox catabolism is thought to occur (4). Ammonium and nitrite are coupled to produce dinitrogen via intermediate hydrazine (N_2H_4); oxidation of hydrazine to dinitrogen is highly exergonic, and this free energy is believed to be harnessed to pump protons across the anammoxosome membrane (15–17). The resulting pH gradient of ∼1 unit in turn powers ATP synthesis (Fig. 1*C*) (18–20). Hydrazine's cellular toxicity and bioenergetic value as a metabolic intermediate have led to the hypothesis that ladderanes serve to prevent the diffusion of hydrazine out of the anammoxosome, thereby protecting the contents of the riboplasm and periplasm from free hydrazine while preserving metabolic energy (4, 20). It has also been reasoned, based on long anammox doubling times and slow hydrazine synthase activity, that ladderanes might prevent the passive diffusion of protons out of the anammoxosome to preserve the proton motive force necessary for ATP synthesis (4, 21). Another theoretical study suggests ladderanes might trap reactive species such as free radicals in addition to protons (22). Although studies on enrichment cultures and lipid extracts suggest

Significance

Ladderane lipids represent exotic natural products containing highly strained, concatenated cyclobutane rings, a motif that has not been found in any other natural products. These lipids are exclusively found in bacteria that carry out anaerobic ammonium oxidation (anammox), suggesting a biological role in the anammox process. The relationship between molecular structure and this metabolism remains unexplored due to a lack of natural lipid material to study. We use an efficient chemical synthesis to create large quantities of pure ladderane lipids for biophysical analysis. This analysis reveals some unusual properties of membranes composed of ladderane lipids. Significantly, ladderane membranes have low proton permeability, which would slow the breakdown of the proton gradient used to synthesize ATP during the slow anammox metabolism.

Author contributions: F.R.M., S.R.S., J.A.M.M., S.G.B., and N.Z.B. designed research; F.R.M., S.R.S., J.A.M.M., C.M.C., and T.M.W. performed research; F.R.M., S.R.S., J.A.M.M., C.M.C., and T.M.W. contributed new reagents/analytic tools; F.R.M., S.R.S., J.A.M.M., T.M.W., S.G.B., and N.Z.B. analyzed data; and F.R.M., S.R.S., S.G.B., and N.Z.B. wrote the paper.

Reviewers: E.C., ETH Zurich; and M.L., University of California, Davis.

The authors declare no conflict of interest.

[1]F.R.M. and S.R.S. contributed equally to this work.

[2]To whom correspondence may be addressed. Email: sboxer@stanford.edu or nburns@stanford.edu.

This article contains supporting information online at www.pnas.org/lookup/suppl/doi:10.1073/pnas.1810706115/-/DCSupplemental.

Published online August 27, 2018.

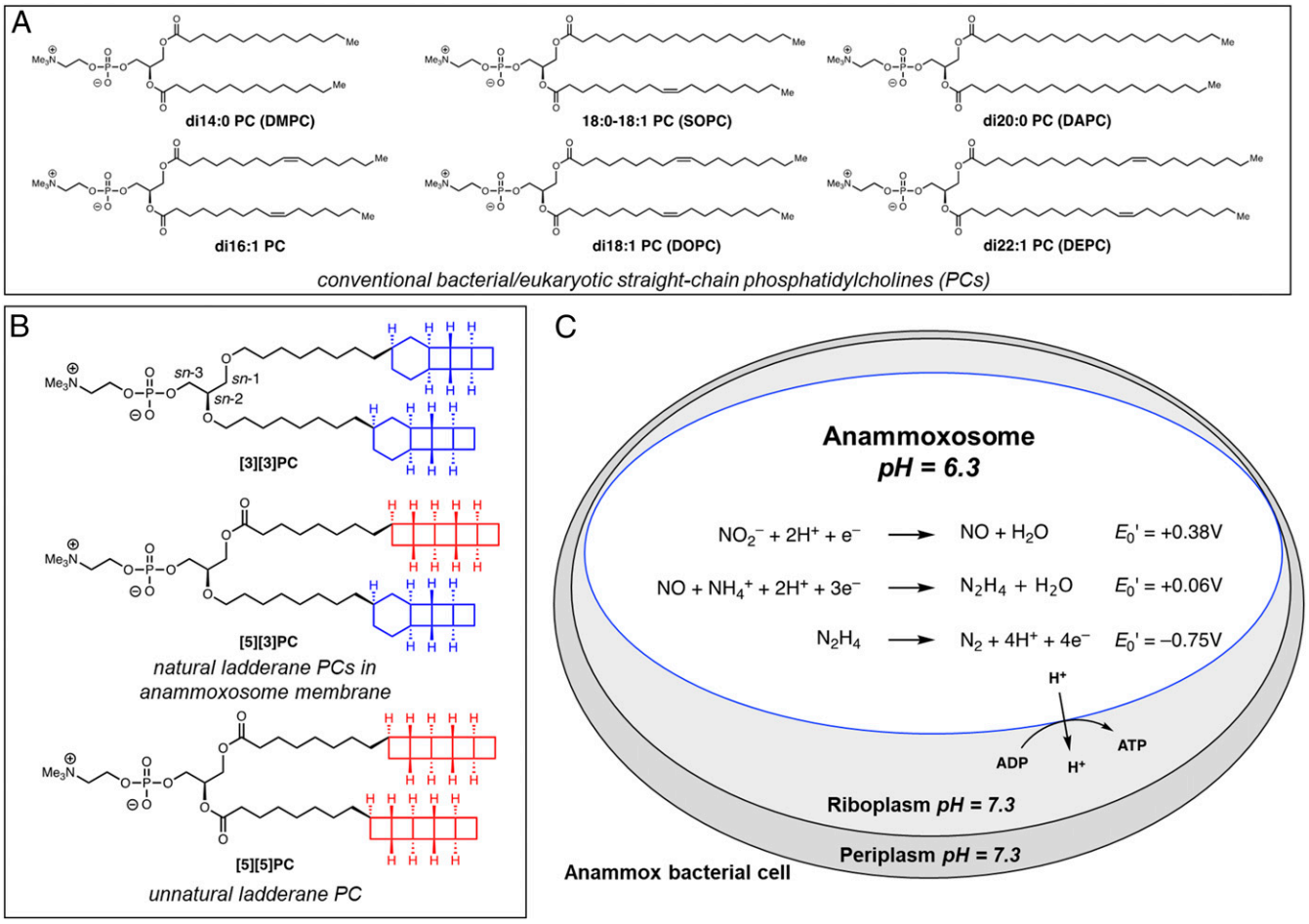

Fig. 1. Lipid structures and anammox metabolism. (*A*) Representative straight-chain PCs. Nomenclature: x:y is a straight chain with x carbons and y degrees of unsaturation. (*B* and *C*) Ladderane lipids such as **[3][3]PC** and **[5][3]PC** occur in the anammoxosome membrane of anammox bacteria. (*B*) **[3][3]PC** and **[5][3]PC** phospholipids and unnatural analog **[5][5]PC** that have been prepared by enantioselective chemical synthesis. (*C*) Anammox catabolism is believed to provide energy to the cell by oxidizing the toxic intermediate hydrazine (N_2H_4). Hydrazine oxidation is thought to be coupled to proton influx, generating a pH gradient that drives ATP synthesis. Standard reduction potentials, E_0', for redox half reactions are shown.

that the anammoxosome membrane is dense and relatively impermeable to dyes, hypotheses about hydrazine and proton permeability remain to be experimentally tested (4, 12). We recently completed the total synthesis of a ladderane phospholipid, which we expand in this work to a total of three phospholipids with distinct tail structures for structure–function studies (14). Biophysical experiments on model membranes composed of these synthetic lipids allow us to identify properties of individual molecular ladderane species.

Results

Syntheses of Ladderane PCs. We recently reported enantioselective total syntheses of a [5]-ladderane fatty acid and a [3]-ladderane fatty alcohol (14). These lipid tails were then elaborated to **[5][3]PC**, **[3][3]PC**, and **[5][5]PC** using a modification of our previously reported phosphatidylcholine synthetic route (*SI Appendix*, Schemes S1–S3).

Differential Scanning Calorimetry. Lipid films were hydrated with a low-melting and high-boiling 1:1 ethylene glycol/phosphate buffer mixture, and differential scanning calorimetry (DSC) was performed to measure the transition temperature (T_m) of the multilamellar lipid dispersions. Control experiments showed that the effect of ethylene glycol on T_m is negligible (*SI Appendix*, Table S1). A single transition between −40 and 80 °C was observed for each ladderane PC. The presence of a [3]-ladderane tail at the *sn*-2 position apparently ensures a low T_m (compare **[5][3]PC**, T_m = 11.8 °C to **[5][5]PC**, T_m = 68.4 °C; Fig. 2*A*). We believe the cyclohexane ring in the [3]-ladderane motif introduces a kink in the lipid tail, mirroring the fluidizing effect of *cis*-unsaturation in the *sn*-2 position tail of a straight-chain lipid [compare 18:0–18:1 PC (SOPC), T_m = 4.1 °C to di18:0 PC (DSPC), T_m = 57.1 °C]; **[5][5]PC** has approximately the same T_m as di20:0 PC (DAPC).

Self-Assembly of Ladderane Phospholipids into Lipid Bilayers. We next evaluated whether ladderane PCs would self- assemble into giant unilamellar vesicles (GUVs) using established methods (23–25). Upon gentle hydration, films of **[3][3]PC** and **[5][3]PC** appeared to form GUVs (Fig. 2 *B* and *C*) with homogeneous incorporation of dye [0.1 mol % Texas Red-DHPE (TR-DHPE)] and spherical shapes confirming that these lipids form fluid bilayers at room temperature. Formation of GUVs from **[5][5]PC** required heating above its T_m, and upon cooling we observed fluorescent objects similar to gel-phase GUVs formed from DAPC (Fig. 2*D* and *SI Appendix*, Fig. S3 *A* and *B*). A 1:1 mixture of **[3][3]PC** and **[5][5]PC** formed GUVs with visible domains that exclude TR-DHPE (Fig. 2*E*) in a manner analogous to mixtures of straight-chain phospholipids that form coexisting phases at room temperature (26). Hydration of **[3][3]PC** or

A Lipid	T_m (°C)
di18:2 PC	-52.7 ± 1.6
di16:1 PC	-33.0 ± 0.1
di18:1 PC (DOPC)	-10.9 ± 0.1
16:0-18:1 PC (POPC)	-4.8 ± 0.1
18:0-18:1 PC (SOPC)	4.1 ± 0.1
di22:1 PC (DEPC)	15.8 ± 0.1
di14:0 PC (DMPC)	24.3 ± 0.1
di18:0 PC (DSPC)	57.1 ± 0.1
di20:0 PC (DAPC)	67.8 ± 0.1
[5][3]PC	11.8 ± 0.2
[3][3]PC	15.2 ± 0.1
[5][5]PC	68.4 ± 0.1

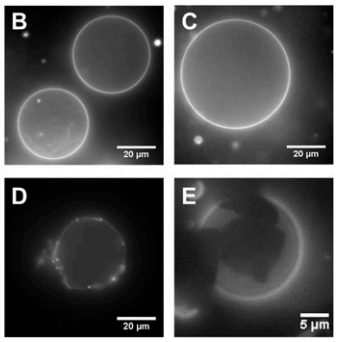

Fig. 2. Transition temperatures and formation of GUVs. (*A*) T_ms of aqueous lamellar dispersions of PCs in 1:1 ethylene glycol/NaH_2PO_4 buffer measured by DSC. (*B–E*) Fluorescence microscope images of GUVs (TR-DHPE or DiI, 0.1 mol %) in 500 mM sucrose. For additional images see *SI Appendix*, Fig. S3. (*B*) **[3][3]PC**, (*C*) **[5][3]PC**, (*D*) **[5][5]PC**, (*E*) 1:1 **[3][3]PC**:**[5][5]PC**.

[5][3]PC films followed by extrusion through a 50-nm-pore polycarbonate membrane resulted in the formation of small unilamellar vesicles (SUVs) (*SI Appendix*, Table S3).

Hydrazine Transmembrane Diffusion Assay. To test the hypothesis that ladderanes form a barrier to transmembrane diffusion of hydrazine, we developed an assay based on a small-molecule sensor that fluoresces upon condensation with hydrazine (27). We prepared a derivative with added hydrophilic sulfonate and amide groups to improve aqueous solubility and presumably reduce interactions between the dye and the membrane (*SI Appendix*, Figs. S4–S11 and Schemes S4–S6); the final hydrazine sensor (**HS**)-based hydrazine transmembrane diffusion kinetic assay design is illustrated in Fig. 3*A* (28). We also confirmed that HS does not localize in lipid bilayers (*SI Appendix*, section 9).

We performed this hydrazine diffusion assay on SUVs composed of several straight-chain PCs, **[3][3]PC**, and **[5][3]PC**. SUVs encapsulating **HS** in a pH = 7.4 phosphate buffer were added to an equiosmolar pH = 7.4 buffer containing hydrazine, and changes in the fluorescence intensity were measured (Fig. 3*B*). Among straight-chain PCs, hydrazine transmembrane diffusion rates depended strongly on hydrophobic tail length (Fig. 3*C*), likely due to different bilayer thicknesses among these lipids (29–31). SUVs of ladderane PCs exhibited half-lives ($t_{1/2}$s) of hydrazine transmembrane diffusion well within the range exhibited by SUVs of straight-chain PCs. We have also conducted this diffusion assay at the anammoxosome-relevant pH of 6.3 with SOPC, di22:1 PC (DEPC), and **[3][3]PC**. Transmembrane diffusion rates are all slower, as expected, but maintain the same trend as at pH = 7.4 (*SI Appendix*, section 10).

Small-Angle X-Ray Scattering. To examine the relationship between hydrazine diffusion rate and bilayer thickness, we performed small angle X-ray scattering (SAXS) on rigorously extruded SUVs of unsaturated straight-chain PCs and ladderane PCs (Fig. 3*C*). Bilayers of straight-chain PCs increased in thickness with increasing chain length from 3.25 nm for di16:1 PC to 4.37 nm for di22:1 PC. The [3]-ladderane and [5]-ladderane tails in our synthetic ladderane phospholipids each contain 20 carbons, and **[3][3]PC** and **[5][3]PC** formed bilayers of about the same thickness as di20:1 PC (~4 nm). SAXS curves also confirmed the high level of unilamellarity of SUVs (see discussion in *SI Appendix*, section 12).

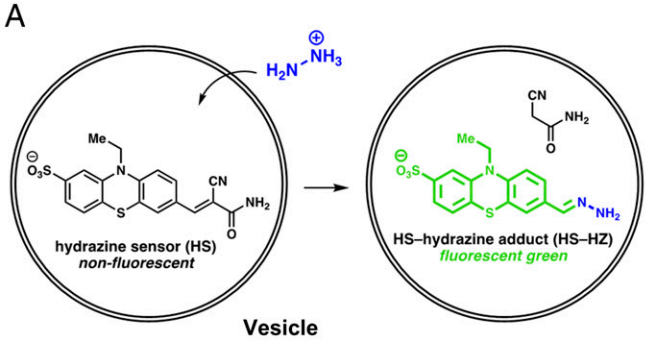

C Lipid	N_2H_4 Diff. $t_{1/2}$ (min)	Bilayer Thickness (nm)
di18:2 PC	23.0 ± 0.9	--
di16:1 PC	23.0 ± 2.7	3.25 ± 0.004
di18:1 PC (DOPC)	54.4 ± 5.6	3.53 ± 0.006
18:0-18:1 PC (SOPC)	50.5 ± 0.5	--
di20:1 PC	--	3.96 ± 0.005
di22:1 PC (DEPC)	98.9 ± 6.0	4.37 ± 0.004
[5][3]PC	47.4 ± 0.9	3.98 ± 0.008
[3][3]PC	71.5 ± 2.0	4.00 ± 0.007

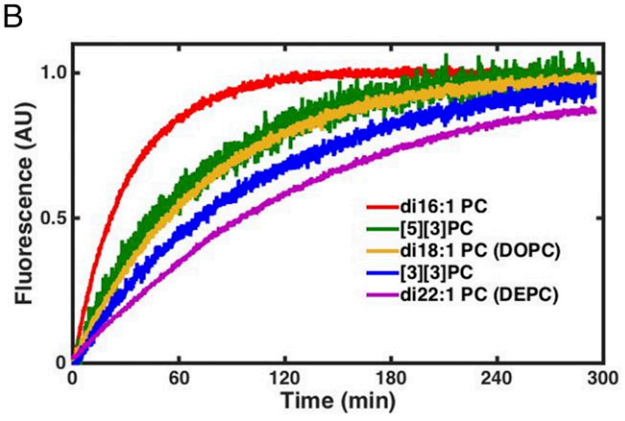

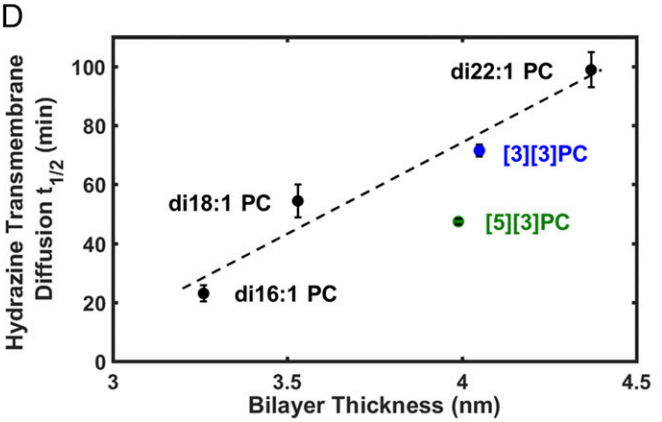

Fig. 3. Hydrazine transmembrane diffusion assay and bilayer thickness as estimated by SAXS. (*A*) Illustration of N_2H_4 transmembrane diffusion assay using a water-soluble derivative (**HS**) of a fluorogenic hydrazine sensor. (*B*) Hydrazine transmembrane diffusion curves for representative straight-chain and ladderane PCs. (*C*) Table of hydrazine transmembrane diffusion half-lives and bilayer thicknesses. (*D*) Hydrazine transmembrane diffusion half-life vs. bilayer thickness. Dashed line illustrates linear correlation for di16:1 PC, di18:1 PC, di22:1 PC, and **[3][3]PC**.

pH Equilibration Across Membranes. To test the hypothesis that ladderanes form a barrier to transmembrane diffusion of protons/hydroxide ions, we performed a carboxyfluorescein (CF)-based assay of pH equilibration (Fig. 4*A*) on SUVs of several straight-chain PCs, **[3][3]PC**, and **[5][3]PC** (32). SUVs encapsulating CF at pH = 7.2 in bis-Tris propane buffer were added to equiosmolar pH = 5.8 bis-Tris propane buffer, creating a transmembrane pH gradient that spontaneously decayed over time. The decrease in CF fluorescence was used to monitor the decrease in pH inside the SUVs as protons/hydroxide ions equilibrated across the bilayers. We also performed control experiments with valinomycin to confirm that a buildup of membrane potential was not affecting relative pH equilibration rates and with gramicidin to confirm that vesicles were unilamellar. We confirmed that valinomycin inserts into ladderane bilayers with the fluorescent K^+ sensor PBFI (*SI Appendix*, section 13) (33). Equilibration of pH across **[3][3]PC** and **[5][3]PC** bilayers was approximately an order of magnitude slower than across membranes composed of straight-chain PCs (48–75 min vs. 0.33–6.9 min $t_{1/2}$) (Fig. 4 *B* and *C*). We observe a correlation between T_m and pH equilibration $t_{1/2}$ for straight-chain PCs; however, **[5][3]PC** and **[3][3]PC** deviate from this trend, suggesting that unique intermolecular interactions between ladderane lipid tails affect rates of pH equilibration (Fig. 4*D*). These interactions remain present in a mixture of **[3][3]PC** with 16:0–18:1 PC (POPC) as indicated by a pH equilibration $t_{1/2}$ of 31 min (*SI Appendix*, section 13).

Pressure-Area Isotherms of Langmuir Monolayers. To help explain the low proton/hydroxide permeability of ladderane PC bilayers, we investigated the physical properties of PC monolayers at the air–water interface. Ladderane PC monolayers collapse at surface pressures similar to liquid-phase monolayers of POPC (Fig. 5*A*), yet their compressibilities, *C*, are similar to those of solid-phase monolayers of DAPC (Fig. 5*C*). In addition, monolayers of ladderane phospholipids have mean molecular areas (MMAs) smaller than fluid straight-chain PCs (Fig. 5*C*). These data suggest that at room temperature the ladderane PC monolayers exist in a phase that is fluid but more tightly packed than straight-chain PCs. Pressure-area isotherms for **[5][3]PC** and **[3][3]PC** are qualitatively similar to the previously published isotherm for a ladderane PC extract (12).

Fluorescence Recovery After Photobleaching. To quantitate fluidity in ladderane PC bilayers, we performed fluorescence recovery after photobleaching (FRAP) experiments on glass-supported lipid bilayers (SLBs) using Oregon Green-DHPE (OG-DHPE) as a fluorescent probe (Fig. 5*B*). As expected for lipids in a gel phase at room temperature, SLBs of **[5][5]PC** showed no lateral diffusion (Fig. 5*B*). SLBs of **[5][3]PC** and **[3][3]PC** exhibited lateral diffusion coefficients, *D*, at least one order of magnitude lower than SLBs of straight-chain PCs (0.24–0.29 $\mu m^2/s$ vs. 2.73–3.93 $\mu m^2/s$) (Fig. 5 *B* and *C*). Straight-chain PCs show a linear correlation between *D* and T_m while ladderane PCs deviate from this trend (Fig. 5*D*).

Discussion and Conclusions

The facile preparation of vesicles, monolayers, and supported bilayers of **[3][3]PC** and **[5][3]PC** was not anticipated, as their

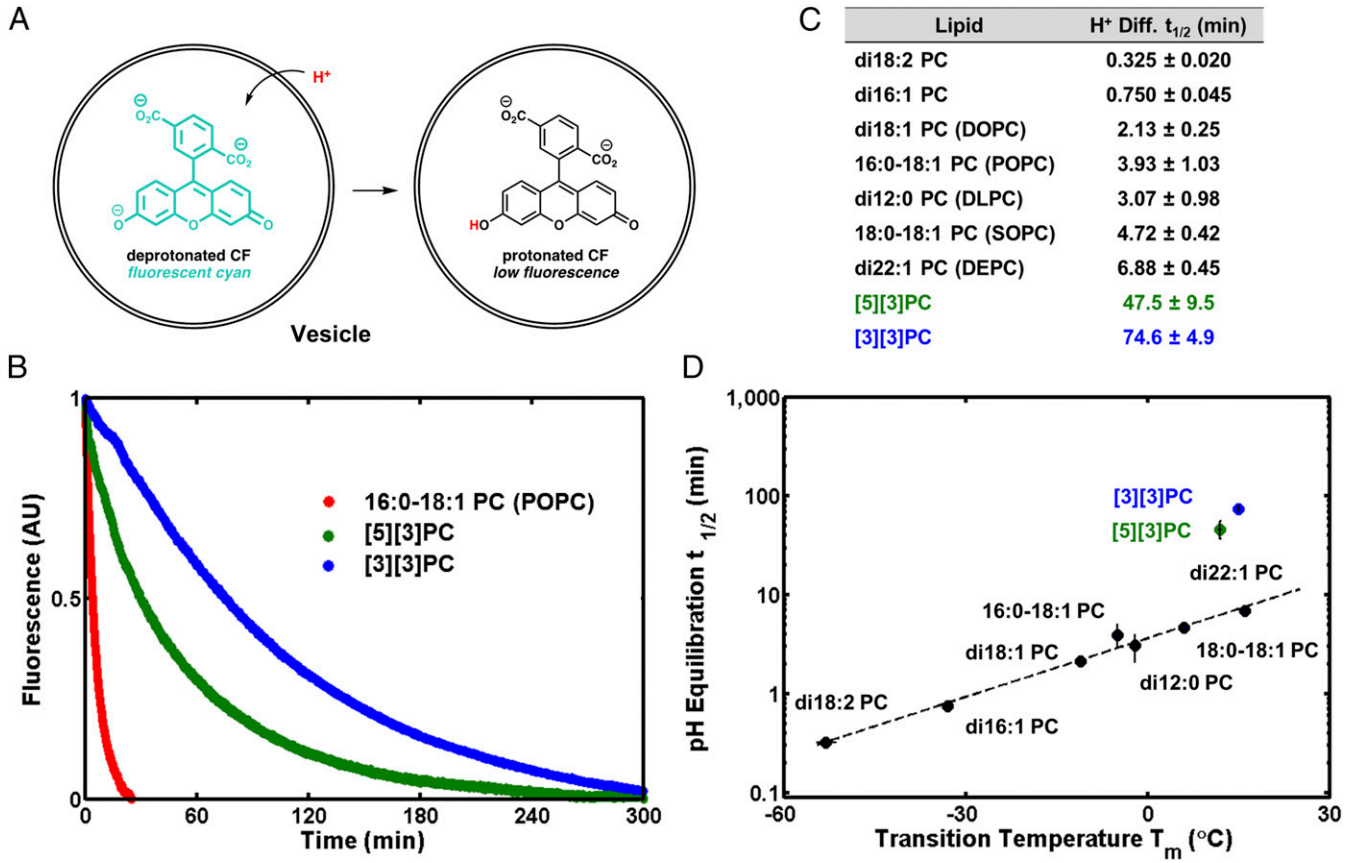

Lipid	H^+ Diff. $t_{1/2}$ (min)
di18:2 PC	0.325 ± 0.020
di16:1 PC	0.750 ± 0.045
di18:1 PC (DOPC)	2.13 ± 0.25
16:0-18:1 PC (POPC)	3.93 ± 1.03
di12:0 PC (DLPC)	3.07 ± 0.98
18:0-18:1 PC (SOPC)	4.72 ± 0.42
di22:1 PC (DEPC)	6.88 ± 0.45
[5][3]PC	47.5 ± 9.5
[3][3]PC	74.6 ± 4.9

Fig. 4. pH equilibration assay. (*A*) Illustration of assay: influx of protons into (or efflux of hydroxide from) vesicles results in the protonation of CF and a decrease in fluorescence intensity. (*B*) Kinetic curves show that equilibration of pH across ladderane PC bilayers is much slower than across straight-chain PC bilayers, as illustrated by the case of POPC. (*C*) Table of pH equilibration half-lives $t_{1/2}$. (*D*) The logarithm of pH equilibration $t_{1/2}$ and straight-chain PC T_m are correlated, while ladderane PCs deviate from this trend.

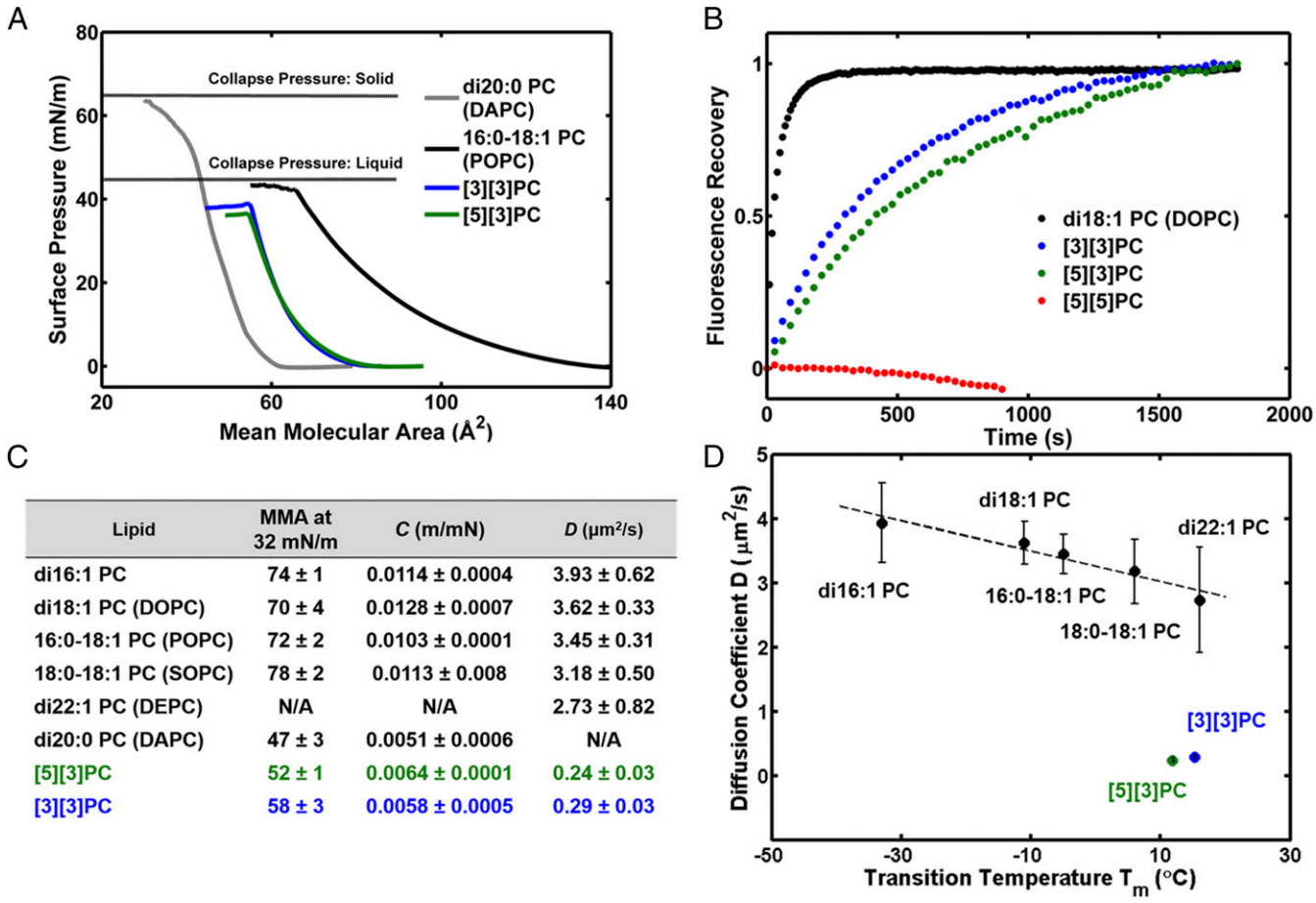

C

Lipid	MMA at 32 mN/m	*C* (m/mN)	*D* (μm²/s)
di16:1 PC	74 ± 1	0.0114 ± 0.0004	3.93 ± 0.62
di18:1 PC (DOPC)	70 ± 4	0.0128 ± 0.0007	3.62 ± 0.33
16:0-18:1 PC (POPC)	72 ± 2	0.0103 ± 0.0001	3.45 ± 0.31
18:0-18:1 PC (SOPC)	78 ± 2	0.0113 ± 0.008	3.18 ± 0.50
di22:1 PC (DEPC)	N/A	N/A	2.73 ± 0.82
di20:0 PC (DAPC)	47 ± 3	0.0051 ± 0.0006	N/A
[5][3]PC	52 ± 1	0.0064 ± 0.0001	0.24 ± 0.03
[3][3]PC	58 ± 3	0.0058 ± 0.0005	0.29 ± 0.03

Fig. 5. Biophysical studies on PC monolayers and bilayers. (*A*) Pressure-area isotherms of Langmuir monolayers composed of di20:0 PC (DAPC, T_m = 68 °C), 16:0–18:1 PC (POPC, T_m = −4.8 °C), and ladderane PCs (T_m = 12–15 °C). (*B*) FRAP curves of ladderane PCs and a representative straight-chain PC, di18:1 PC (DOPC). (*C*) Physical parameters extracted from isotherms and FRAP curves. MMA is given in square angstroms. N/A, not assessed. (*D*) *D* correlates linearly with T_m for straight-chain PCs, but ladderane PCs deviate from this trend.

unique structural elements might be expected to alter their molecular spontaneous curvature and favor nonbilayer structures. However, self-assembly is consistent with the observation that ladderanes are the primary lipid components of the membranes in anammox bacteria, suggesting a major structural role for ladderane phospholipids. Anammox bacteria rely on a pH gradient to drive ATP synthesis (19, 20). Loss of this pH gradient during the slow anammox metabolism would make this process unviable as a source of energy for the cell. Our data support the hypothesis that ladderanes evolved at least in part to impede the loss of this vital pH gradient. Our biophysical results are qualitatively similar to results from complex mixtures of ladderanes, but we are able to observe functional distinctions between individual molecules that are lost in mixtures (for a discussion see *SI Appendix*, section 16) (12, 13). We note that this study was enabled by the success of a scalable natural product total synthesis (14).

Although much work has been done to understand the permeability of membranes to easily detectable drugs and organic dyes, methods of quantifying transmembrane diffusion of small hydrophilic molecules such as hydrazine in real time are limited, often to indirect assays (34–36). The lack of correlation between the rates of pH equilibration and hydrazine transmembrane diffusion provides experimental evidence that these processes occur by different mechanisms. Evidence from the literature supports a model in which proton/hydroxide diffusion occurs via water molecules in the bilayer that act as proton wires or water clusters that carry protons (30, 37–40). Transmembrane diffusion of other ions (e.g., K^+) and small neutral molecules (e.g., H_2O, O_2, and CO_2), the rates of which are directly dependent on bilayer thickness, is thought to occur via direct partitioning into the bilayer and diffusion through the hydrophobic region of the bilayer (21, 41). Our data are consistent with the idea that this is the case for hydrazine. Our data do not support the hypothesis that ladderane PCs alone offer any advantage with respect to hydrazine permeability. Ladderane PC bilayers and straight-chain PC bilayers have similar rates of hydrazine transmembrane diffusion. Notably, the relative hydrazine permeability of ladderane bilayers compared with conventional PC bilayers was correctly predicted by molecular dynamics simulations (42). Hydrazine containment by other means, such as rapid conversion within the hydrazine synthase complex or retention within encapsulin nanocompartments, remains a possibility (17, 43).

In contrast, equilibration of pH across the **[3][3]PC** bilayer was at least 10 times slower than across bilayers composed of any straight-chain PC. To the best of our knowledge this is the slowest known pH equilibration to be measured across a homogeneous PC bilayer; interestingly, very slow pH equilibration across archaea-inspired tetraether lipid monolayers is also known (33). Rates of pH equilibration for straight-chain PC bilayers correlate with their T_ms, which reflect the strength of intermolecular interactions and lipid packing. Our data are consistent with a model in which water must disrupt lipid–lipid interactions to form a proton-conductive wire or cluster in the hydrophobic region of the bilayer. For straight-chain PCs these interactions are accurately reflected in the T_ms, but this

correlation breaks down with **[3][3]PC** and **[5][3]PC**. Monolayers of **[3][3]PC** and **[5][3]PC** at room temperature have smaller MMAs and lower compressibilities than fluid straight-chain PC monolayers, suggesting tighter packing and a higher level of molecular order in the fluid bilayer that is somehow not reflected in the T_m. However, these stronger intermolecular interactions are reflected in the slower lateral diffusion rates in SLBs. Finally, it is interesting to note that **[3][3]PC** and **[5][3]PC**, which both have 20-carbon ladderane tails, form bilayers of similar thickness to di20:1 PC, indicating that the conformational rigidity of the polycyclobutane ladderane motifs counterbalances their shortened structure for a null net effect on bilayer thickness.

Strong London dispersion interactions between ladderane hydrocarbons have been predicted computationally (44). The strong ladderane–ladderane interactions might resist the formation of a proton-conductive water cluster/wire, which would disrupt these interactions (35, 39, 41, 42). This is consistent with the very low D of ladderane bilayers, as this same disruption of packing is necessary for the OG-DHPE to diffuse laterally. D correlates well with pH equilibration $t_{1/2}$ for all PCs assessed, including ladderanes, indicating that D reports on the strength of the physical interactions relevant to proton/hydroxide permeability (*SI Appendix*, Fig. S22). Hydrazine, which is much smaller than a water cluster, may be able to diffuse through small, transient spaces without wholly disrupting ladderane–ladderane packing (12, 45). More generally, we have demonstrated that lipid packing in the hydrophobic region of the lipid bilayer can strongly affect the permeability of the bilayer to small ions. Cells may utilize this mechanism to control the permeabilities of their membranes.

ACKNOWLEDGMENTS. We thank Dr. Stephen R. Lynch for assistance with NMR spectroscopy and Katherine N. Liu for assistance in the development of the hydrazine transmembrane diffusion assay. This work was supported by Stanford University, the Terman Foundation, National Institutes of Health Grants GM069630 and GM118044 (to S.G.B.), the NSF Biophysics Program (S.G.B.), the National Science Foundation (graduate fellowships to J.A.M.M., C.M.C., and S.R.S.), and the Center for Molecular Analysis and Design (graduate fellowship to F.R.M.). Use of the Stanford Synchrotron Radiation Lightsource (SSRL), SLAC National Accelerator Laboratory, is supported by the US Department of Energy (DOE), Office of Science, Office of Basic Energy Sciences under Contract DE-AC02-76SF00515. The SSRL Structural Molecular Biology Program is supported by the DOE Office of Biological and Environmental Research and by the National Institutes of Health, National Institute of General Medical Sciences (NIGMS) (including P41GM103393). The contents of this publication are solely the responsibility of the authors and do not necessarily represent the official views of NIGMS or NIH. Part of this work was performed at the Stanford Nano Shared Facilities, supported by the NSF under Award ECCS-1542152.

1. van Meer G, Voelker DR, Feigenson GW (2008) Membrane lipids: Where they are and how they behave. *Nat Rev Mol Cell Biol* 9:112–124.
2. Alberts B, et al. (2008) Membrane structure. *Molecular Biology of the Cell* (Garland, New York), pp 617–650.
3. Simons K, Vaz WLC (2004) Model systems, lipid rafts, and cell membranes. *Annu Rev Biophys Biomol Struct* 33:269–295.
4. Sinninghe Damsté JS, et al. (2002) Linearly concatenated cyclobutane lipids form a dense bacterial membrane. *Nature* 419:708–712.
5. Nouri DH, Tantillo DJ (2006) They came from the deep: Syntheses, applications, and biology of ladderanes. *Curr Org Chem* 10:2055–2075.
6. Sinninghe Damsté JS, Rijpstra WIC, Geenevasen JAJ, Strous M, Jetten MSM (2005) Structural identification of ladderane and other membrane lipids of planctomycetes capable of anaerobic ammonium oxidation (anammox). *FEBS J* 272:4270–4283.
7. Boumann HA, et al. (2006) Ladderane phospholipids in anammox bacteria comprise phosphocholine and phosphoethanolamine headgroups. *FEMS Microbiol Lett* 258:297–304.
8. Rattray JE, et al. (2008) Ladderane lipid distribution in four genera of anammox bacteria. *Arch Microbiol* 190:51–66.
9. Sinninghe Damsté JS, et al. (2004) A mixed ladderane/*n*-alkyl glycerol diether membrane lipid in an anaerobic ammonium-oxidizing bacterium. *Chem Commun (Camb)*, 2590–2591.
10. Strous M, Heijnen JJ, Kuenen JG, Jetten MSM (1998) The sequencing batch reactor as a powerful tool for the study of slowly growing anaerobic ammonium-oxidizing microorganisms. *Appl Microbiol Biotechnol* 50:589–596.
11. van der Star WRL, et al. (2008) The membrane bioreactor: A novel tool to grow anammox bacteria as free cells. *Biotechnol Bioeng* 101:286–294.
12. Boumann HA, et al. (2009) Biophysical properties of membrane lipids of anammox bacteria: I. Ladderane phospholipids form highly organized fluid membranes. *Biochim Biophys Acta* 1788:1444–1451.
13. Boumann HA, et al. (2009) Biophysical properties of membrane lipids of anammox bacteria: II. Impact of temperature and bacteriohopanoids. *Biochim Biophys Acta* 1788:1452–1457.
14. Mercer JAM, et al. (2016) Chemical synthesis and self-assembly of a ladderane phospholipid. *J Am Chem Soc* 138:15845–15848.
15. Kuenen JG (2008) Anammox bacteria: From discovery to application. *Nat Rev Microbiol* 6:320–326.
16. Kartal B, et al. (2011) Molecular mechanism of anaerobic ammonium oxidation. *Nature* 479:127–130.
17. Dietl A, et al. (2015) The inner workings of the hydrazine synthase multiprotein complex. *Nature* 527:394–397.
18. van der Star WRL, et al. (2010) An intracellular pH gradient in the anammox bacterium *Kuenenia stuttgartiensis* as evaluated by 31P NMR. *Appl Microbiol Biotechnol* 86:311–317.
19. van Niftrik LA, et al. (2004) The anammoxosome: An intracytoplasmic compartment in anammox bacteria. *FEMS Microbiol Lett* 233:7–13.
20. Kartal B, et al. (2013) How to make a living from anaerobic ammonium oxidation. *FEMS Microbiol Rev* 37:428–461.
21. Jetten MSM, et al. (2009) Biochemistry and molecular biology of anammox bacteria. *Crit Rev Biochem Mol Biol* 44:65–84.
22. Nouri DH, Tantillo DJ (2012) Attack of radicals and protons on ladderane lipids: Quantum chemical calculations and biological implications. *Org Biomol Chem* 10: 5514–5517.
23. Reeves JP, Dowben RM (1969) Formation and properties of thin-walled phospholipid vesicles. *J Cell Physiol* 73:49–60.
24. Walde P, Cosentino K, Engel H, Stano P (2010) Giant vesicles: Preparations and applications. *ChemBioChem* 11:848–865.
25. Akashi K, Miyata H, Itoh H, Kinosita K, Jr (1996) Preparation of giant liposomes in physiological conditions and their characterization under an optical microscope. *Biophys J* 71:3242–3250.
26. Veatch SL, Keller SL (2003) Separation of liquid phases in giant vesicles of ternary mixtures of phospholipids and cholesterol. *Biophys J* 85:3074–3083.
27. Sun M, Guo J, Yang Q, Xiao N, Li Y (2014) A new fluorescent and colorimetric sensor for hydrazine and its application in biological systems. *J Mater Chem B* 2:1846–1851.
28. Hughes LD, Rawle RJ, Boxer SG (2014) Choose your label wisely: Water-soluble fluorophores often interact with lipid bilayers. *PLoS One* 9:e87649.
29. Walter A, Gutknecht J (1986) Permeability of small nonelectrolytes through lipid bilayer membranes. *J Membr Biol* 90:207–217.
30. Lorent JH, Levental I (2015) Structural determinants of protein partitioning into ordered membrane domains and lipid rafts. *Chem Phys Lipids* 192:23–32.
31. Pignataro MF, et al. (2015) Modulation of plasma membrane Ca^{2+}-ATPase by neutral phospholipids: Effect of the micelle-vesicle transition and the bilayer thickness. *J Biol Chem* 290:6179–6190.
32. Koyanagi T, et al. (2016) Cyclohexane rings reduce membrane permeability to small ions in archaea-inspired tetraether lipids. *Angew Chem Int Ed Engl* 55:1890–1893.
33. Hervé M, Cybulska B, Gary-Bobo CM (1985) Cation permeability induced by valinomycin, gramicidin D and amphotericin B in large lipidic unilamellar vesicles studied by ^{31}P-NMR. *Eur Biophys J* 12:121–128.
34. Liu H, et al. (2003) *In vitro* permeability of poorly aqueous soluble compounds using different solubilizers in the PAMPA assay with liquid chromatography/mass spectrometry detection. *Pharm Res* 20:1820–1826.
35. Bangham AD, Standish MM, Watkins JC (1965) Diffusion of univalent ions across the lamellae of swollen phospholipids. *J Mol Biol* 13:238–252.
36. Mathai JC, Sprott GD, Zeidel ML (2001) Molecular mechanisms of water and solute transport across archaebacterial lipid membranes. *J Biol Chem* 276:27266–27271.
37. Paula S, Deamer DW (1999) Membrane permeability barriers to ionic and polar solutes. *Curr Top Membr* 48:77–95.
38. Deamer DW, Nichols JW (1989) Proton flux mechanisms in model and biological membranes. *J Membr Biol* 107:91–103.
39. Marrink SJ, Jähnig F, Berendsen HJC (1996) Proton transport across transient single-file water pores in a lipid membrane studied by molecular dynamics simulations. *Biophys J* 71:632–647.
40. Tepper HL, Voth GA (2005) Protons may leak through pure lipid bilayers via a concerted mechanism. *Biophys J* 88:3095–3108.
41. Mathai JC, Tristram-Nagle S, Nagle JF, Zeidel ML (2008) Structural determinants of water permeability through the lipid membrane. *J Gen Physiol* 131:69–76.
42. Chaban VV, Nielsen MB, Kopec W, Khandelia H (2014) Insights into the role of cyclic ladderane lipids in bacteria from computer simulations. *Chem Phys Lipids* 181:76–82.
43. Giessen TW, Silver PA (2017) Widespread distribution of encapsulin nanocompartments reveals functional diversity. *Nat Microbiol* 2:17029.
44. Wagner JP, Schreiner PR (2014) Nature utilizes unusual high London dispersion interactions for compact membranes composed of molecular ladders. *J Chem Theory Comput* 10:1353–1358.
45. Paula S, Volkov AG, Van Hoek AN, Haines TH, Deamer DW (1996) Permeation of protons, potassium ions, and small polar molecules through phospholipid bilayers as a function of membrane thickness. *Biophys J* 70:339–348.

Supporting Information

Ladderane phospholipids form a densely packed membrane with normal hydrazine and anomalously low proton/hydroxide permeability

Frank R. Moss III[a,1], Steven R. Shuken[a,1], Jaron A. M. Mercer[a], Carolyn M. Cohen[a], Thomas M. Weiss[b], Steven G. Boxer[a,2], and Noah Z. Burns[a,2]

[a]Department of Chemistry, Stanford University, Stanford, CA 94305; and [b]Stanford Synchrotron Radiation Laboratory, Stanford Linear Accelerator Center, Stanford University, Menlo Park, CA 94025
[1]F.R.M. and S.R.S. contributed equally to this work.
[2]To whom correspondence may be addressed. Email: sboxer@stanford.edu or nburns@ stanford.edu

Table of Contents

www.pnas.org/cgi/doi/10.1073/pnas.1810706115

1. Diverse Lipid Structures

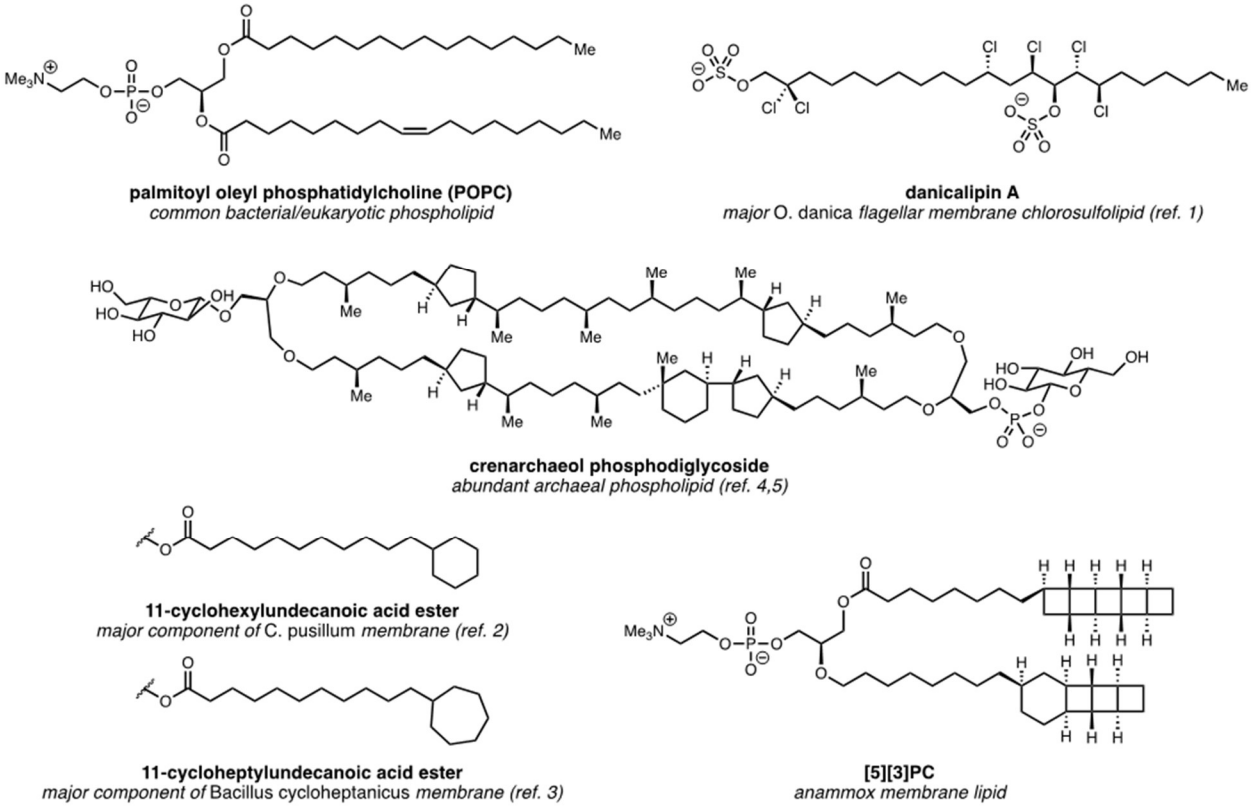

Supplementary Figure S1. Examples of conventional and non-conventional membrane lipids from the literature.[1,2,3,4,5]

2. Chemical Synthesis General Information

All reactions were conducted in oven- or flame-dried glassware under an atmosphere of nitrogen or argon unless otherwise noted. Commercial reagents and solvents were used as received unless otherwise noted with the exception of the following: hexanes (ACS grade, 4.2% various methylpentanes), toluene, tetrahydrofuran, acetonitrile, methanol, benzene, and dichloromethane were dried by passing through a bed of activated alumina in a JC Meyer Solvent System. Flash column chromatography was performed using F60 silica gel (40-63 μm, 230-400 mesh, 60Å) purchased from Silicycle. Analytical thin-layer chromatography (TLC) was carried out on 250 μm 60-F254 silica gel plates purchased from EMD Millipore, and visualization was affected by observation of fluorescence-quenching with ultraviolet light and staining with either p-anisaldehyde, potassium permanganate, or phosphomolybdic acid and cerium sulfate (Seebach's stain) as a developing agent. Proton nuclear magnetic resonance (^{1}H NMR), carbon nuclear magnetic resonance (^{13}C NMR), and 2-dimensional nuclear magnetic resonance (2D NMR) spectra were recorded on Varian Inova 600, Varian Inova 500, Varian Mercury 400, or Varian Inova 300 spectrometers operating respectively at 600, 500, 400, and 300 MHz for ^{1}H and at 150, 125, 100, and 75 MHz for ^{13}C. Chemical shifts are reported in parts per million (ppm) with respect to residual protonated solvent for ^{1}H ($CHCl_3$ = δ 7.26, CH_3OH = δ 3.31) and with respect to carbon resonances of the solvent for ^{13}C ($CDCl_3$ = δ 77.0 CD_3OD = δ 49.86). Peak multiplicities are annotated as follows: app = apparent, br = broad, s = singlet, d = doublet, t = triplet, q = quartet, p = quintet, m = multiplet. Infrared (IR) spectra were recorded on a Nicolet 6700 FT-IR spectrometer. LC-MS (ESI) data were collected on a Waters Micromass ZQ or a Waters Micromass LCT Premier mass spectrometer. GC-MS (CI) data were collected on a Waters Micromass GCT Premier or a VG Micromass 7070 mass spectrometer. Isotopic abundance patterns observed alongside each major ion reported matched calculated ratios. Optical rotations were measured using a JASCO P-2000 polarimeter. Reverse-phase semi-preparative high-performance liquid chromatography was performed on an Agilent Technologies 1260 Infinity machine equipped with a Kromasil 300-5C4 250x10mm column from Peeke Scientific (Redwood City, CA). Uncorrected melting point data were collected using a Thomas Hoover Uni-Melt apparatus.

3. Chemical Synthesis Schemes

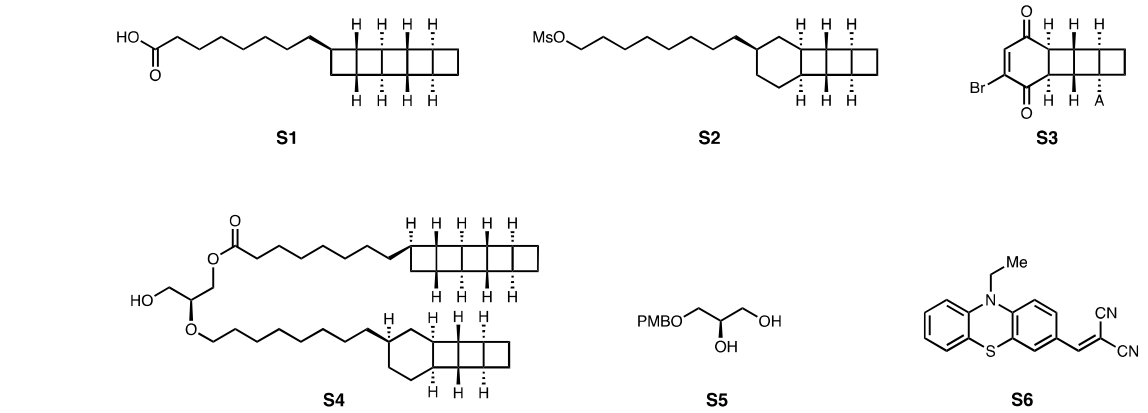

Supplementary Figure S2. Previously reported intermediates.

[5]-Ladderanoic acid **S1** was prepared in either 80% ee or 90% ee as previously reported.[6] [3]-Ladderane mesylate **S2** was prepared in >96% ee by recrystallizing intermediate **S3** along the previously reported route. [5][3] glycerol alcohol **S4** was prepared from **S1** (90% ee) and **S2** (96% ee) as previously reported. Glycerol diol **S5** was prepared according to a literature procedure.[7] Hydrazine sensor **S6** was prepared according to a literature procedure and the structure was reassigned on the basis of 2D NMR studies (see below).[8]

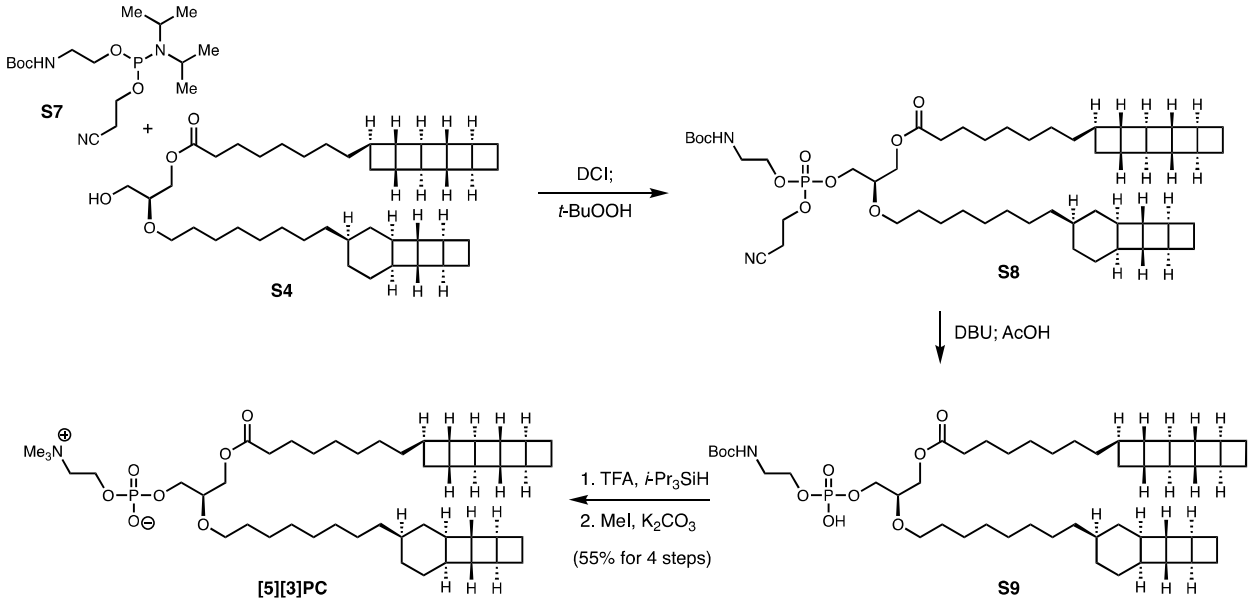

Supplementary Scheme S1. Preparation of **[5][3]PC**.

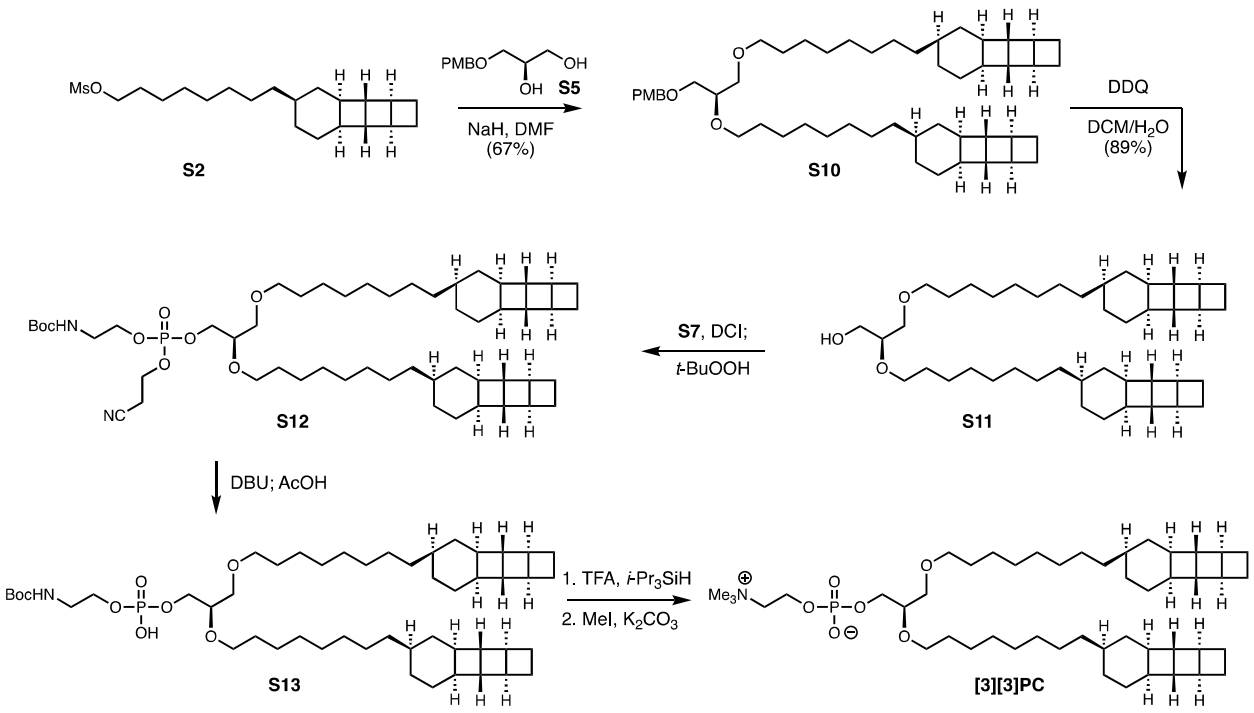

Supplementary Scheme S2. Preparation of **[3][3]PC**.

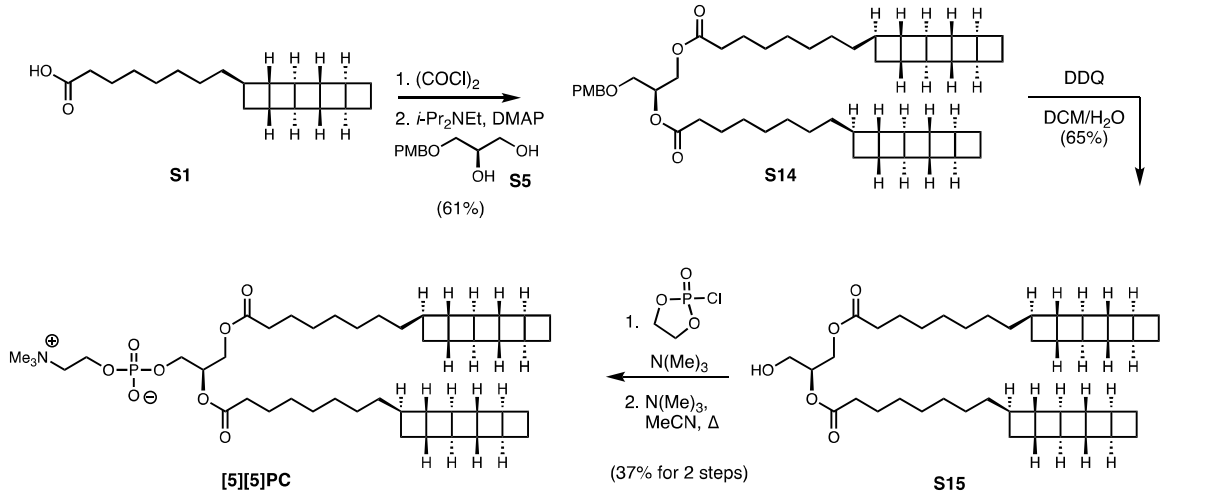

Supplementary Scheme S3. Preparation of **[5][5]PC**.

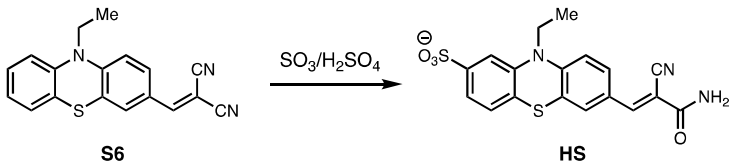

Supplementary Scheme S4. Preparation of **HS**.

4. Chemical Synthesis Experimental Procedures

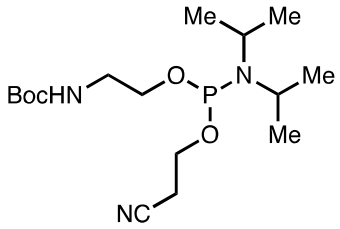

Phosphoramidite S7:

To a solution of *N*-Boc-ethanolamine (80.6 mg, 0.5 mmol, 1.0 equiv.) and *N,N*-diisopropylethylamine (218 µL, 1.25 mmol, 2.5 equiv.) in 1,2-dichloroethane (2.5 mL, 0.2 M) was added 2-cyanoethyl *N,N*-diisopropylchlorophosphoramidite (139 µL, 0.625 mmol, 1.25 equiv.) dropwise by syringe. The reaction mixture was allowed to stir at room temperature for 1.5 hours, then quenched by the addition of sat. aq. $NaHCO_3$ (3 mL). The resulting mixture was partitioned between dichloromethane (10 mL) and water (10 mL). The layers were separated, and the aqueous layer was extracted with dichloromethane (2 x 10 mL). The combined organic extracts were washed with sat. aq. sodium chloride (20 mL), dried over sodium sulfate, filtered, and concentrated *in vacuo*. The crude residue was purified by flash column chromatography on silica gel (30% EtOAc/hexanes), providing **S7** (76 mg, 42%) as a colorless oil.

Physical properties: colorless oil;
R_f = 0.21 (silica gel, 65:15:2 DCM:MeOH:H_2O, visualized with Seebach's stain);
IR (film) ν_{max} = 3372, 2967, 2932, 2873, 2253, 1705, 1510, 1460, 1393, 1364, 1251, 1174, 1027, 977, 877, 707, 641, 521 cm^{-1};
^{1}H NMR (400 MHz, $CDCl_3$): δ 4.95 (br s, 1H), 3.92 – 3.83 (m, 1H), 3.83 – 3.75 (m, 1H), 3.75 – 3.63 (m, 2H), 3.63 – 3.53 (m, 2H), 3.32 (q, *J* = 5.6 Hz, 2H), 2.64 (t, *J* = 5.9 Hz, 2H), 1.42 (s, 9H), 1.16 (dd, *J* = 6.6, 4.5 Hz, 12H);
^{13}C NMR (126 MHz, $CDCl_3$) δ 155.78, 117.54, 79.14, 77.26, 77.20, 77.00, 76.75, 62.95, 62.82, 58.35, 58.19, 43.01, 42.91, 41.60, 41.55, 28.31, 28.18, 24.59, 24.52, 24.46, 20.30, 20.25;
^{31}P NMR (162 MHz, $CDCl_3$) δ 148.47.

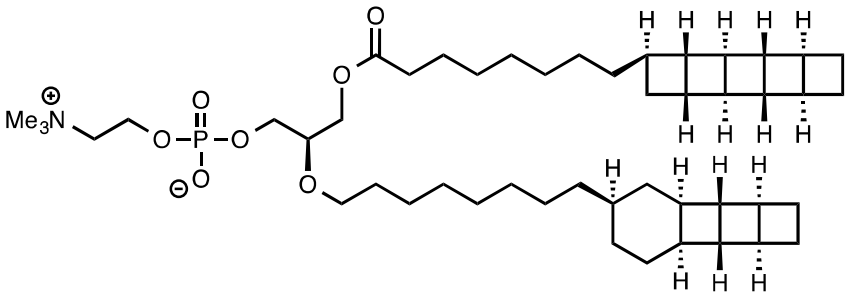

[5][3PC:

The following sequence was adapted from literature procedures.[9,10] [5][3] glycerol alcohol **S4** (14.7 mg, 22.6 µmol, 1.0 equiv.) and phosphoramidite **S7** (20.4 mg, 56.5 µmol, 2.5 equiv.) were concentrated from toluene (ca. 1 mL) in a 5-mL screw-cap vial. The vial was equipped with a magnetic stir bar, capped with a rubber septum, and flushed with nitrogen. The residue was taken up in anhydrous dichloromethane (226 µL, 0.1M). To the resulting solution was added a 0.5 M solution of 4,5-dicyanoimidazole in anhydrous acetonitrile (226 µL, 113 µmol, 5.0 equiv.) by syringe. After four hours, the reaction mixture was cooled to –40 ºC in a dry ice-acetonitrile bath and 70% *tert*-butylhydroperoxide (15.6 µL, 113 µmol, 5.0 equiv.) was added dropwise by syringe. The cooling bath was removed, and the reaction mixture was allowed to warm to 23 ºC. After one hour, remaining oxidant was quenched by the addition of sat. aq. sodium thiosulfate (1 mL). The resulting mixture was partitioned between chloroform (5 mL) and water (5 mL). The layers were separated, and the aqueous layer was extracted twice more with chloroform (2 x 5 mL). The combined organics were dried with sodium sulfate, filtered, and concentrated *in vacuo* to provide crude **S8**.

A 5-mL screw-cap vial was charged with crude **S8** (22.6 µmol, 1.0 equiv.), equipped with a magnetic stir bar, capped with a rubber septum, and flushed with nitrogen. The residue was taken up in anhydrous dichloromethane (1 mL). The resulting solution was cooled to 0 ºC in an ice-water bath, and 1,8-diazabicyclo(4.5.0)undec-7-ene (35 µL, 226 µmol, 10 equiv.) was added dropwise by syringe. The cooling bath was removed, and the reaction mixture was allowed to stir at 23 ºC for an hour. After this time, acetic acid (5 drops) and toluene (1 mL) were added by pipet. The solution was concentrated *in vacuo*. Remaining acetic acid was removed by repeated concentration from toluene (2 x 1 mL). The resulting residue was purified by flash column chromatography on silica gel (2 to 5 to 10 to 20% MeOH/DCM) to provide **S9**.

A 10-mL round bottom flask was charged with **S9** (22.6 µmol, 1.0 equiv.), and equipped with a magnetic stir bar. The residue was taken up in anhydrous dichloromethane (1.13 mL, 0.02 M), and the resulting solution was cooled to 0 ºC in an ice-water bath. Triisopropylsilane (27.8 µL, 135.6 µmol, 6 equiv.) and trifluoroacetic acid (138 µL, 1.81 mmol, 80 equiv.) were added sequentially by syringe. The cooling bath was removed, and the resulting mixture was allowed to stir at 23 ºC for one hour. After this time, toluene (1 mL) was added by pipet and the reaction mixture was concentrated *in vacuo*. Remaining trifluoroacetic acid was removed by repeated concentration from toluene (2 x 1 mL).

The crude residue was concentrated from toluene in 5-mL screw-cap vial. The vial was equipped with a stir bar, capped with a rubber septum, and flushed with nitrogen. The residue was taken up in benzene (1 mL). Solid potassium carbonate (15.6 mg, 113 µmol, 5 equiv.) and 18-crown-6 (59.7 mg, 226 µmol, 10 equiv.) were added in single portions. Iodomethane (14.1 µL, 226 µmol, 10 equiv.) was added dropwise by syringe. The rubber septum was exchanged for a

Teflon-lined screw cap, and the reaction vial was placed in a 40 ºC oil bath for 24 hours. After this time, the reaction mixture was partitioned between half sat. aq. sodium chloride (5 mL) and 10% isopropanol/chloroform (5 mL). The layers were separated, and the aqueous layer was extracted with additional 10% isopropanol/chloroform (4 x 5 mL). The combined organics were dried with sodium sulfate, filtered, and concentrated *in vacuo*. The resulting residue was purified first by flash column chromatography on silica gel (65:15:2 DCM:MeOH:H_2O) and then by reverse-phase semi-preparative high-performance liquid chromatography (Kromasil 300-5C4 250x10mm, operating at a 3 mL/min flow rate eluting first with 5% MeOH/95% 50 mM aq. NH_4OAc for 10 minutes, then 95% MeOH/5% 50 mM aq. NH_4OAc for 20 min, then 100% MeOH for 20 minutes) to provide **[5][3]PC** (10.2 mg, 55% for four steps) as a colorless wax.

Physical properties: colorless wax;
R_f = 0.21 (silica gel, 65:15:2 DCM:MeOH:H_2O, visualized with Seebach's stain);
IR (film) ν_{max} = 2918, 2850, 1729, 1467, 1236, 1089, 969 cm^{-1};
^{1}H NMR (600 MHz, $CDCl_3$): δ 4.39 – 4.30 (m, 2H), 4.28 (dd, *J* = 11.7, 3.2 Hz, 1H), 4.08 (dd, *J* = 11.7, 7.1 Hz, 1H), 3.99 – 3.91 (m, 1H), 3.89 – 3.78 (m, 3H), 3.68 – 3.62 (m, 1H), 3.60 – 3.54 (m, 1H), 3.52 – 3.46 (m, 1H), 3.37 (s, 9H), 2.73 (bd, *J* = 6.5 Hz, 3H), 2.65 – 2.60 (m, 4H), 2.60 (br s, 1H), 2.58 – 2.57 (m, 1H), 2.57 – 2.53 (m, 2H), 2.52 – 2.44 (m, 1H), 2.44 – 2.36 (m, 2H), 2.36 – 2.33 (m, 1H), 2.31 – 2.28 (m, 3H), 2.28 – 2.25 (m, 1H), 2.22 – 2.14 (m, 3H), 2.07 – 2.02 (m, 2H), 2.02 – 1.97 (m, 1H), 1.97 – 1.90 (m, 1H), 1.88 – 1.81 (m, 1H), 1.77 – 1.71 (m, 1H), 1.64 – 1.56 (m, 2H), 1.55 – 1.47 (m, 5H), 1.47 – 1.38 (m, 2H), 1.31 – 1.23 (m, 16H), 1.22 – 1.13 (m, 5H), 1.13 – 1.06 (m, 1H), 1.06 – 0.98 (m, 1H);
^{13}C NMR (101 MHz, $CDCl_3$): δ 173.80, 70.50, 66.32, 64.41, 63.90, 59.19, 54.42, 49.40, 49.33, 49.31, 49.15, 48.26, 47.27, 47.23, 42.20, 41.78, 41.48, 39.88, 38.47, 38.19, 37.84, 37.63, 37.37, 34.29, 34.24, 33.26, 32.50, 30.08, 30.03, 29.79, 29.60, 29.40, 29.22, 28.19, 26.96, 26.50, 26.46, 26.16, 26.07, 25.48, 25.46, 24.98;
^{31}P NMR (162 MHz, $CDCl_3$) δ –0.69;
MS (ESI) calcd. for $C_{48}H_{80}NO_7P$ $[M + H]^+$ 814.58, found 814.7;
$[\alpha]_D^{23}$ = +9.1 (c = 1.0, $CHCl_3$).

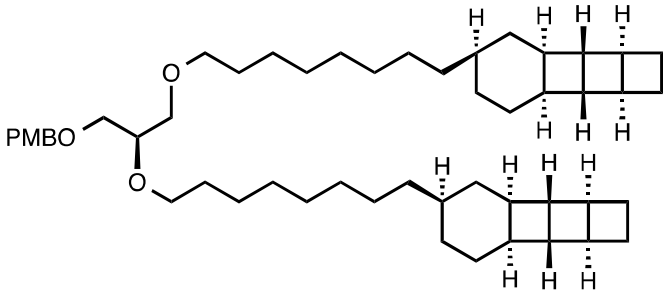

[3][3] Glycerol ether S10:

To a solution of glycerol diol **S5** (26.7 mg, 0.126 mmol, 1.0 equiv.) in anhydrous DMF (316 μL) at 23 °C was added a 2M solution of sodium hydride in DMF (316 μL, 0.632 mmol, 5.0 equiv.) dropwise by syringe. After 15 minutes, a solution of 96% ee [3]-ladderanol mesylate **S2** (93.2 mg, 0.25 mmol, 2.0 equiv.) in DMF (630 μL) was added dropwise via syringe. The reaction mixture was heated to 70 °C for 2.5 hours, then cooled to 0 °C and quenched by the dropwise addition of sat. aq. NH_4Cl (1 mL). The resulting mixture was partitioned between sat. aq. NaCl (1 mL) and Et_2O (3 mL), and the layers were separated. The aqueous layer was extracted with Et_2O (2 x 3 mL). The combined organic extracts were dried with sodium sulfate, filtered, and concentrated *in vacuo*. The crude residue was purified by flash column chromatography on silica gel (2 to 5% EtOAc/hexanes), providing **S10** (63.5 mg, 67%) as a colorless oil.

Physical properties: colorless oil;
R_f = 0.51 (silica gel, 10% EtOAc/hexanes, visualized with anisaldehyde stain);
IR (film) ν_{max} = 2922, 2852, 1614, 1513, 1465, 1302, 1247, 1112, 1040, 819 cm^{-1};
^{1}H NMR (600 MHz, $CDCl_3$): δ 7.27 – 7.24 (m, 2H), 6.89 – 6.85 (m, 2H), 4.48 (s, 2H), 3.80 (s, 3H), 3.62 – 3.45 (m, 7H), 3.42 (t, *J* = 6.7 Hz, 2H), 2.73 (br d, *J* = 6.9 Hz, 2H), 2.62 (br t, *J* = 3.8 Hz, 2H), 2.54 – 2.45 (m, 2H), 2.45 – 2.37 (m, 4H), 2.29 (d, *J* = 3.6 Hz, 2H), 2.29 – 2.25 (m, 2H), 2.23 – 2.17 (m, 2H), 1.98 – 1.91 (m, 2H), 1.88 – 1.82 (m, 2H), 1.78 – 1.72 (m, 2H), 1.60 – 1.52 (m, 6H), 1.52 – 1.47 (m, 4H), 1.38 – 1.22 (m, 20H), 1.22 – 1.15 (m, 6H), 1.14 – 1.06 (m, 2H), 1.06 – 0.98 (m, 2H);
^{13}C NMR 126 MHz, $CDCl_3$): δ 159.06, 130.47, 129.19, 113.65, 77.87, 72.98, 71.62, 70.76, 70.56, 69.89, 55.25, 55.19, 49.35, 47.27, 42.21, 41.49, 38.15, 37.85, 37.64, 34.24, 32.48, 30.08, 29.94, 29.68, 29.51, 28.19, 26.89, 26.16, 26.12, 26.09, 25.49;
MS (ESI) calcd. for $C_{51}H_{80}O_4$ $[M + Na]^+$ 779.60, found 779.7;
$[\alpha]_D^{24}$ = +13.9 (c = 0.38, $CHCl_3$).

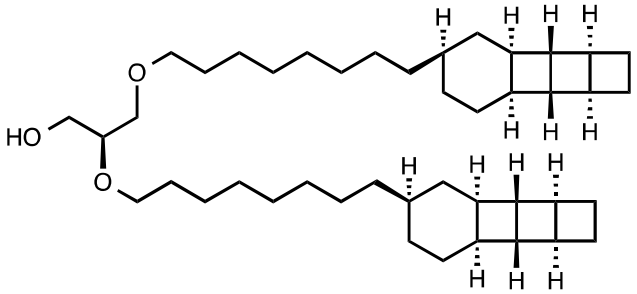

[3][3] Glycerol alcohol S11:

To a solution of **S10** (63.5 mg, 0.084 mmol, 1.0 equiv.) in DCM (1.7 mL, 0.05 M) and water (170 µL, 0.05 M) at 0 ºC was added DDQ (38.1 mg, 0.168 mmol, 2.0 equiv.) in a single portion. The reaction mixture was allowed to stir vigorously at 0 ºC for 3 hours, then filtered through a pad of celite, washing thoroughly with DCM (3 mL). To the filtrate was added sat. aq. $NaHCO_3$ (1 mL). The layers were separated, and the aqueous layer was extracted with DCM (3 x 3 mL). The combined organics were dried with sodium sulfate, filtered, and concentrated *in vacuo*. The crude residue was purified by flash column chromatography on silica gel (0.5 to 2% MeOH/DCM), providing **S11** (30.1 mg, 89%) as a colorless wax.

Physical properties: colorless wax;
R_f = 0.18 (silica gel, 10% EtOAc/hexanes, visualized with anisaldehyde stain);
IR (film) ν_{max} = 3452 (br), 2920, 2852, 1466, 1117 cm^{-1};
^{1}H NMR (600 MHz, $CDCl_3$): δ 3.75 – 3.69 (m, 1H), 3.65 – 3.58 (m, 2H), 3.57 – 3.49 (m, 3H), 3.49 – 3.46 (m, 1H), 3.45 – 3.41 (m, 2H), 2.72 (br d, *J* = 6.8 Hz, 2H), 2.62 (br t, *J* = 3.9 Hz, 2H), 2.53 – 2.45 (m, 2H), 2.45 – 2.34 (m, 4H), 2.29 (d, *J* = 3.7 Hz, 2H), 2.28 – 2.24 (m, 2H), 2.23 – 2.17 (m, 3H), 1.98 – 1.90 (m, 2H), 1.88 – 1.81 (m, 2H), 1.77 – 1.71 (m, 2H), 1.61 – 1.52 (m, 6H), 1.52 – 1.46 (m, 4H), 1.38 – 1.22 (m, 20H), 1.22 – 1.14 (m, 6H), 1.13 – 1.06 (m, 2H), 1.05 – 0.98 (m, 2H);
^{13}C NMR (126 MHz, $CDCl_3$): δ 78.19, 71.83, 70.89, 70.38, 63.09, 49.38, 49.32, 47.27, 42.25, 42.18, 41.54, 41.43, 38.14, 37.88, 37.83, 37.64, 34.26, 34.21, 32.48, 30.05, 29.91, 29.64, 29.46, 28.19, 26.87, 26.21, 26.09, 25.49;
MS (ESI) calcd. for $C_{43}H_{72}O_3$ $[M + Na]^+$ 659.54, found 659.6;
$[\alpha]_D^{24}$ = +6.32 (c = 0.26, $CHCl_3$).

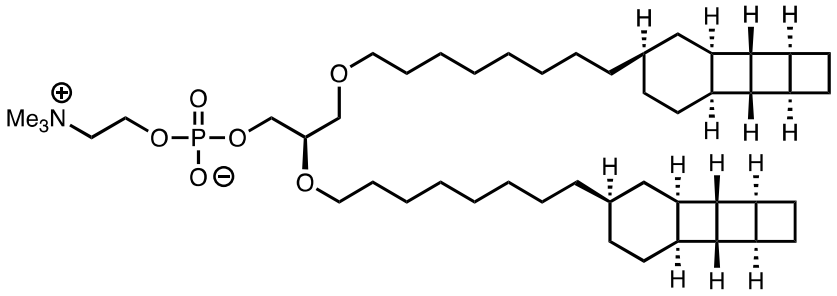

[3][3]PC:

[3][3] glycerol alcohol **S11** (12.5 mg, 19.6 µmol, 1.0 equiv.) and phosphoramidite **S7** (17.7 mg, 49 µmol, 2.5 equiv.) were concentrated from toluene (ca. 1 mL) in a 5-mL screw-cap vial. The vial was equipped with a magnetic stir bar, capped with a rubber septum, and flushed with nitrogen. The residue was taken up in anhydrous dichloromethane (280 µL, 0.07 M). To the resulting solution was added a 0.5 M solution of 4,5-dicyanoimidazole in anhydrous acetonitrile (245 µL, 98 µmol, 5.0 equiv.) by syringe. After four hours, the reaction mixture was cooled to –40 ºC in a dry ice-acetonitrile bath and 70% *tert*-butylhydroperoxide (13.6 µL, 98 µmol, 5.0 equiv.) was added dropwise by syringe. The cooling bath was removed, and the reaction mixture was allowed to warm to 23 ºC. After one hour, remaining oxidant was quenched by the addition of sat. aq. sodium thiosulfate (1 mL). The resulting mixture was partitioned between chloroform (5 mL) and water (5 mL). The layers were separated, and the aqueous layer was extracted twice more with chloroform (2 x 5 mL). The combined organics were dried with sodium sulfate, filtered, and concentrated *in vacuo* to provide crude **S12**.

A 5-mL screw-cap vial was charged with crude **S12** (19.6 µmol, 1.0 equiv.), equipped with a magnetic stir bar, capped with a rubber septum, and flushed with nitrogen. The residue was taken up in anhydrous dichloromethane (1 mL). The resulting solution was cooled to 0 ºC in an ice-water bath, and 1,8-diazabicyclo(4.5.0)undec-7-ene (29 µL, 196 µmol, 10 equiv.) was added dropwise by syringe. The cooling bath was removed, and the reaction mixture was allowed to stir at 23 ºC for an hour. After this time, acetic acid (5 drops) and toluene (1 mL) were added by pipet. The solution was concentrated *in vacuo*. Remaining acetic acid was removed by repeated concentration from toluene (2 x 1 mL). The resulting residue was purified by flash column chromatography on silica gel (2 to 5 to 10 to 20% MeOH/DCM) to provide **S13**.

A 10-mL round bottom flask was charged with **S13** (16.9 µmol, 1.0 equiv.), and equipped with a magnetic stir bar. The residue was taken up in anhydrous dichloromethane (850 µL, 0.02 M), and the resulting solution was cooled to 0 ºC in an ice-water bath. Triisopropylsilane (35 µL, 169 µmol, 10 equiv.) and trifluoroacetic acid (103 µL, 1.35 mmol, 80 equiv.) were added sequentially by syringe. The cooling bath was removed, and the resulting mixture was allowed to stir at 23 ºC for one hour. After this time, toluene (1 mL) was added by pipet and the reaction mixture was concentrated *in vacuo*. Remaining trifluoroacetic acid was removed by repeated concentration from toluene (2 x 1 mL).

The crude residue was concentrated from toluene in 5-mL screw-cap vial. The vial was equipped with a stir bar, capped with a rubber septum, and flushed with nitrogen. The residue was taken up in benzene (560 µL). Solid potassium carbonate (11.7 mg, 85 µmol, 5 equiv.) and 18-crown-6 (45 mg, 169 µmol, 10 equiv.) were added in single portions. Iodomethane (10.5 µL, 169 µmol, 10 equiv.) was added dropwise by syringe. The rubber septum was exchanged for a Teflon-lined screw cap, and the reaction vial was placed in a 40 ºC oil bath for 24 hours. After this time,

the reaction mixture was partitioned between half sat. aq. sodium chloride (5 mL) and 10% isopropanol/chloroform (5 mL). The layers were separated, and the aqueous layer was extracted with additional 10% isopropanol/chloroform (4 x 5 mL). The combined organics were dried with sodium sulfate, filtered, and concentrated *in vacuo*. The resulting residue was purified first by flash column chromatography on silica gel (65:15:2 DCM:MeOH:H_2O) and then by reverse-phase semi-preparative high-performance liquid chromatography (Kromasil 300-5C4 250x10mm, operating at a 3 mL/min flow rate eluting first with 5% MeOH/95% 50 mM aq. N H_4OAc for 10 minutes, then 95% MeOH/5% 50 mM aq. NH_4OAc for 20 min, then 100% MeOH for 20 minutes) to provide **[3][3]PC** (5.2 mg, 33% for four steps) as a colorless wax.

Physical properties: colorless wax;
R_f = 0.22 (silica gel, 65:15:2 DCM:MeOH:H_2O, visualized with Seebach's stain);
IR (film) ν_{max} = 2920, 2851, 1467, 1245, 1089, 1062, 968, 765 cm^{-1};
^{1}H NMR (600 MHz, $CDCl_3$): δ 4.31 (br s, 2H), 3.90 – 3.82 (m, 2H), 3.82 – 3.77 (m, 2H), 3.63 – 3.50 (m, 4H), 3.48 – 3.40 (m, 3H), 3.38 (s, 9H), 2.72 (br d, *J* = 6.7 Hz, 2H), 2.62 (br t, *J* = 3.7 Hz, 2H), 2.53 – 2.45 (m, 2H), 2.45 – 2.36 (m, 4H), 2.29 (d, *J* = 3.7 Hz, 2H), 2.28 – 2.24 (m, 2H), 2.23 – 2.16 (m, 2H), 1.97 – 1.90 (m, 2H), 1.87 – 1.81 (m, 2H), 1.78 – 1.70 (m, 2H), 1.58 – 1.45 (m, 10H), 1.34 – 1.21 (m, 20H), 1.19 (q, *J* = 6.9 Hz, 6H), 1.13 – 1.05 (m, 2H), 1.05 – 0.98 (m, 2H);
^{13}C NMR (126 MHz, $CDCl_3$): δ 78.08, 71.68, 70.86, 70.46, 66.44, 64.84, 59.15, 54.47, 49.34, 47.27, 42.21, 41.48, 38.19, 37.85, 37.64, 34.25, 32.50, 30.21, 30.01, 29.78, 29.75, 29.61, 29.60, 28.20, 26.94, 26.17, 26.11, 25.49, 25.47;
^{31}P NMR (162 MHz, $CDCl_3$) δ –0.54;
MS (ESI) calcd. for $C_{48}H_{84}NO_6P$ $[M + H]^+$ 802.61, found 802.7;
$[\alpha]_D^{24}$ = +17.9 (c = 0.2, $CHCl_3$).

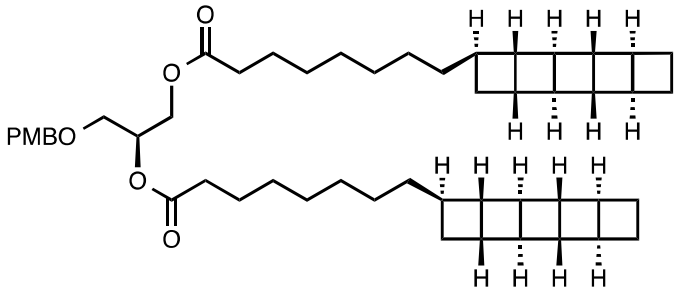

[5][5] glycerol ether S14:

To a slurry of 80% ee [5]-ladderanoic acid **S1** (25.0 mg, 82.7 µmol, 2.0 equiv.) in toluene (827 µL, 0.1 M) at 0 ºC (ice bath) under nitrogen was added oxalyl chloride (14.2 µL, 165 µmol, 2.0 equiv.) dropwise by syringe. A single drop of DMF was added by syringe. The cooling bath was removed, and the mixture was allowed to warm to room temperature. The mixture was allowed to stir for 2 hours, becoming homogeneous as the reaction proceeded. Solvent was removed *in vacuo*, affording a residue which was taken up in toluene (1 mL) and concentrated again. The concentrated residue was taken up in DCM (100 µL), and the resulting solution was cooled to 0 ºC. A solution of diol **S5** (7.46 mg, 35.1 µmol, 0.85 equiv.), *i*-$PrNEt_2$ (17.9 µL, 103 µmol, 2.5 equiv.), and 4-dimethylaminopyridine (0.50 mg, 4.13 µmol, 10 mol%) in DCM (314 µL) was added dropwise by syringe. The resulting mixture was allowed to stir for 36 hours at 23 ºC. The reaction was quenched by the addition of 1 N aq. HCl (2 mL). The resulting biphasic mixture was partitioned between chloroform (8 mL) and water (8 mL). The layers were separated, and the aqueous layer was extracted with chloroform (2 x 8 mL). The combined organics were dried with sodium sulfate, filtered, and concentrated *in vacuo*. The crude residue was purified by flash column chromatography on silica gel (2 to 4 to 6% EtOAc/hexanes) to provide [5][5] PMB ether **S14** (21.0 mg, 65%) as a colorless wax.

Physical properties: colorless wax;
R_f = 0.61 (silica gel, 20% EtOAc/hexanes, visualized with anisaldehyde stain);
IR (film) ν_{max} = 2918, 2851, 1741, 1613, 1514, 1248, 1167, 1104, 820 cm^{-1};
^{1}H NMR (500 MHz, $CDCl_3$): δ 7.23 (d, *J* = 7.8 Hz, 2H), 6.87 (d, *J* = 8.6 Hz, 2H), 5.26 – 5.18 (m, 1H), 4.46 (app. q, *J* = 11.7 Hz, 2H), 4.32 (dd, *J* = 11.8, 3.7 Hz, 1H), 4.17 (dd, *J* = 11.9, 6.5 Hz, 1H), 3.80 (s, 3H), 3.55 (dd, *J* = 5.3, 2.1 Hz, 2H), 2.72 (br d, *J* = 5.5 Hz, 4H), 2.62 (m, 6H), 2.59 (s, 2H), 2.58 – 2.50 (m, 6H), 2.34 (s, 2H), 2.31 (t, *J* = 7.5 Hz, 2H), 2.27 (t, *J* = 7.6 Hz, 2H), 2.23 – 2.09 (m, 4H), 2.09 – 1.95 (m, 6H), 1.65 – 1.54 (m, 4H), 1.52 – 1.36 (m, 4H), 1.33 – 1.23 (m, 12H), 1.23 – 1.15 (m, 4H);
^{13}C NMR (126 MHz, $CDCl_3$): δ 173.42, 173.13, 159.26, 129.70, 129.29, 113.77, 72.93, 69.98, 67.86, 62.68, 55.23, 49.41, 49.36, 49.32, 49.16, 48.28, 47.23, 41.79, 39.87, 38.47, 37.34, 34.32, 34.11, 33.25, 29.51, 29.32, 29.10, 29.07, 26.50, 26.46, 24.95, 24.87;
MS (ESI) calcd. for $C_{51}H_{72}O_6$ $[M + Na]^+$ 803.52, found 803.7;
$[\alpha]_D^{25}$ = –5.2 (c = 0.5, $CHCl_3$).

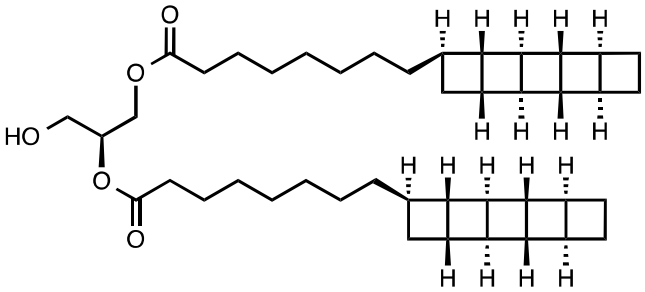

[5][5] Glycerol alcohol S15:

To a solution of **S14** (23.0 mg, 29.4 μmol, 1.0 equiv.) in DCM (589 μL, 0.05M) and water (58.9 μL, 0.5M) at 0 ºC was added DDQ (13.4 mg, 58.9 μmol, 2.0 equiv.) in a single portion. The reaction mixture was allowed to stir vigorously at 0 ºC for 8 hours, then filtered through a pad of celite, washing thoroughly with DCM (10 mL total). To the filtrate was added sat. aq. $NaHCO_3$ (10 mL). The layers were separated, and the aqueous layer was extracted with DCM (2 x 10 mL). The organic layers were combined, dried with sodium sulfate, filtered, and concentrated *in vacuo*. The crude residue was purified by flash column chromatography on silica gel (0.5 to 2% MeOH/DCM), providing **S15** (12.7 mg, 65%) as a colorless wax.

Physical properties: colorless wax;
R_f = 0.42 (silica gel, 20% EtOAc/hexanes, visualized with anisaldehyde stain);
IR (film) ν_{max} = 3345, 2917, 2849, 1739, 1466, 1165, 669 cm^{-1};
^{1}H NMR (500 MHz, $CDCl_3$): δ 5.11 – 5.05 (m, 1H), 4.32 (dd, *J* = 11.9, 4.4 Hz, 1H), 4.23 (dd, *J* = 11.9, 5.7 Hz, 1H), 3.73 (d, *J* = 5.0 Hz, 2H), 2.72 (br d, *J* = 6.3 Hz, 4H), 2.65 – 2.60 (m, 6H), 2.60 – 2.58 (m, 2H), 2.58 – 2.52 (m, 6H), 2.38 – 2.29 (m, 6H), 2.22 – 2.11 (m, 4H), 2.08 – 1.96 (m, 7H), 1.68 – 1.55 (m, 4H), 1.50 – 1.37 (m, 4H), 1.34 – 1.23 (m, 12H), 1.23 – 1.15 (m, 4H);
^{13}C NMR (126 MHz, $CDCl_3$): δ 173.79, 173.42, 72.07, 61.97, 61.53, 49.42, 49.33, 49.17, 48.28, 47.24, 41.79, 39.87, 38.48, 37.33, 34.27, 34.09, 33.25, 29.70, 29.49, 29.29, 29.09, 29.06, 26.50, 26.47, 26.44, 24.93, 24.87;
MS (ESI) calcd. for $C_{43}H_{64}O_5$ $[M + Na]^+$ 683.47, found 683.6;
$[\alpha]_D^{24}$ = –13.3 (c = 0.1, $CHCl_3$).

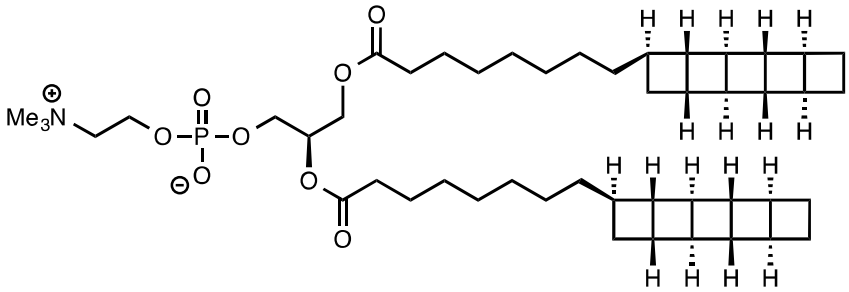

[5][5]PC:

Alcohol **S15** (8.7 mg, 13.2 μmol, 1.0 equiv.) was concentrated from toluene (ca. 1 mL) in a 5-mL pointed microwave vial. The vial was equipped with a triangular magnetic stir bar, capped with a rubber septum, and flushed with nitrogen. The residue was taken up in anhydrous toluene (264 μL, 0.05M) and the resulting solution was cooled to 0 ºC under nitrogen. Neat trimethylamine from a pressurized cylinder was introduced via a needle and ca. 200 μl was allowed to condense in the microwave vial. Freshly distilled 2-chloro-1,3,2-dioxaphospholane 2-oxide (3.6 μL, 39.5 μmol, 3.0 equiv.) was added by syringe. The resulting mixture was allowed to stir at 0 ºC for 1 hour. Reaction progress was monitored by ^{1}H NMR analysis of small aliquots.

When the reaction was complete, the flask was allowed to warm to room temperature and a stream of nitrogen was introduced to remove trimethylamine. The resulting suspension was filtered through pad of celite to remove trimethylamine hydrochloride, rinsing thoroughly with toluene (ca. 5 mL). The filtrate was concentrated in a 15-mL screw-cap pressure tube. The tube was equipped with a magnetic stir bar, capped with a rubber septum, and flushed with nitrogen. The residue was taken up in anhydrous MeCN (500 μL), and the resulting solution was cooled to –78 ºC. Neat trimethylamine was introduced as before, and ca. 1.0 mL was allowed to condense. The rubber septum was replaced quickly with a screw cap, and the reaction vessel was allowed to warm first to room temperature and then to 75 ºC in an oil bath. After 18 hours, the reaction vessel was returned to –78 ºC briefly while the screw cap was removed, then allowed to warm slowly to room temperature as excess trimethylamine evaporated. The resulting residue was purified first by flash column chromatography on silica gel to provide [**5][5]PC** (3.7 mg, 34%) as a colorless wax.

Physical properties: colorless wax;
R_f = 0.27 (silica gel, 65:15:2 DCM:MeOH:H_2O, visualized with Seebach's stain);
IR (film) ν_{max} = 2917, 2849, 1737, 1248, 1092, 6669 cm^{-1};
^{1}H NMR (600 MHz, $CDCl_3$): δ 5.20 (d, *J* = 7.3 Hz, 1H), 4.39 (d, *J* = 11.9 Hz, 1H), 4.33 (br s, 2H), 4.12 (dd, *J* = 12.1, 7.4 Hz, 1H), 3.94 (d, *J* = 6.2 Hz, 2H), 3.80 (br s, 2H), 3.35 (s, 9H), 2.72 (d, *J* = 6.0 Hz, 4H), 2.65 – 2.61 (m, 6H), 2.60 – 2.58 (m, 2H), 2.58 – 2.51 (m, 6H), 2.37 – 2.33 (m, 2H), 2.31 – 2.25 (m, 4H), 2.22 – 2.14 (m, 4H), 2.07 – 1.97 (m, 6H), 1.61 – 1.53 (m, 4H), 1.50 – 1.38 (m, 4H), 1.33 – 1.23 (m, 12H), 1.23 – 1.16 (m, 4H);
^{13}C NMR (126 MHz, $CDCl_3$): δ 173.57, 173.25, 70.43, 66.40, 63.49, 62.97, 59.30, 54.46, 49.40, 49.31, 49.16, 48.27, 47.24, 41.78, 39.89, 38.48, 37.38, 34.31, 34.12, 33.26, 29.62, 29.44, 29.40, 29.20, 29.16, 26.51, 26.47, 24.98, 24.89;
^{31}P NMR (162 MHz, $CDCl_3$) δ –1.14;
MS (ESI) calcd. for $C_{48}H_{76}NO_8P$ $[M + H]^+$ 826.54, found 826.6;
$[\alpha]_D^{24}$ = –3.8 (c = 0.31, $CHCl_3$).

[5][5]PC was also prepared from 90% ee **S1**, in this case using the phosphoramidite method to install the phosphatidylcholine headgroup; this material was found to be spectroscopically identical. In Langmuir monolayer experiments **[5][5]PC** prepared from 90% ee **S1** was employed. In all other experiments **[5][5]PC** prepared from 80% ee **S1** was employed.

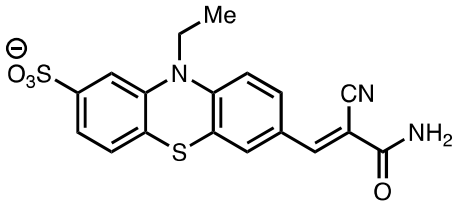

Phenothiazine Sulfonate (HS):

To the phenothiazine dinitrile parent sensor **S6** (160 mg) under nitrogen was added 5 mL fuming H_2SO_4 (20-30% free SO_3) at 0 °C. The cooling bath was removed, and the mixture was allowed to stir at room temperature for 3 hours. After this time, the reaction mixture was poured over 300 mL ice in a 500 mL Erlenmeyer flask, rinsing with cold water. Precipitated solids were collected on filter paper by passing the quenched mixture was through a Hirsch funnel attached to a vacuum flask. The filtrate was passed through the same filter to capture additional crude solid. This process was repeated 3 times until the filtrate appeared homogeneous. Vacuum was applied on the filter flask until residual ice in the funnel had melted and the residue was dry. The Hirsch funnel was connected to a clean vacuum flask. Methanol was repeatedly poured over the filter paper now bearing a rust-colored residue and vacuum was applied in order to wash the crude product through. The resulting methanolic filtrate was concentrated *in vacuo*. The resulting crude purple/black tar was purified by flash column chromatography on silica gel (0 to 30% methanol/dichloromethane) followed by preparatory thin layer chromatography (25% methanol/dichloromethane) to provide the phenothiazine sulfonate hydrazine sensor (**HS**) (22.4 mg, 8.5%) as a red-orange solid.

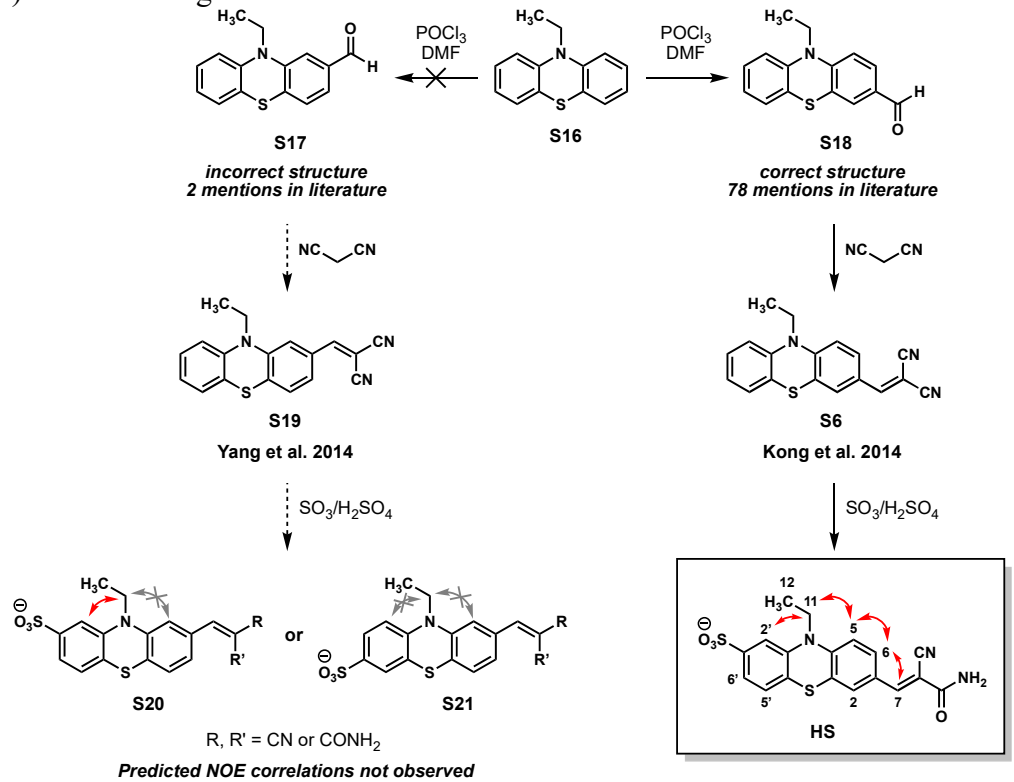

Supplementary Scheme S5. Structural determination of **HS** based on NMR and literature evidence.

Sun *et al.* originally described structure **S19** (Supplementary Scheme S5) as a hydrazine sensor, which would arise from aldehyde **S17**.[8] NMR experiments and an examination of the literature allowed us to reassign **S19** to structure **S6**, which would derive from aldehyde **S18**. Vilsmeier-Haak carbonylation of **S16** proceeds *para* to nitrogen, not *para* to sulfur. The difference between our structure for dicyanoalkene S6 (first described by Kong *et al*.) and **S19** reported Sun *et al*. is the position of the dicyanoethenyl group relative to the N and S atoms.[11]

On the sulfonate **HS**, the alkenyl group can be assigned to a ring system containing three aromatic protons (H2, H5, H6) by NOESY peaks correlating H7 to H2 and H5, and by ^{1}H J-coupling and COSY peaks between H2, H5 and H6 acquired in CD_3OD. The J-coupling constants and COSY peaks suggest a 1,3,4-trisubstituted benzene ring. In our structure for **HS**, one would expect to see a NOESY peak correlating the ethyl CH_2 (H11) to a proton split by *ortho* coupling (H5), which is observed. In hypothetical sulfonated **S20** and **S21**, which would arise from sulfonation of **S19**, the ethyl CH_2 would correlate to a proton both split by weak *meta* coupling and proximal to an alkenyl group, which is not observed. ^{1}H-^{13}C HMBC correlations agree with these assignments.

The position of the sulfonate is determined using similar logic. The selectivity of sulfonation for the 1' position can be rationalized by considering the deactivating effect of the dicyanoethenyl group on the N atom, leaving the S atom to function as a *para*-directing group. Although the presence of one amide group is evident from IR spectroscopy and mass spectrometry, the *E* geometry of the alkene is assigned only tentatively based on predicted steric destabilization of the corresponding *Z* alkene.

Physical properties: red-orange solid;
R_f = 0.40 (silica gel, 75:25 DCM:MeOH, visible by eye as a yellow spot) (note: multiple orange product bands appear on prep TLC, likely varying countercation);
IR (film) ν_{max} = 3442, 2929, 2214, 1673, 1569, 1471, 1410, 1215, 1187, 1138, 1037, 805, 662, 616 cm^{-1};
^{1}H NMR (500 MHz, CD_3OD) δ 8.03 (s, 1H), 7.83 (dd, *J* = 8.7, 2.2 Hz, 1H), 7.73 (d, *J* = 2.2 Hz, 1H), 7.44 (d, *J* = 1.7 Hz, 1H), 7.42 (dd, *J* = 7.9, 1.7 Hz, 1H), 7.14 (d, *J* = 7.9 Hz, 1H), 7.09 (d, *J* = 8.7 Hz, 1H), 4.05 (q, *J* = 7.0 Hz, 2H), 3.18 (q, *J* = 7.3 Hz, 6H), 1.44 (t, *J* = 7.0 Hz, 3H), 1.30 (t, *J* = 7.3 Hz, 9H);
^{13}C NMR (126 MHz, CD_3OD) δ 165.86, 151.57, 149.71, 146.16, 144.12, 132.75, 129.75, 127.87, 127.61, 126.77, 124.87, 122.01, 117.83, 116.27, 114.30, 102.67, 43.42, 12.95;
MS (ESI) m/z calcd. for $C_{18}H_{14}N_3O_4S_2^-$ $[M - H]^-$ 400.0, found 400.1.

5. ^{1}H, ^{13}C, and 2D NMR Spectra

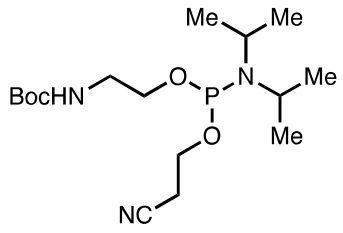

S7

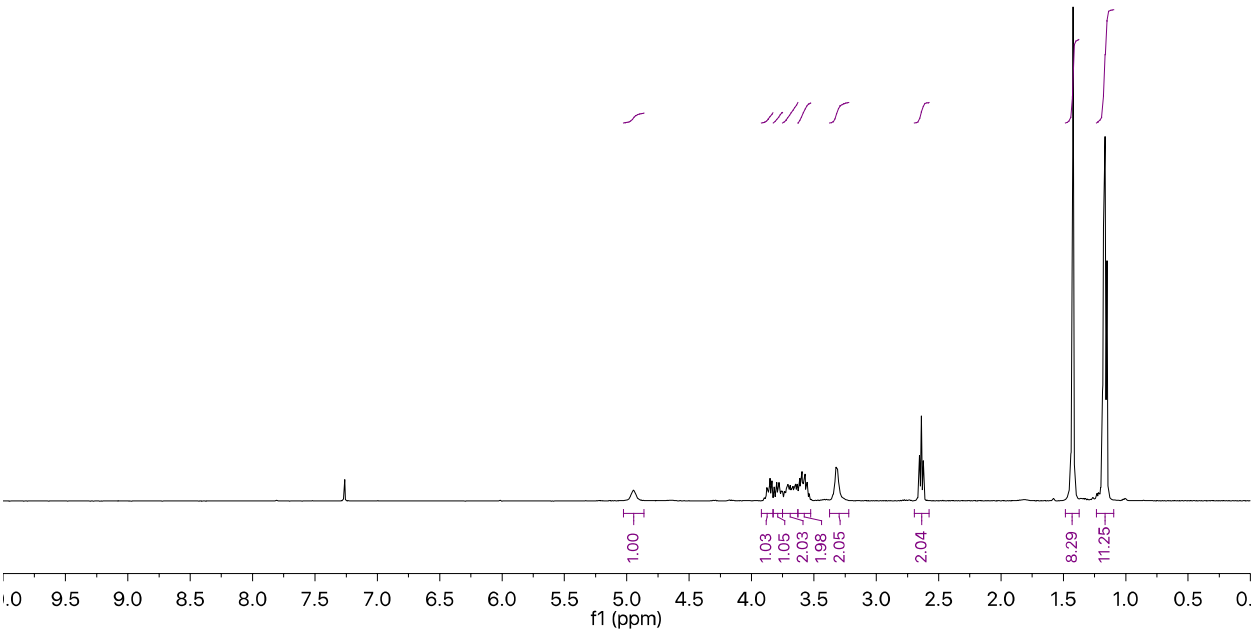

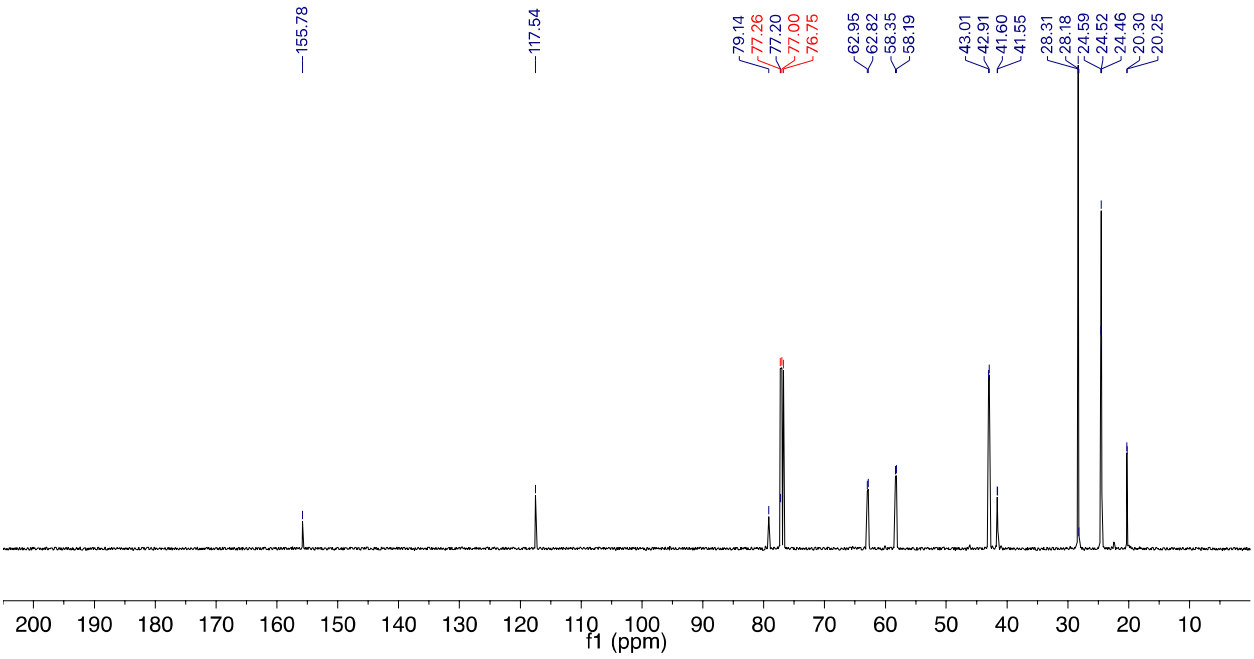

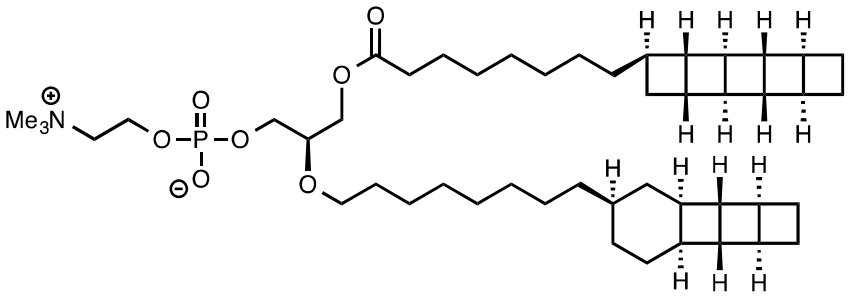

[5][3]PC

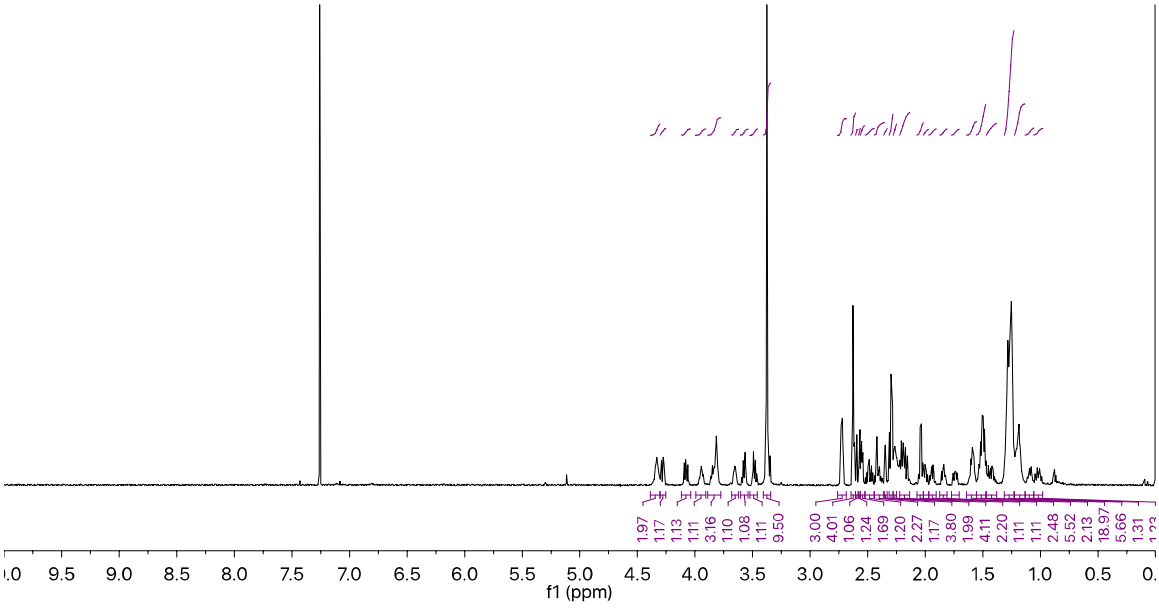
1.97
1.17
1.13
1.11
3.16
1.10
1.08
1.11
9.50
3.00
4.01
1.06
1.24
1.69
1.20
2.27
1.17
3.80
1.99
4.11
2.20
1.11
1.11
2.48
5.52
2.13
18.97
5.66
1.31
f1 (ppm)

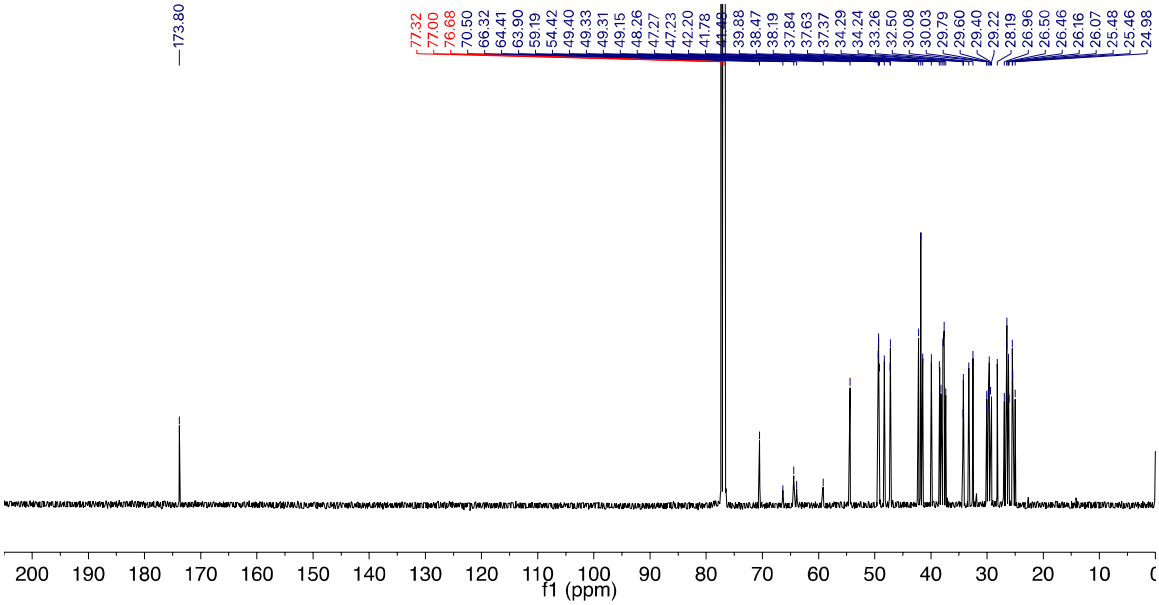
173.80
77.32
77.00
76.68
70.50
66.32
64.41
63.90
59.19
54.42
49.40
49.33
49.31
49.15
48.26
47.27
47.23
42.20
41.78
39.88
38.47
38.19
37.84
37.63
37.37
34.29
34.24
33.26
32.50
30.08
30.03
29.79
29.60
29.40
29.22
28.19
26.96
26.50
26.46
26.16
26.07
25.48
25.46
24.98
f1 (ppm)

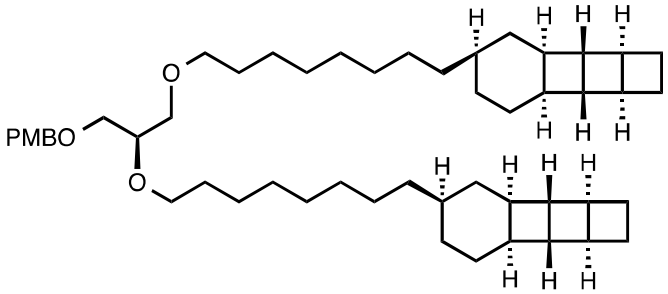
PMBO
O
O
H

S10

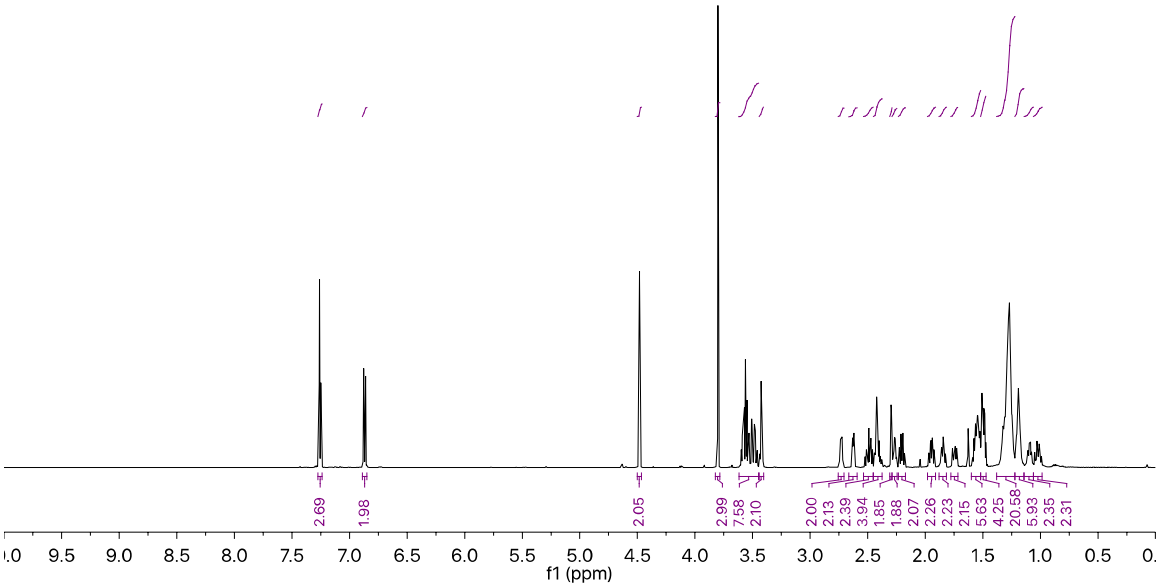
2.69
1.98
2.05
2.99
7.58
2.10
2.00
2.13
2.39
3.94
1.85
1.88
2.07
2.26
2.23
2.15
5.63
4.25
20.58
5.93
2.35
2.31
f1 (ppm)

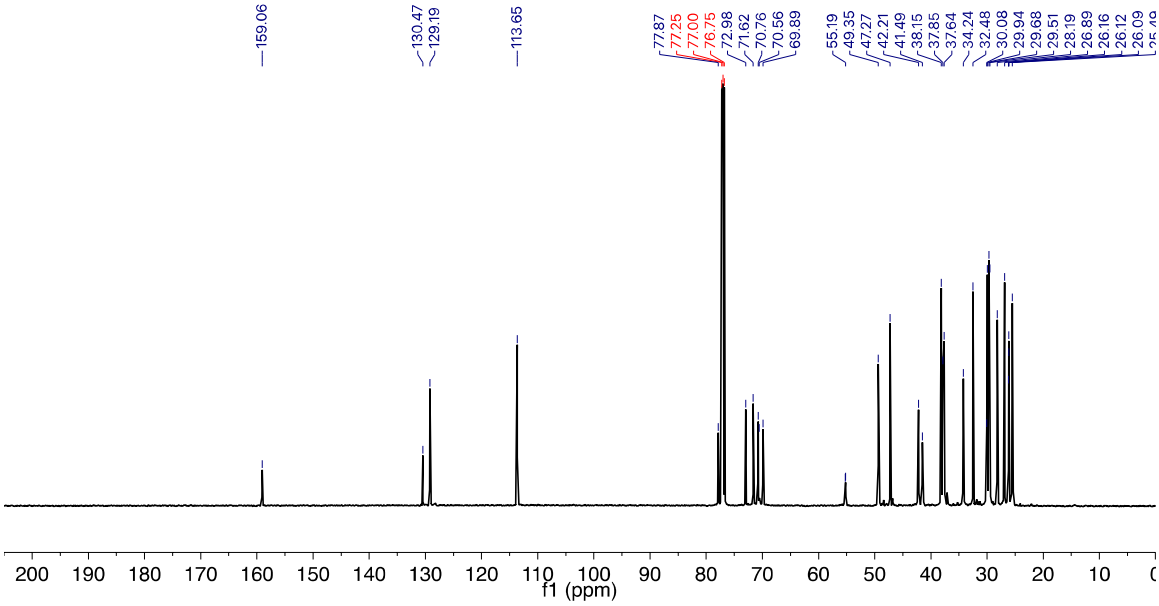
159.06
130.47
129.19
113.65
77.87
77.25
77.00
76.75
72.98
71.62
70.76
70.56
69.89
55.19
49.35
47.27
42.21
41.49
38.15
37.85
37.64
34.24
32.48
30.08
29.94
29.68
29.51
28.19
26.89
26.16
26.12
26.09
f1 (ppm)

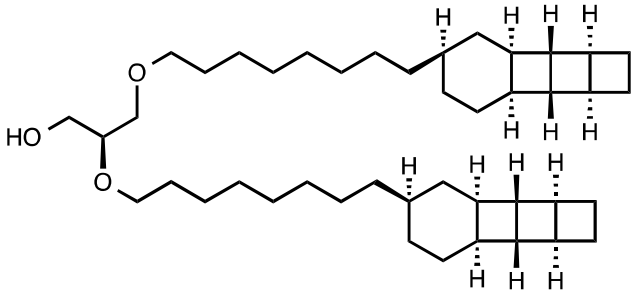
HO
O
O
H

S11

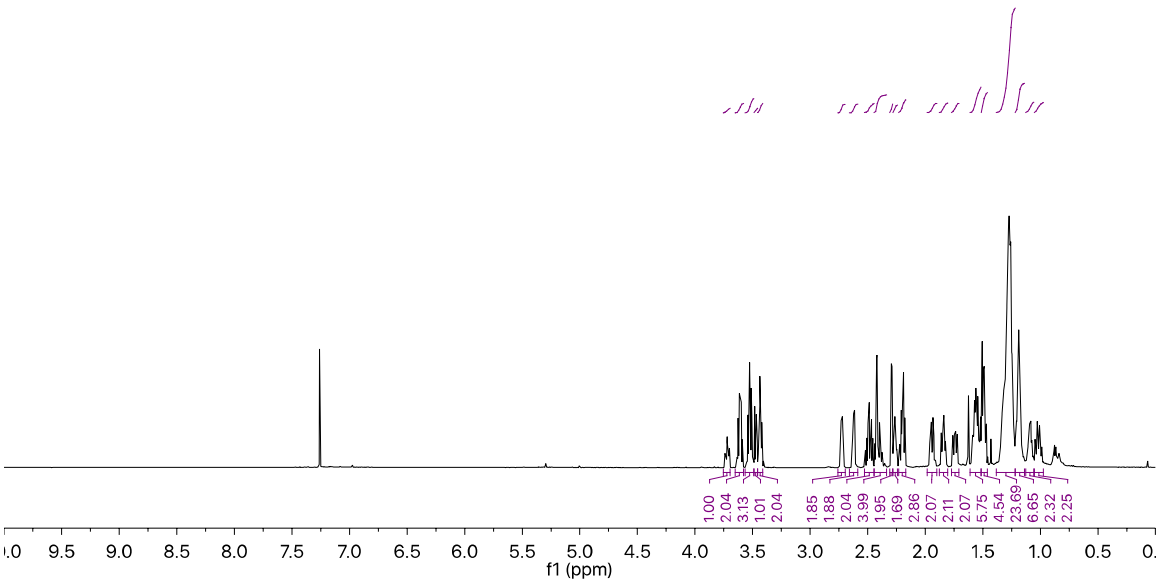
1.00
2.04
3.13
1.01
2.04
1.85
1.88
2.04
3.99
1.95
1.69
2.86
2.07
2.11
2.07
5.75
4.54
23.69
6.65
2.32
2.25
f1 (ppm)

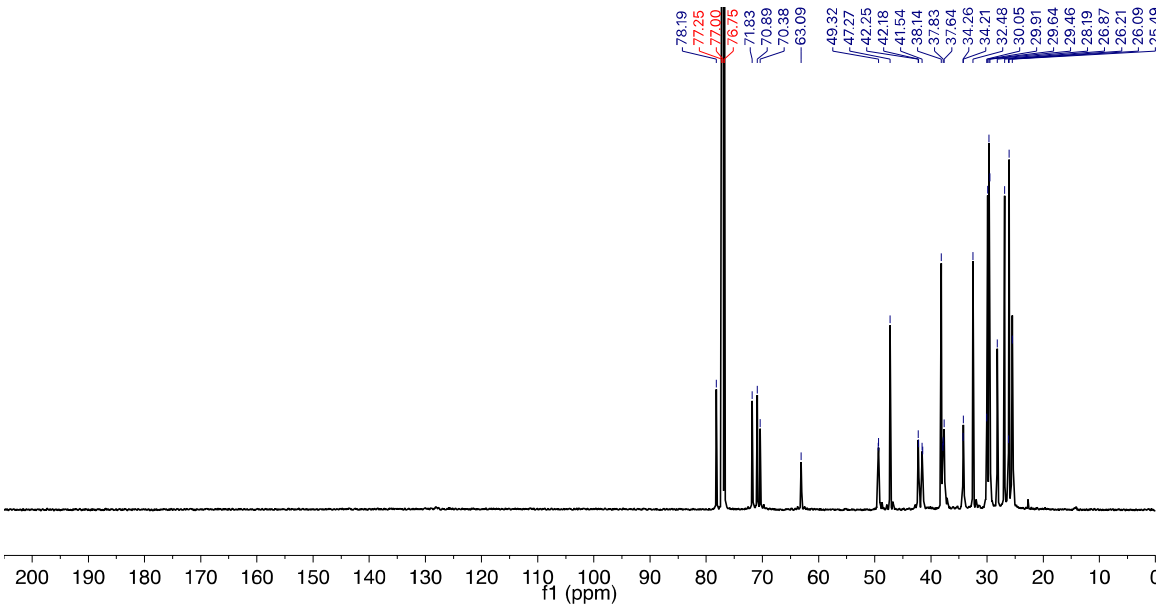
78.19
77.25
77.00
76.75
71.83
70.89
70.38
63.09
49.32
47.27
42.25
42.18
41.54
38.14
37.83
37.64
34.26
34.21
32.48
30.05
29.91
29.64
29.46
28.19
26.87
26.21
26.09
f1 (ppm)

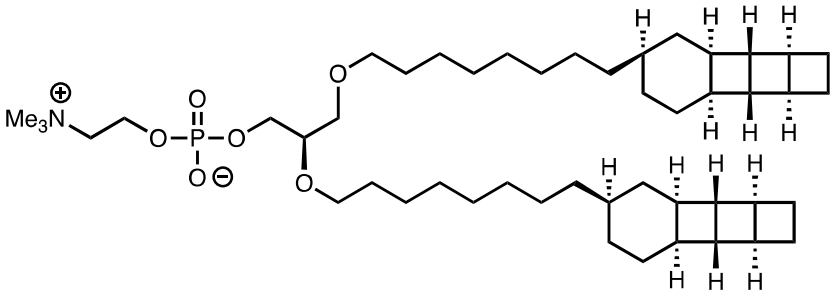

[3][3]PC

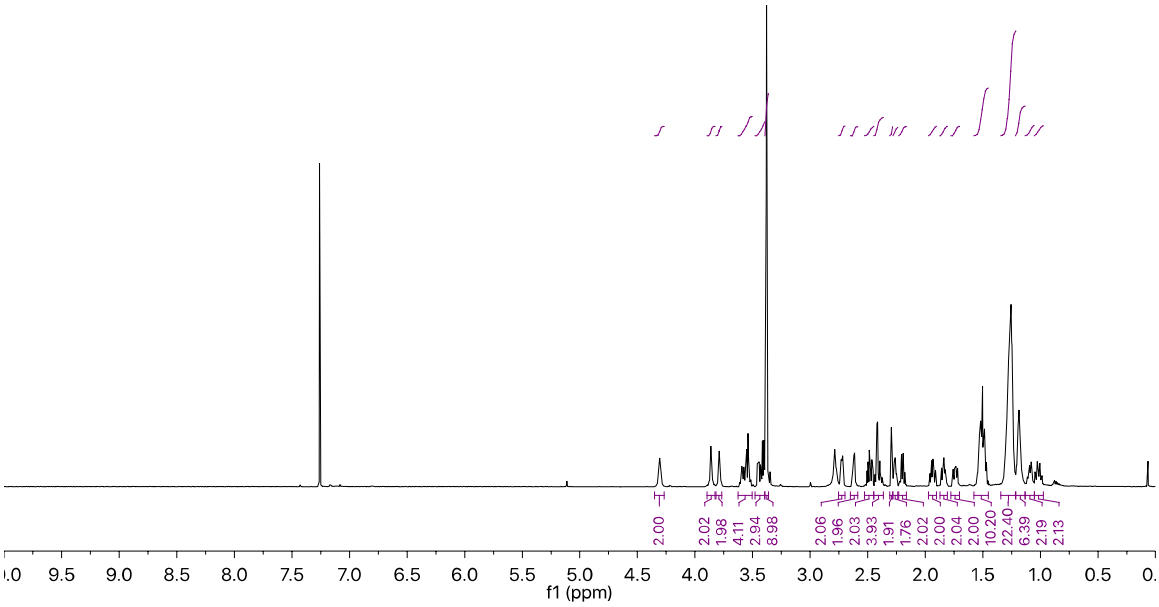
2.00
2.02
1.98
4.11
2.94
8.98
2.06
1.96
2.03
3.93
1.91
1.76
2.02
2.00
2.04
2.00
10.20
22.40
6.39
2.19
2.13
f1 (ppm)

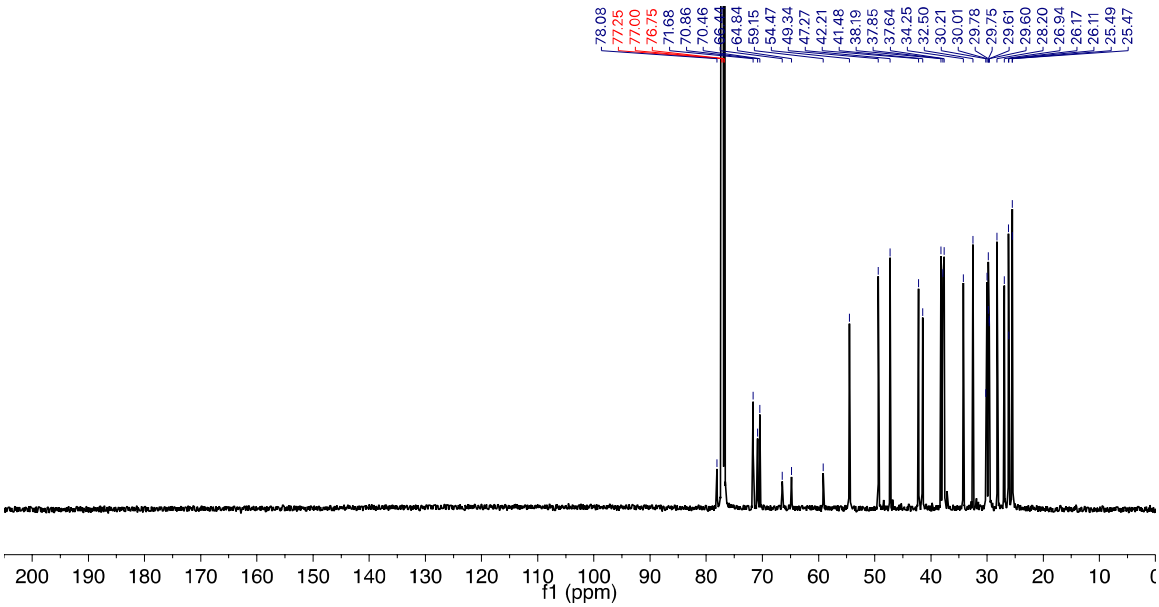
78.08
77.25
77.00
76.75
71.68
70.86
70.46
64.84
59.15
54.47
49.34
47.27
42.21
41.48
38.19
37.85
37.64
34.25
32.50
30.21
30.01
29.78
29.75
29.61
29.60
28.20
26.94
26.17
26.11
25.49
25.47
f1 (ppm)

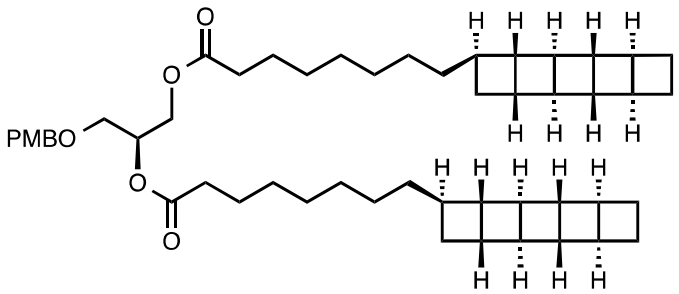
PMBO
O
O
O
O
H H H H H
H H H H
H H H H H
H H H H

S14

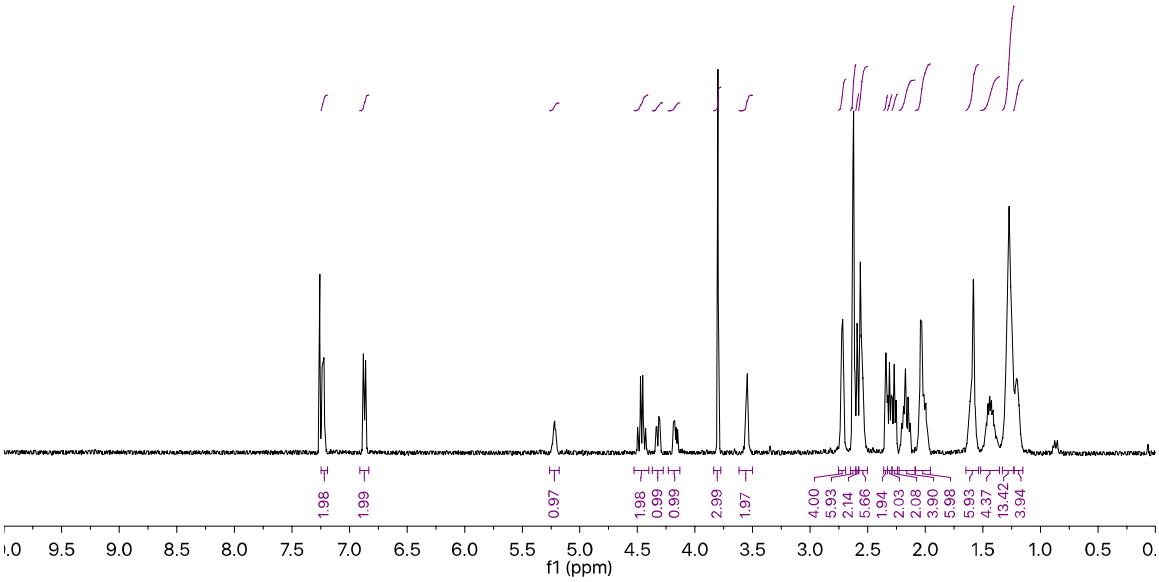
1.98
1.99
0.97
1.98
0.99
0.99
2.99
1.97
4.00
5.93
2.14
5.66
1.94
2.03
2.08
3.90
5.98
5.93
4.37
13.42
3.94
f1 (ppm)

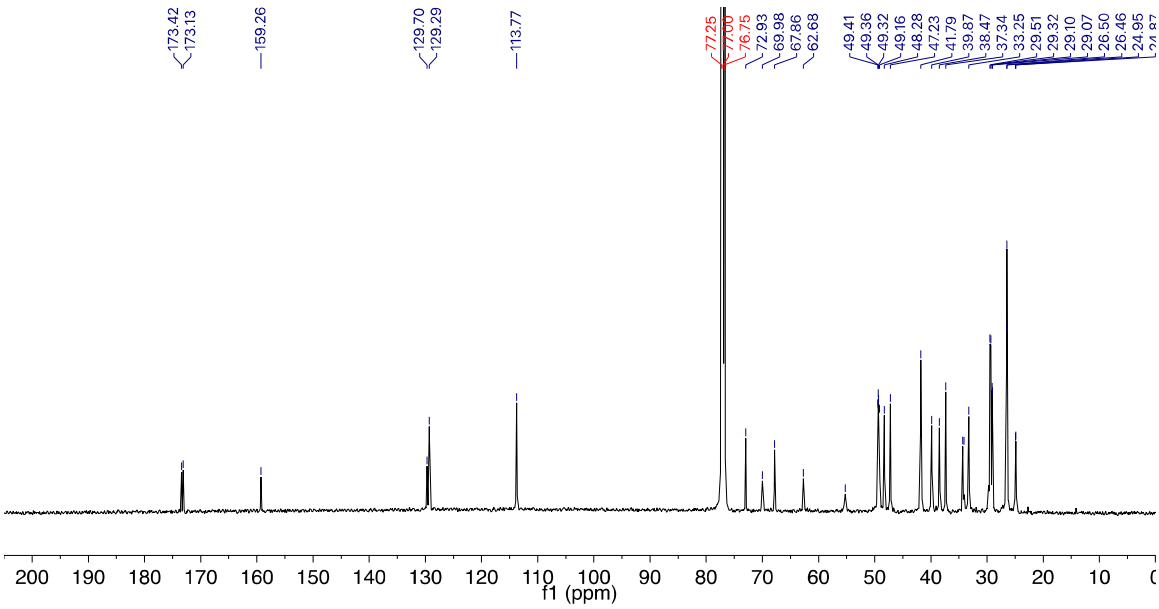
173.42
173.13
159.26
129.70
129.29
113.77
77.25
77.00
76.75
72.93
69.98
67.86
62.68
49.41
49.36
49.32
49.16
48.28
47.23
41.79
39.87
38.47
37.34
33.25
29.51
29.32
29.10
29.07
26.50
26.46
24.95
f1 (ppm)

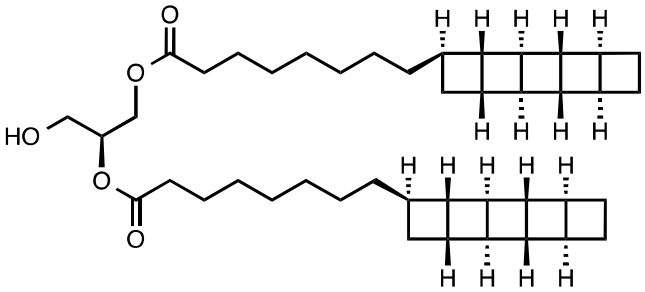

S15

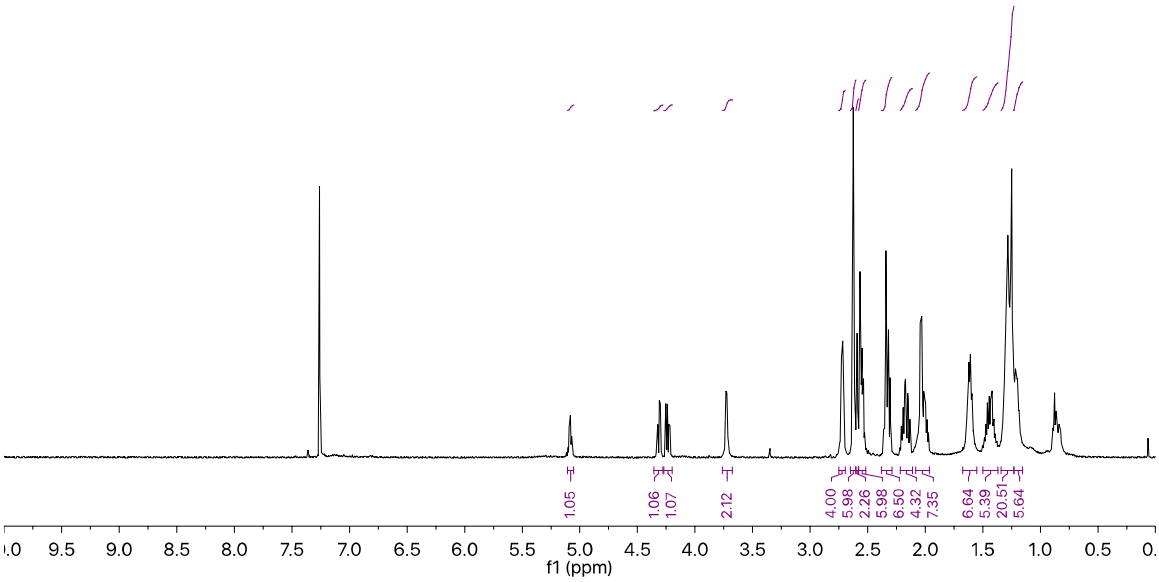
1.05
1.06
1.07
2.12
4.00
5.98
2.26
5.98
6.50
4.32
7.35
6.64
5.39
20.51
5.64
f1 (ppm)

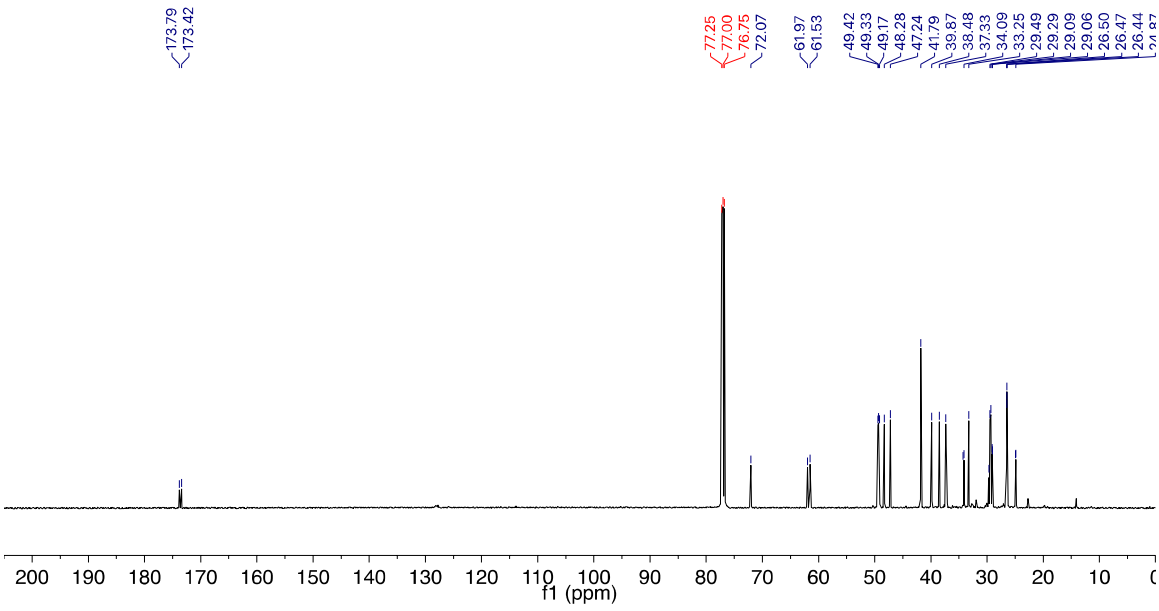
173.79
173.42
77.25
77.00
76.75
72.07
61.97
61.53
49.42
49.33
49.17
48.28
47.24
41.79
39.87
38.48
37.33
34.09
33.25
29.49
29.29
29.09
29.06
26.50
26.47
26.44
f1 (ppm)

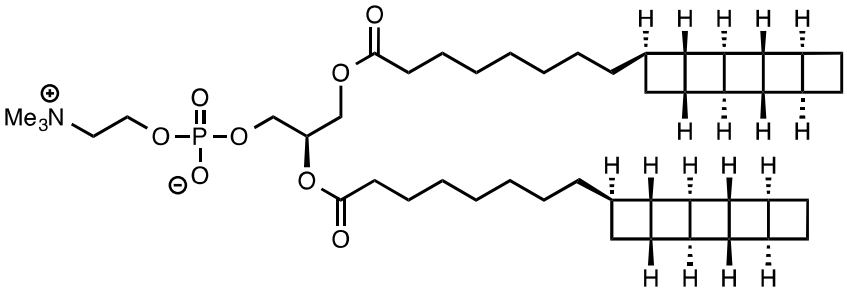

[5][5]PC

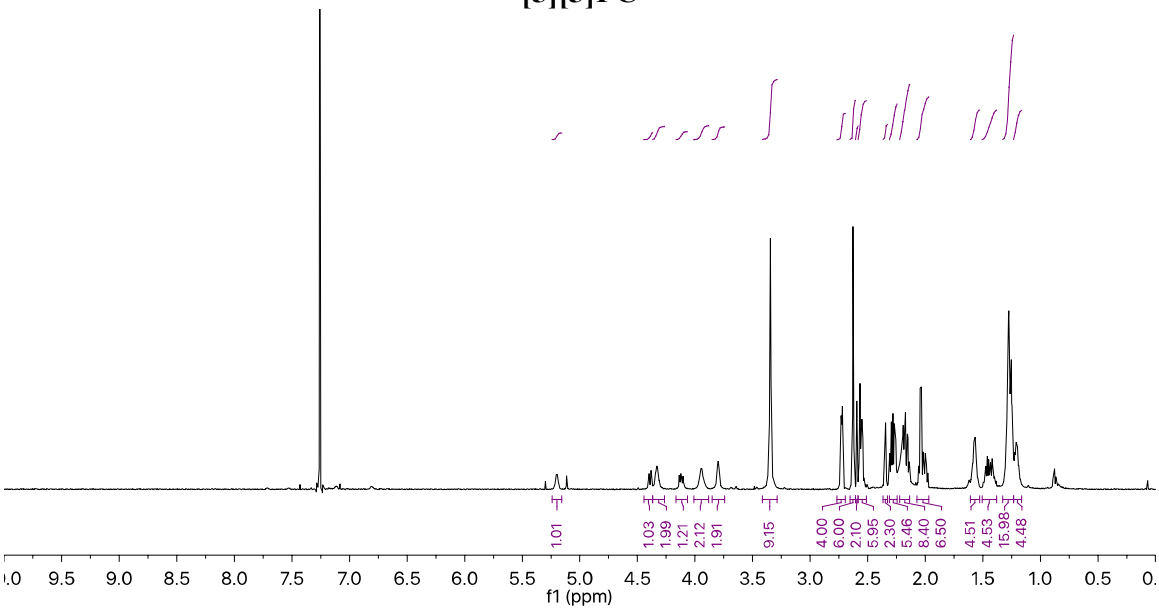
1.01
1.03
1.99
1.21
2.12
1.91
9.15
4.00
6.00
2.10
5.95
2.30
5.46
8.40
6.50
4.51
4.53
15.98
4.48
f1 (ppm)

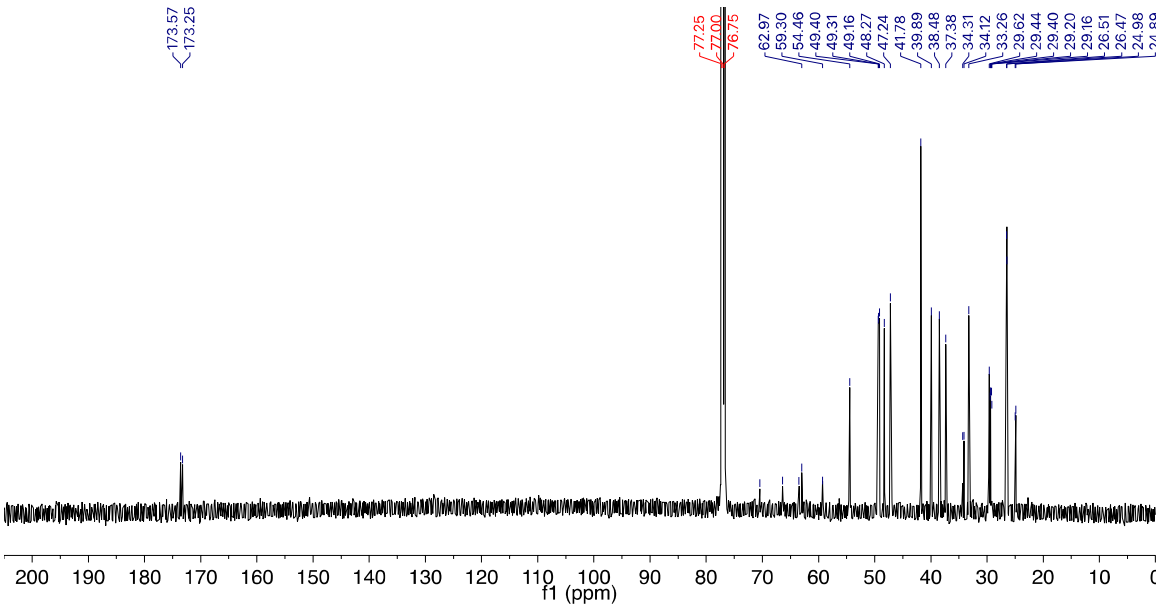
173.57
173.25
77.25
77.00
76.75
62.97
59.30
54.46
49.40
49.31
49.16
48.27
47.24
41.78
39.89
38.48
37.38
34.31
34.12
33.26
29.62
29.44
29.40
29.20
29.16
26.51
26.47
f1 (ppm)

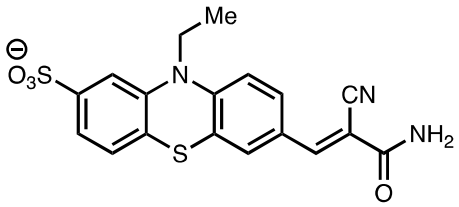
Me
N
S
CN
NH2
O
O3S

HS

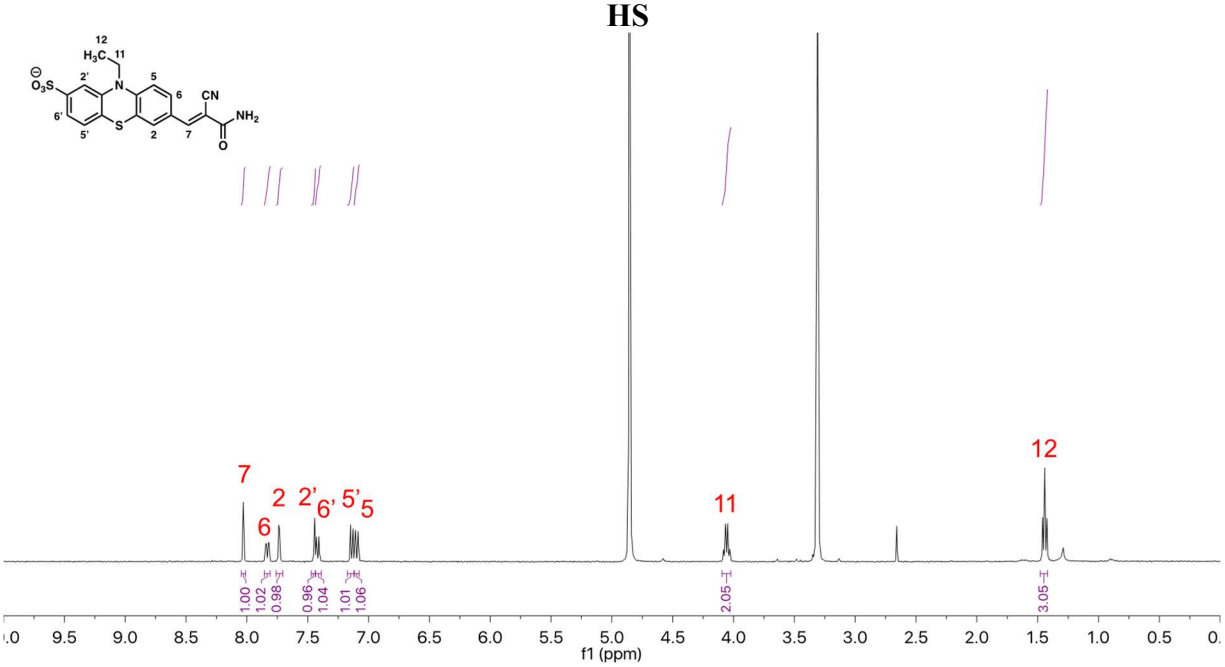
7
6
2
2'
6'
5'
5
11
12
1.00
1.02
0.98
0.96
1.04
1.01
1.06
2.05
3.05
f1 (ppm)

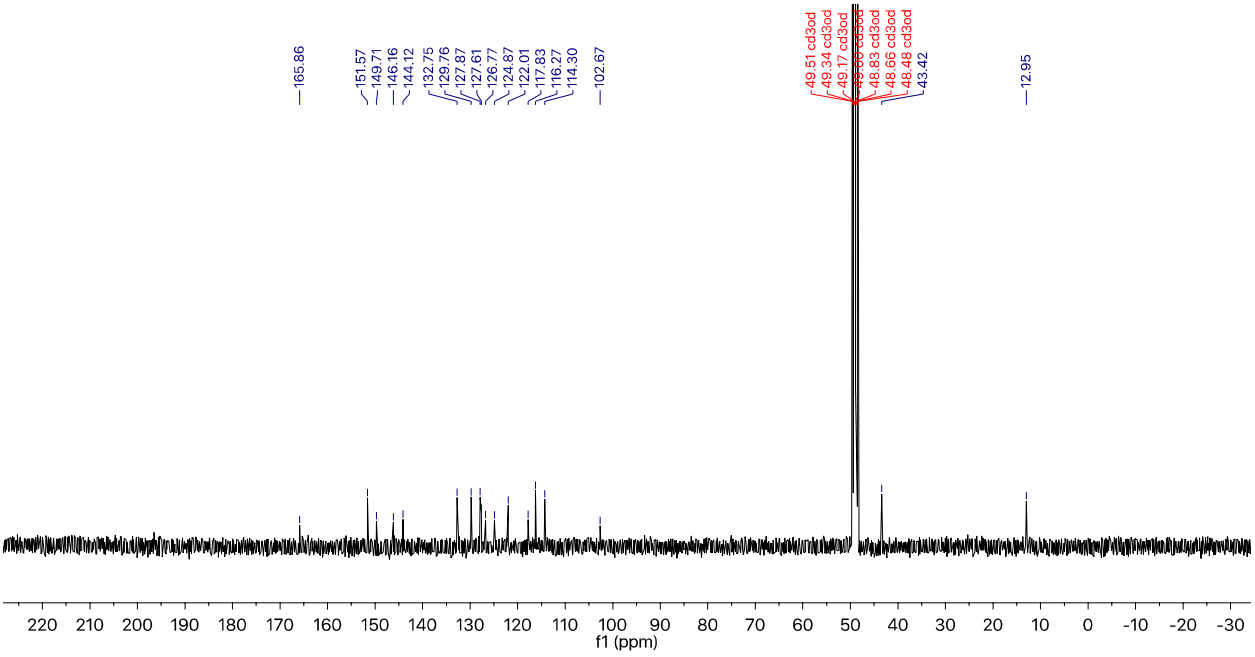
165.86
151.57
149.71
146.16
144.12
132.75
129.76
127.87
127.61
126.77
124.87
122.01
117.83
116.27
114.30
102.67
49.51 cd3od
49.34 cd3od
49.17 cd3od
48.83 cd3od
48.66 cd3od
48.48 cd3od
43.42
12.95
f1 (ppm)

^{1}H COSY, 600 MHz, CD_3OD

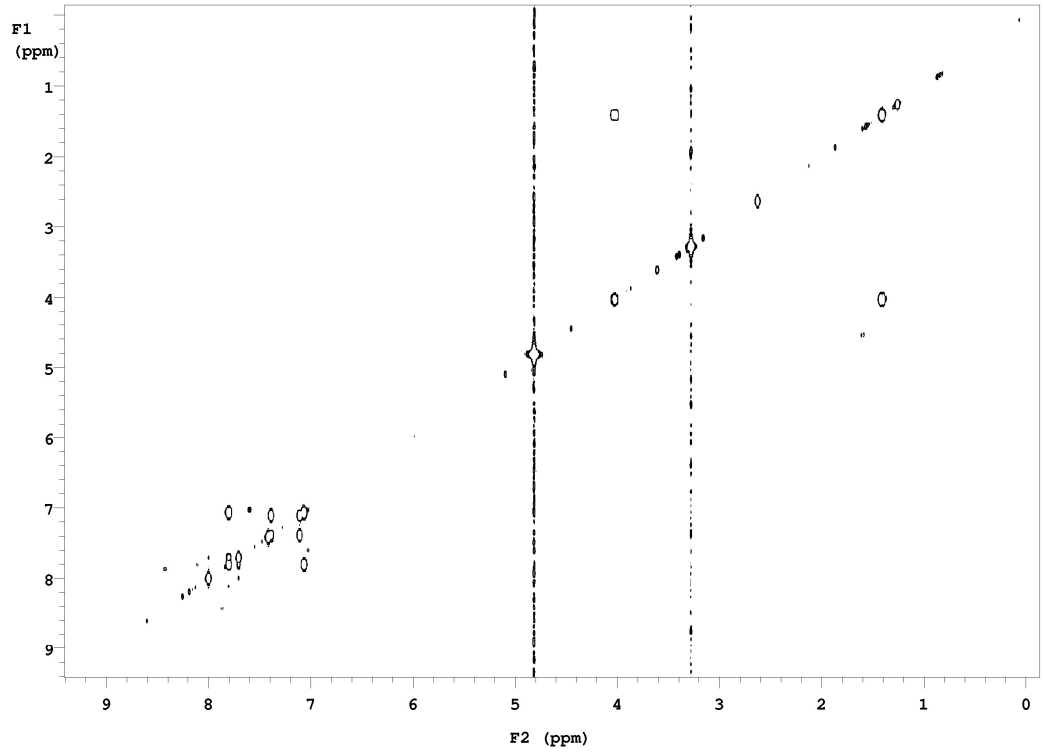

^{1}H NOESY, 600 MHz, CD_3OD

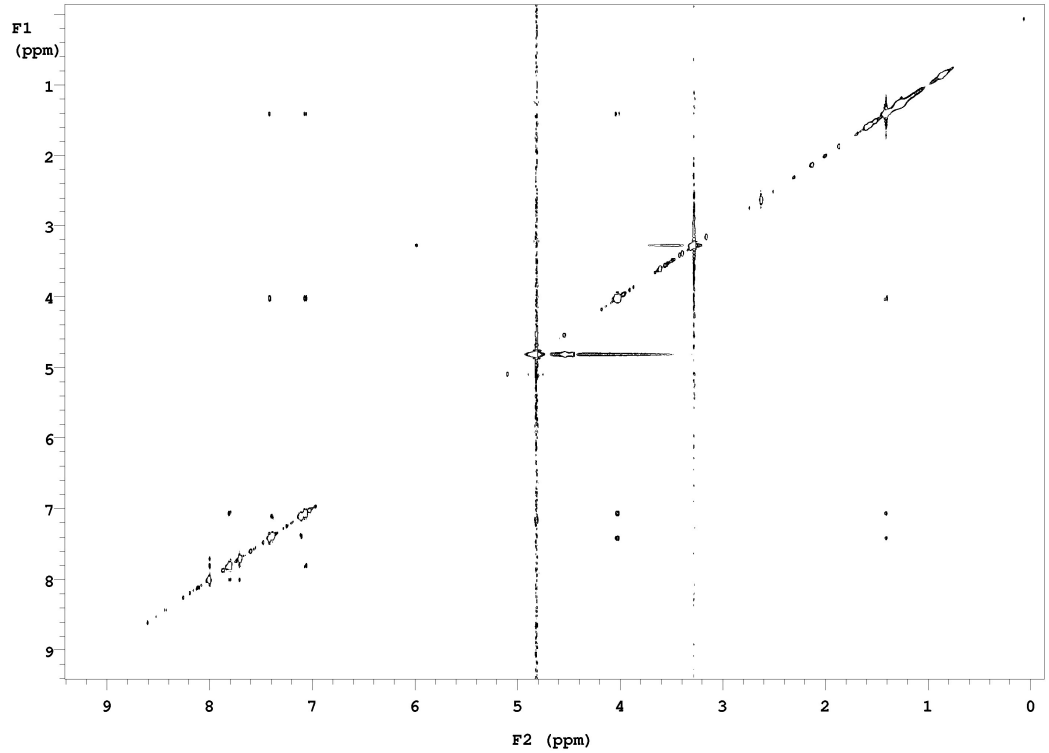

^{1}H NOESY, 600 MHz, CD_3OD (zoom)

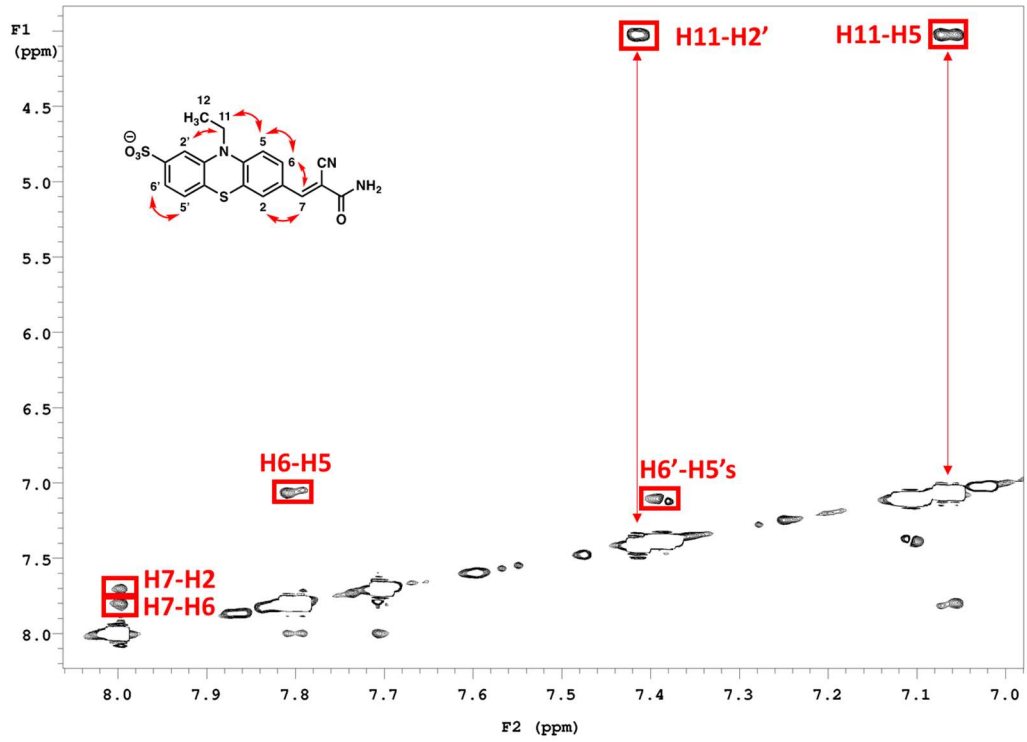

^{1}H-^{13}C HSQC, 600 MHz, CD_3OD

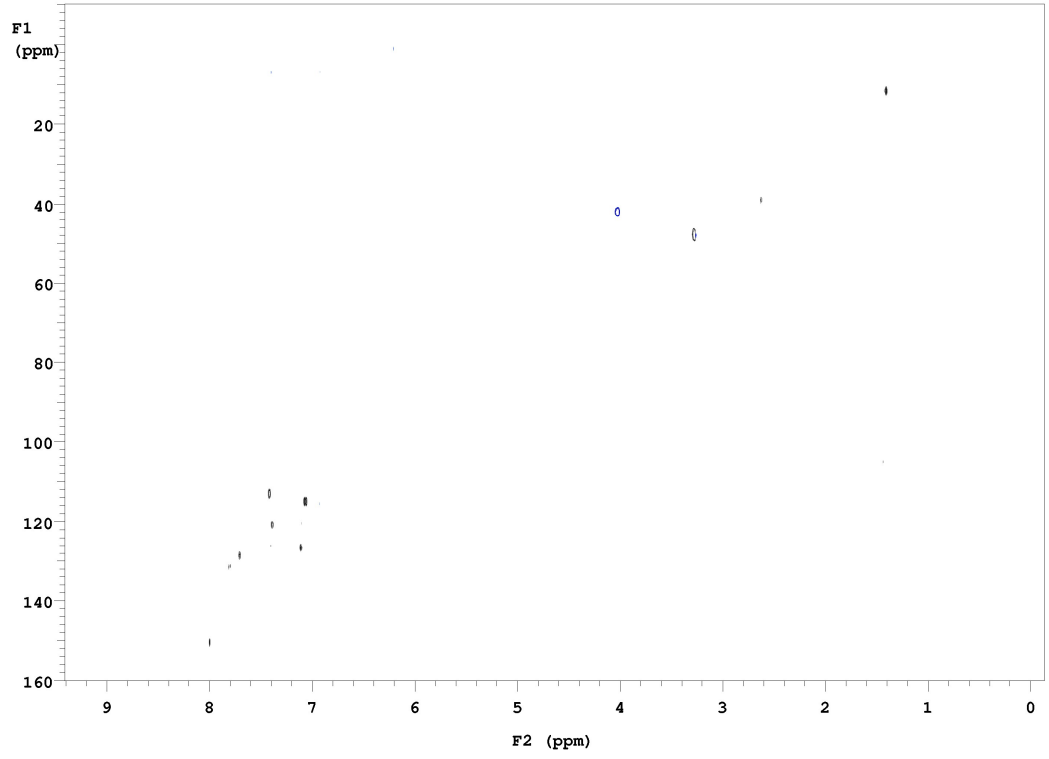

^{1}H-^{13}C HMBC, 600 MHz, CD_3OD

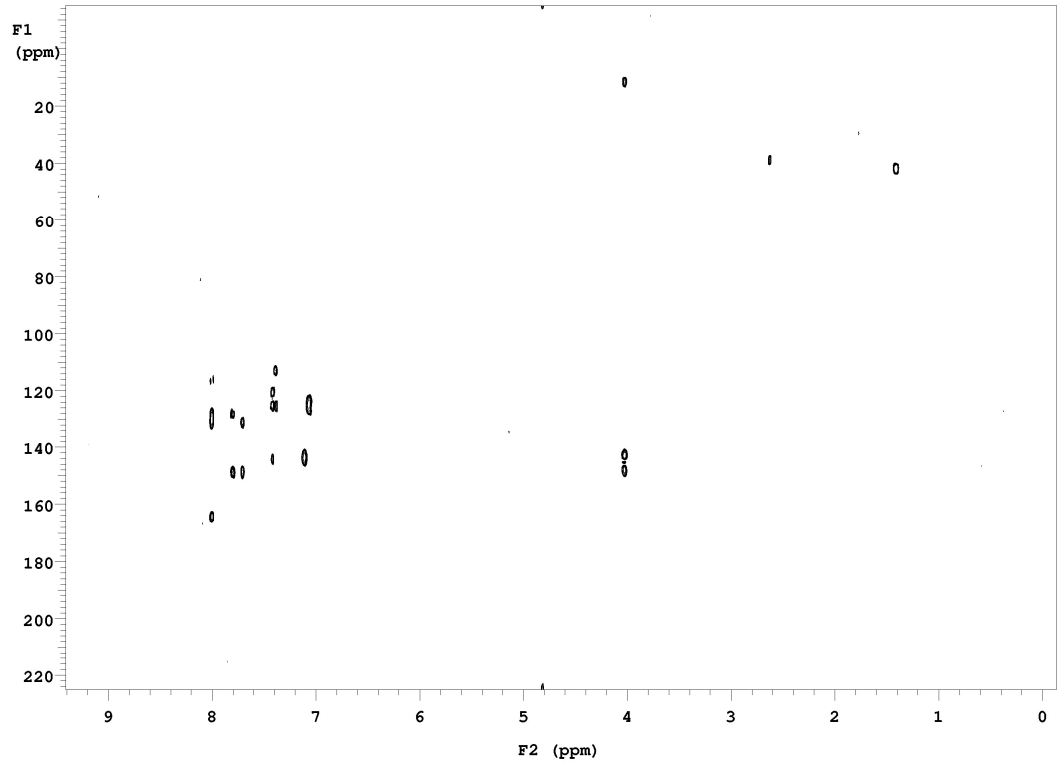

6. Biophysical Studies General Information

All straight-chain lipids were from Avanti Polar Lipids (Alabaster, AL) and used as supplied. Texas Red 1,2-dihexadecanoyl-*sn*-glycero-3-phosphoethanolamine (Texas Red DHPE), DiI, and Oregon Green 488 1,2-dihexadecanoyl-*sn*-glycero-3-phosphoethanolamine (Oregon Green DHPE) were from Thermo Fisher Scientific. Solvents were ACS grade and used as used as received unless otherwise noted. All water used was from a Millipore (Billerica, MA) MilliQ system with a resistivity of ~ 18.2 MΩ·cm. The concentrations of ladderane lipid stock solutions were determined by performing LC-MS with 12:0-13:0 PC as an internal standard.

The solutions called "420 μM HS," "50 mM phosphate buffer," and "hydrazine buffer" were prepared as follows. To prepare 50 mM phosphate (500 mOsM) buffer preparation, 6.0 g of monobasic sodium phosphate was dissolved in 1 L MilliQ water to make a 50 mM solution. The pH of the solution was raised to 7.40 or 6.30 by addition of 5 N NaOH (typically 9 mL). Depending on the amount of NaOH added, NaCl was added (typically 10 g) to form a 500 mOsM buffer.

For assays involving hydrazine, oxygen was removed from water prior to use as described here. Loosely capped Falcon tubes containing 45 mL of buffer or MilliQ water were placed in a desiccator and house vacuum was applied overnight. The desiccator was then filled with argon by first capping the inlet with a rubber septum, then piercing the septum with two argon-filled balloons with attached needles, then simultaneously closing the desiccator valve to vacuum and opening the desiccator valve to the inlet. The desiccator top was removed, and the Falcon tubes quickly closed and sealed with Parafilm.

To prepare the hydrazine buffer preparation, 425-430 mg of hydrazine hydrochloride was weighed and dispensed into a 25-mL reagent bottle pre-filled with argon. The bottle was then purged of air with a stream of argon and closed. 25 mL degassed MilliQ water was added to the bottle, along with 300 μL 5 N NaOH, under a stream of argon. The bottle was closed and shaken vigorously. The pH was then adjusted to 7.40 ± 0.02 with 5N NaOH, purged of air with argon immediately after each time the pH was measured with a glass electrode. The bottle was purged of air with a stream of argon, closed, and sealed with Parafilm.

Buffer A and B in the pH equilibration studies were prepared as follows. Buffer A was 100 mM NaCl, 10 mM bis tris propane, pH = 7.2. Buffer B was 100 mM NaCl, 10 mM bis-tris propane, pH = 5.8. The pH of buffers was adjusted with concentrated HCl or 1 M NaOH, and buffers were submicron filtered prior to use.

7. Gentle Hydration and Fluorescence Microscopy

Giant unilamellar vesicles (GUVs) were formed with the gentle hydration method. 100 nmol of the desired lipid mixtures in chloroform were mixed with 0.1% Texas Red DHPE or DiI in glass vials. Thin lipid films were prepared by evaporating the chloroform under a gentle stream of argon while rotating the vials. Vials with lipid films were placed under vacuum for at least 4 hours to remove residual solvent. 1 mL of 500 mM sucrose was gently added to each vial. Vials of PCs that are fluid at room temperature were incubated at 37°C overnight, and vials of PCs that are solid at RT were incubated overnight at 70°C. After incubation vials were cooled to room temperature and gently agitated to resuspend GUVs. 10-20 µL of vesicle solution was gently pipetted into wells containing 200 µL of 500 mM glucose in a PDMS gasket bonded to a glass microscope cover slip. After allowing the GUVs to sink for at least 10 minutes, they were imaged with a Nikon Ti-U inverted epifluorescence microscope with a 100X oil immersion objective (Nikon Instruments, Melville, NY; NA-1.49) equipped with an Andor iXon 897 camera (Andor Technology, Belfast, United Kingdom). Standard emission and excitation filters for Texas Red (ex = 562/40 nm, bs = 593 nm, em = 624/40 nm) and Oregon Green (ex = 475/35 nm, bs = 509 nm, em = 528/38 nm) were used (Chroma Technology Corp., Bellows Falls, VA). Metamorph (Molecular Devices, Sunnyvale, CA) was used to acquire images, and images were processed with ImageJ (National Institutes of Health, USA).

In order to confirm that the objects observed with fluorescence microscopy for ladderane lipids were true GUVs, we encapsulated the water-soluble dye carboxyfluorescein (CF). Dried **[5][3]PC** lipid films were rehydrated with 250 mM sucrose containing 42 µM CF. After overnight gentle hydration, 20 µL of the GUV solution was added to 200 µL of 250 mM glucose. Vesicles were imaged with the Texas Red and Oregon Green filter sets. Images were false colored and merged to examine localization of the two dyes. Supplementary Fig. S3G-H shows that CF fluorescence is clearly localized to the interior of the GUVs, proving that they have an aqueous interior and are vesicles. As is expected for the gentle hydration method of GUV formation, multilamellar and multivesicular vesicles are often observed among clean GUVs.[12] We note that GUVs are not used in further biophysical characterization. SUVs are used for proton and hydrazine transmembrane diffusion assays, and we demonstrate aqueous interiors for these vesicles by CF encapsulation and unilamellarity by small angle X-ray scattering (SAXS) and protonophore insertion (see Sections 9 and 13 for details).

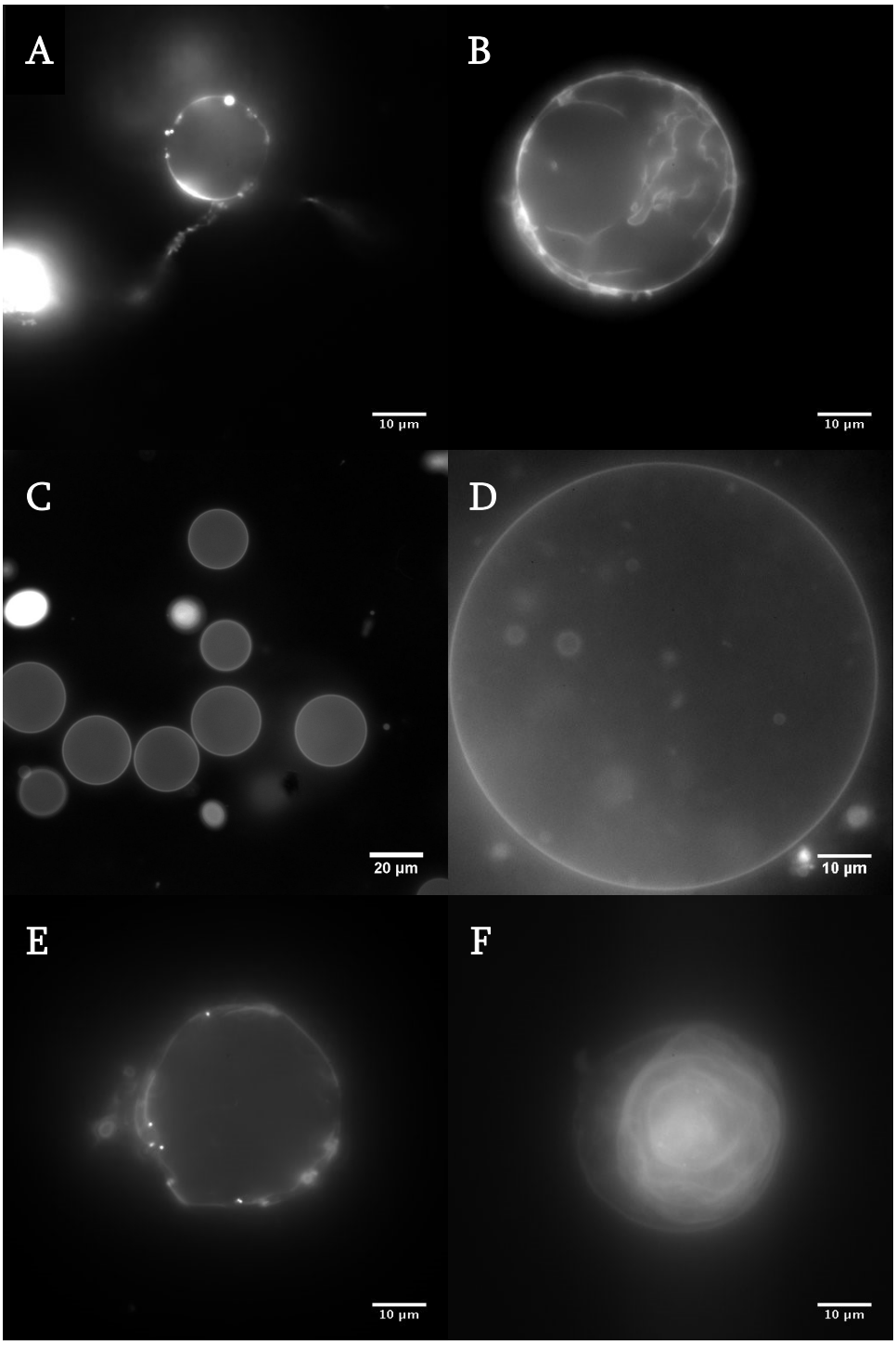
A
10 µm
B
10 µm
C
20 µm
D
10 µm
E
10 µm
F
10 µm

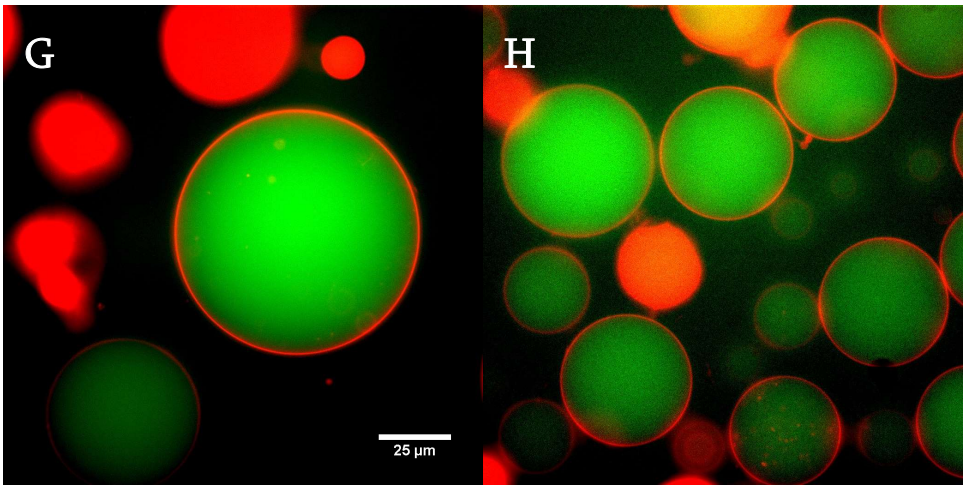

Supplementary Figure S3. Fluorescence images of gently hydrated PCs incubated at elevated temperature then cooled to room temperature. (A–B) Hydrated **di20:0 PC (DAPC)** (0.1 mol% **DiI**) incubated at 70 °C then cooled to room temperature. (C–D) Hydrated **[5][3]PC** (0.1 mol% **Texas Red-DHPE**) incubated at 37 °C then cooled to room temperature. (E–F) Hydrated **[5][5]PC** (0.1 mol% **Texas Red-DHPE**) incubated at 70 °C then cooled to room temperature. (G-H) Hydrated **[5][3]PC** (0.1 mol% **Texas Red-DHPE** (red), encapsulating 42 µM carboxyfluorescein (green)) incubated at 37 °C then cooled to room temperature.

8. Differential Scanning Calorimetry (DSC)

Multilamellar lipid dispersions were prepared by adding either 40 µl of 1:1 ethylene glycol: buffer* (240 mM NaCl + 10 mM NaH_2PO_4) or 40 µL buffer (240 mM NaCl + 10 mM NaH_2PO_4) to a 1 mg PC lipid film dried from a chloroform solution and then sonicating in a bath set to 69 °C for 5 minutes. 25 µl of each suspension was loaded into a 40 µl T-Zero aluminum pan (TA Instruments, New Castle, DE) and hermetically sealed. Calorimetric scans were performed in a TA Instruments Q2000 DSC (temperature accuracy = ±0.1 °C) using an empty T-Zero aluminum pan as a reference at a scan rate of 10 °C/min. For each sample, a scan from –20 °C to 80 °C was performed to locate T_m, and then scans centered around T_m with a range of 30 °C were performed in quadruplicate to measure T_m. In the case of **[5][3]PC**, a manual baseline correction was performed in Microsoft Excel: the points at 8 °C and 20 °C were fit to a linear function, and the values of the function were subtracted at all points in-between. Data were analyzed manually in Microsoft Excel using the =MIN function to locate T_m for each scan.

Results

LIPID	T_m (°C) (1:1 ethylene glycol:buffer)	T_m (°C) (buffer)
di18:0 PC (DSPC)	57.08 ± 0.07	55.16 ± 0.01
di20:0 PC (DAPC)	67.815 ± 0.002	NA
di14:0 PC (DMPC)	24.34 ± 0.01	NA
18:1-18:0 PC (SOPC)	4.119 ± 0.007	6.14 ± 0.02
18:1-16:0 PC (POPC)	-4.83 ± 0.08	NA
di18:1 PC (DOPC)	-10.93 ± 0.03	NA
di18:2 PC	-52.7 ± 1.6	NA
di16:1 PC	-33.05 ± 0.04	NA
di22:1 PC (DEPC)	15.85 ± 0.03	NA
[3][3]PC	15.18 ± 0.02	20.72 ± 0.02
[5][3]PC	11.77 ± 0.16	16.67 ± 0.34
[5][5]PC	68.4 ± 0.1	NA

Supplementary Table S1. Transition temperatures T_m for all lipid dispersions assessed using DSC. In the main text, error is reported using the precision of the instrument (±0.1 °C) where the standard deviation is lower than 0.1 °C.

*Ethylene glycol was used as an antifreeze co-solvent in order to measure transition temperatures below 0 °C. In order to compare all the T_ms measured under the same conditions and to be consistent, the 1:1 ethylene glycol/phosphate buffer was used to suspend all lipid films, including those with T_ms above 0°C. Ethylene glycol is known to cause small changes of a up to a few degrees in measured T_ms.[13,14] As the difference between **[5][3]PC**/**[3][3]PC** and **[5][5]PC** is over 50°C, and **[3][3]PC**/**[5][3]PC** are clearly fluid at room temperature from GUV fluorescence microscopy, small effects of ethylene glycol on the measured T_ms would not change our conclusions. As the analysis in Figs. 4D and 5D in the main text rely on comparisons of T_ms above and below 0°C, we felt it best to perform all DSC analyses in the same solution. We note that our measured T_ms for straight chain PCs are close to published values.[14] In order to confirm that the

ethylene glycol did not have an anomalous effect on the T_ms of ladderane lipids, we also measured T_ms for DSPC, SOPC, **[5][3]PC** and **[3][3]PC** in phosphate buffer (the same buffer used in hydrazine transmembrane diffusion assays). As shown in Supplementary Table S1, the T_ms in buffer are between 2 and 5.5 °C higher in buffer than in 1:1 ethylene glycol/buffer. These differences are small, should be consistent across lipids, and do not change our conclusions or data analysis. Both **[5][3]PC** and **[3][3]PC** are still fluid at room temperature in buffer. Additionally, lateral diffusion coefficients and transmembrane pH equilibration rates are still anomalously low for the ladderane PCs even at the slightly higher T_ms in buffer.

9. Spectral and Kinetic Characterization of HS

Fluorescence Spectra

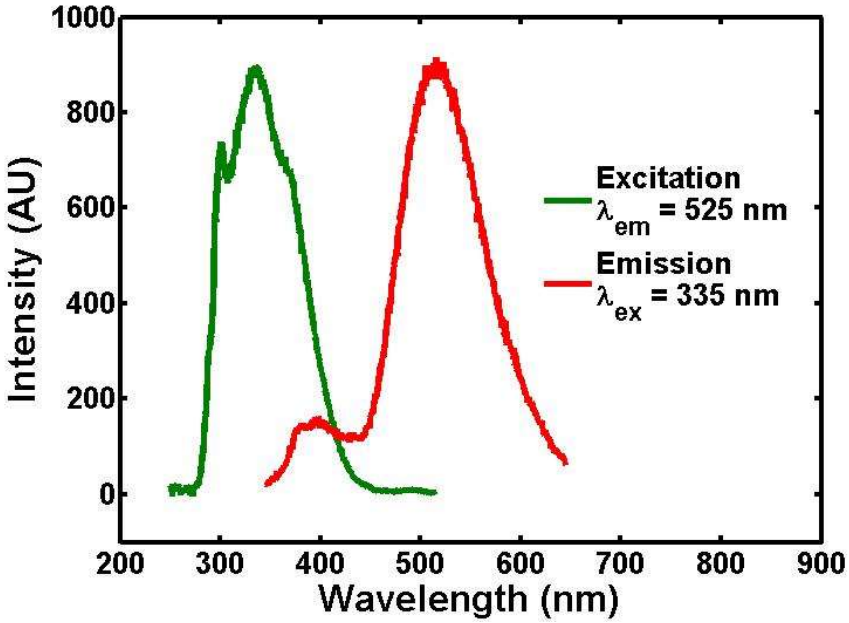

Supplementary Figure S4. Fluorescence and fluorescence excitation spectra of HS–HZ formed *in situ* by the reaction of HS (45 µM) with hydrazine (50 mM) in 500 mOsM buffer for 1 h, obtained in 4-mL cuvette (path length = 1 cm). Green: fluorescence excitation spectrum with λ_{em} = 525 nm. Red: emission spectrum with λ_{ex} = 335 nm.

NMR Characterization of **HS** and Hydrazine Reaction

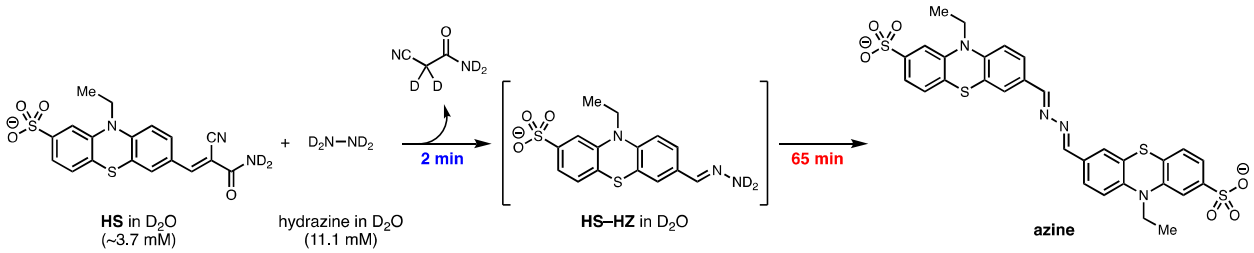

Supplementary Scheme S6. Observation by NMR of **HS–HZ** and **azine** formation.

Procedure

To a deep orange solution of **HS** (1.6 mg, ~0.037 mmol) and hydrazine monohydrochloride (0.8 mg, 0.111 mmol) in 1.0 ml D_2O in an NMR test tube under Ar was added 40% NaOD in D_2O (30 µl, 0.3 mmol). The test tube head space was filled with Ar and the tube was capped and sealed with Parafilm. The reaction was initiated by inverting the tube which was done four times. The mixture immediately began to pale. The tube was inserted into a 600 MHz NMR spectrometer (Varian) and successive 8-scan spectra were taken 40 seconds apart for 30 minutes. At *t* = 30 minutes, a 3-minute lapse in data collection commenced for the preparation of an LCMS sample. Data collection then resumed (40 seconds apart, as before) for an additional 30 minutes. Sample was yellow and fluoresced green under long-wave UV radiation.

Results

Immediately after raising the pH, all **HS** was converted (no **HS** signal observed at t = 2 min, Supplementary Fig. S5) to an intermediate that we identify as **HS–HZ** based on literature precedent and mass spectrometry (m/z obsd. = 348.1, calcd. = 348.0).[8] Over the course of the NMR experiment, **HS–HZ** was converted to **azine XX** (m/z obsd. = 665.3, calcd. = 665.1).

When **HS** (53 μM) was combined with excess hydrazine (125mM) in buffer (see Supplementary Fig. S11), gain of fluorescence was observed at a rapid rate ($t_{1/2}$ = 1.0 min). Since this fluorescence gain is over an order of magnitude faster than the expected rate of **azine** formation from **HS–HZ**, we deduce that the fluorescence gain observed in our fluorometric assays is due to the formation of **HS–HZ**. We hypothesize that at the lower concentration used in the hydrazine transmembrane diffusion assay ([**HS**]$_0$ = 420 μM; [**HS–HZ**](t) ≤ 420 μM), **HS–HZ** dimerizes on a slower timescale than that of the experiment.

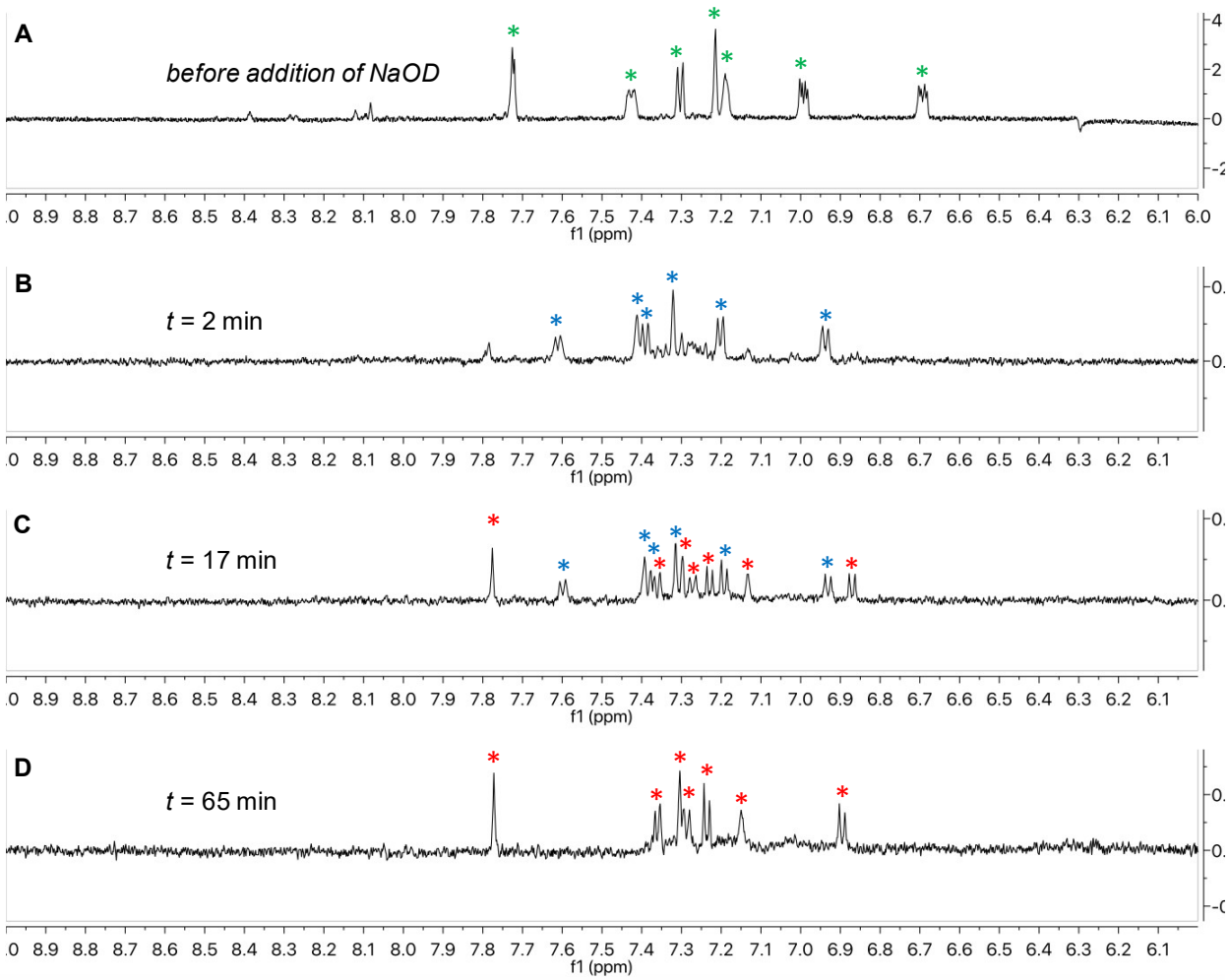

Supplementary Figure S5. ^{1}H NMR spectra (600 MHz, D_2O) of (A) **HS**, (B) **HS–HZ** (t = 2 min), (C) a mixture of **HS–HZ** and **azine** (t = 17 min), and **azine** (t = 65 min) acquired before and during the kinetic experiment.

Vesicle encapsulation and membrane interaction evaluation

Procedure

In order to evaluate whether **HS** can be encapsulated in vesicles and whether **HS** is localized in the aqueous interior of vesicles or membrane bound, we encapsulated **HS-HZ** in **[5][3]PC** GUVs. **HS-HZ** was used because **HS** has very little fluorescence. **HS-HZ** was generated by reacting 850 µM **HS** with 8.5 mM hydrazine in degassed water overnight. A Leica DMI6000 B epifluorescence microscope equipped with a 63X oil immersion objective (Leica Microsystems, Buffalo Grove, IL, USA), pco.edge sCMOS (PCO, Kelheim, Lower Bavaria, Germany) camera, DAPI filter cube (ex = 387/1 nm, bs = 344-404/415-570 nm, em = 447/60 nm), and Texas Red filter cube (ex = 560/40, bs = 595, em = 645/75) was used to image these vesicles. Images were false colored and merged to examine localization of the two dyes. Supplementary Fig. S6A-B show that **HS-HZ** fluorescence is clearly localized to the interior of the GUVs, proving that this molecule can be encapsulated and that it does not strongly interact with lipid bilayers.

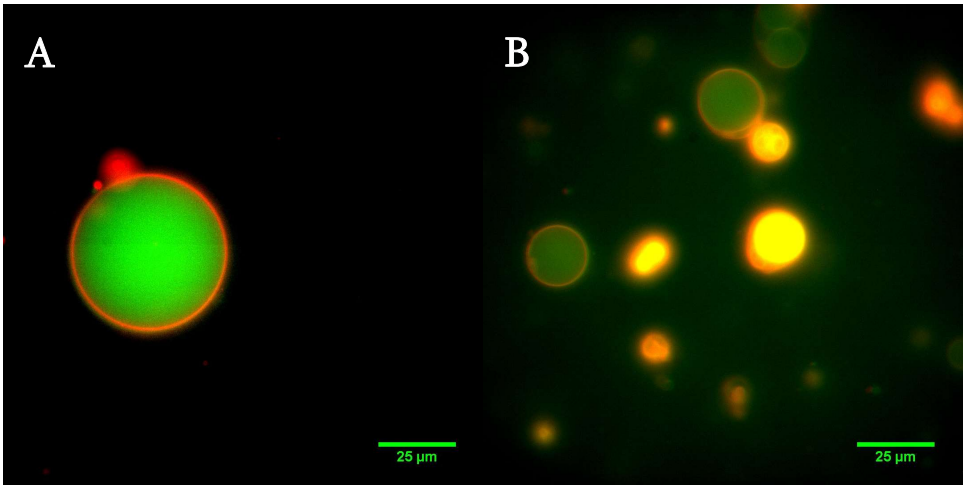

Supplementary Figure S6. Fluorescence images of **[5][3]PC** GUVs encapsulating **HS-HZ**. (A-B) Hydrated **[5][3]PC** (0.1 mol% **Texas Red-DHPE** (red) encapsulating 420 µM **HS-HZ** (green)) incubated at 37 °C then cooled to room temperature.

Kinetic Experiments

i. Lipid-free kinetic run

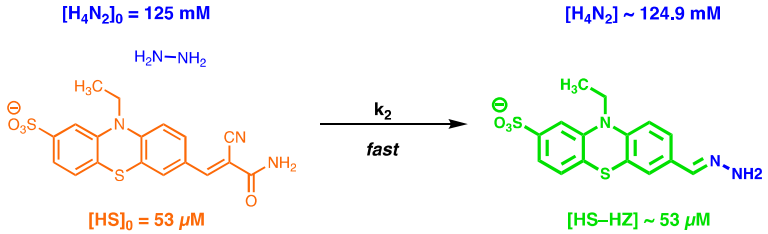

Supplementary Figure S7. Lipid-free kinetic run.

Procedure

Under argon, 250 µL of 420 µM **HS** was added to 750 µl degassed 50 mM phosphate buffer and mixed by pipette aspiration; this 1 mL solution (rather than 1 mL vesicles prepared from hydration of a lipid film with 250 µL of 420 µM **HS**) was added to 1 mL hydrazine buffer in

a cuvette under argon; the mixture was mixed by aspiration, and then a fluorometric kinetic trace was acquired at λ_{ex} = 335 nm and λ_{em} = 525. Rapid pseudo-first order kinetics were observed with $t_{1/2}$ ~ 1 min.

ii. Vesicles ruptured with Triton X-100

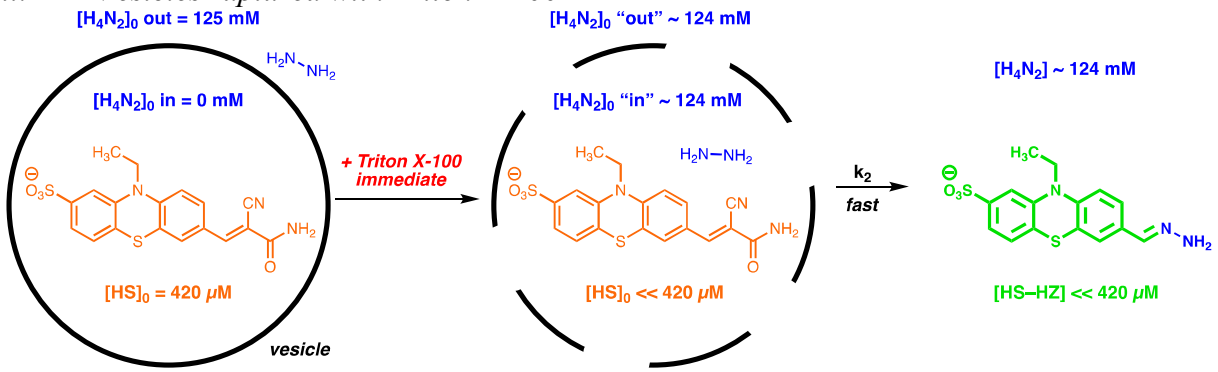

Supplementary Figure S8. Kinetic run with ruptured vesicles (Supplementary Figure S10, red trace).

Procedure

SOPC SUVs with encapsulated 420 μM HS in degassed 50 mM phosphate buffer were prepared and purified according to the procedure on SI p. 44. Under argon, the vesicles (1 mL) were added to 1 mL hydrazine buffer in a cuvette under argon; the mixture was mixed with pipette aspiration; 30 μL of 10% Triton X-100 in H_2O (v/v) was added to the mixture, which was mixed by aspiration under argon and then capped with Parafilm before acquiring a fluorometric kinetic trace at λ_{ex} = 335 nm and λ_{em} = 525.

iii. Hydrazine diffusion into vesicles

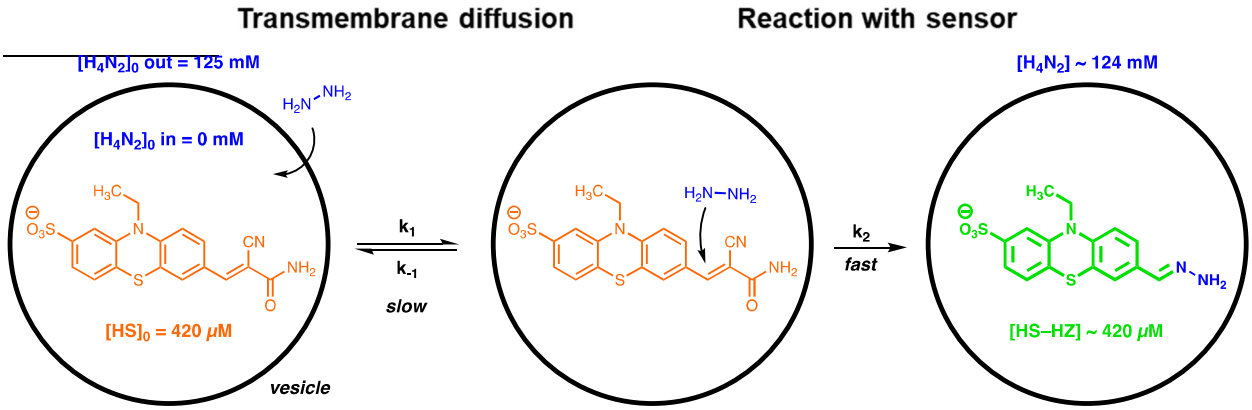

Supplementary Figure S9. Kinetic run with intact vesicles (Supplementary Fig. S11, blue trace). Hydrazine diffusion experiment was carried out according to the procedure in Section 10.

iv. HS–HZ leakage

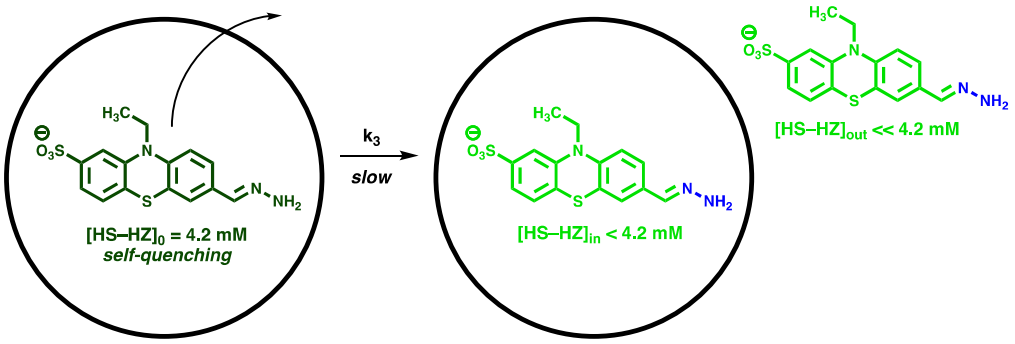

Supplementary Figure S10. Diffusion of **HS–HZ** out of vesicles (Supplementary Fig. S11, green trace). *Note*: at 4.2 mM, some dimerization is likely to occur on the time course of this experiment. We assume that lower hydrophilicity of the azine results in faster leakage than for **HS–HZ**, so that this experiment gives an upper bound on the **HS–HZ** leakage rate.

Procedure

Under argon, 422 µL hydrazine buffer was added to 0.72 mg of **HS** in a vial and then incubated at room temperature for 30 min under argon to make a 0.72 mg/401.5 mg $mmol^{-1}$/0.422 mL = 4.2 mM solution of **HS–HZ**. A 0.5-mg film of POPC under argon was hydrated with 250 µl of 4.2 mM **HS–HZ**, vortexed vigorously for ≥10 sec, and extruded 31 times through a 50 nm-pore polycarbonate membrane before purification on a size exclusion column run under argon with degassed 50 mM phosphate buffer. To assess maximum intensity (100% diffusion) for the sample, 0.5 mL vesicles were ruptured with 30 µl 10% Triton X-100 in H_2O (v/v) and added to 1.5 mL degassed 50 mM phosphate buffer; this sample was inserted into the fluorimeter and a kinetic trace at λ_{ex} = 335 nm and λ_{em} = 525 was obtained for 5 min. A new sample was then prepared by adding 0.5 mL vesicles to 1.5 mL degassed 50 mM phosphate buffer and collecting a kinetic trace for 12 h. After the run was over, 30 µL 10% Triton X-100 in H_2O (v/v) was added to the sample to rupture the vesicles to verify the maximum intensity (100% diffusion). This value agreed well with the value obtained before the leakage experiment (178 ± 1 vs. 172.2 ± 0.9 arbitrary units). The dequenching leakage $t_{1/2}$ was obtained by linear fit of the logarithm using the average maximum intensity value obtained between the two rupturing experiments (175 arbitrary units).

Results

The reaction of the hydrazine sensor (**HS**) with excess N_2H_4 at 125 mM had a much shorter $t_{1/2}$ (1.0 min; 5.3 min in the presence of lipid and detergent) than that of **HS** encapsulated within SUVs composed of 18:0-18:1 PC (SOPC) ($t_{1/2}$ = 50.7 min). Leakage from SUVs of the hydrazal dye product **HS–HZ** is negligible on the timescale of hydrazine transmembrane diffusion, suggesting that **HS** leakage is also negligible on this timescale (Supplementary Fig. S11).

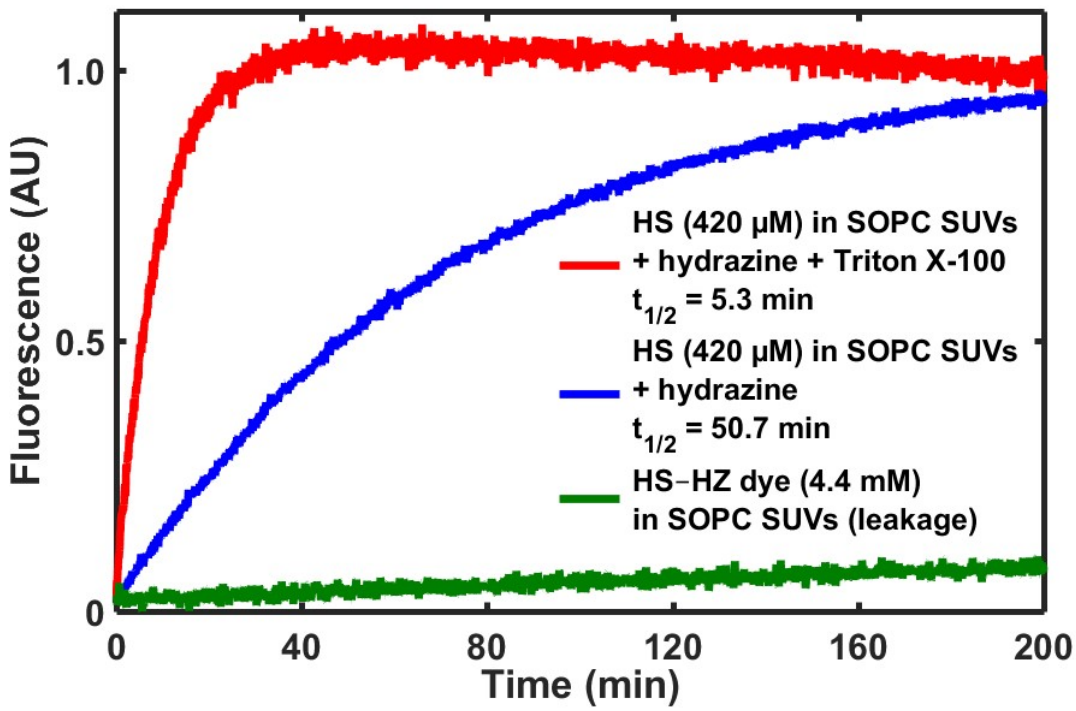

Supplementary Figure S11. Characterization of **HS** performance. Since the concentration of dye is higher in this assay than in the hydrazine diffusion assay, this provides an upper bound for the dye leakage rate during the hydrazine diffusion assay. Sensor leakage is assumed to be similar. When 18:0-18:1 PC (SOPC) SUVs encapsulating **HS** were added to 125 mM N_2H_4 and ruptured, a much faster fluorescence increase ($t_{1/2}$ = 5.3 min) was observed than when intact SOPC SUVs encapsulating **HS** were incubated in 125 mM N_2H_4. **HS–HZ** dye leakage out of 18:0-18:1 PC (SOPC) SUVs, measured by a dequenching assay, is negligible over the course of N_2H_4 transmembrane diffusion.

10. Hydrazine Transmembrane Diffusion Assay

Procedure
Buffers and solutions were prepared according to procedures in Supplementary Information Section 6.

A. Lipid film preparation: 1.0 mg of phosphatidylcholine lipid in chloroform solution was dispensed into a 20 mL scintillation vial, dried under a stream of argon, and put under house vacuum in a desiccator overnight. The vial was then removed from the desiccator, purged of air with a stream of argon, closed, and sealed with Parafilm.

B. Size exclusion column preparation: A suspension of Sepharose® CL-4B in 10–30% ethanol (Sigma) was added to an 8.5-cm size-exclusion column. Methanol was washed out of the column by flushing with at least 5 column volumes of 50 mM phosphate buffer. Then the column was capped with a rubber septum, the septum was pierced with an argon-filled balloon with attached needle, and the column was eluted until the meniscus descended to the top of the resin. Then, under a stream of argon, the head space was filled with degassed buffer and the Falcon tube containing the degassed buffer was purged of any incidental air with a stream of argon, then closed. Using this technique, the column was purged of oxygenated buffer by running at least 5 column volumes of degassed buffer through the column under argon.

C. Film hydration and extrusion to form 90–130-nm SUV's: 250 µL degassed phosphate buffer was passed through an Avanti Mini Extruder (Avanti Polar Lipids, Alabaster, AL) with a 50 nm-pore polycarbonate membrane 9 times to remove bubbles and check for leaks. 250 µL of 440 µM hydrazine sensor (**HS**) was added to the dried lipid film under a stream of Ar, and the mixture was vortexed for ≥10 seconds at full power. In the case of ladderanes, which were resistant to suspension, the sample was additionally agitated in an ultrasonic bath for ≥5 seconds. The cloudy yellow suspension was passed through the extruder 31 times.

D. Vesicle purification by size exclusion chromatography: The vesicles were loaded onto the column under a stream of Ar and then degassed phosphate buffer was added to the column under a stream of Ar; the column was subsequently run under Ar. Effluent was collected in a 4 mL polyacrylamide cuvette that was under a continuous stream of Ar. Vesicles were not visible by eye or upon exposure to a UV lamp; vesicles were detected by directing the beam from a 5 mW green laser pointer horizontally through the cuvette; upon elution of the vesicles, bright scattering was visible (Supplementary Fig. S12). Collected vesicle sample was capped with Parafilm.

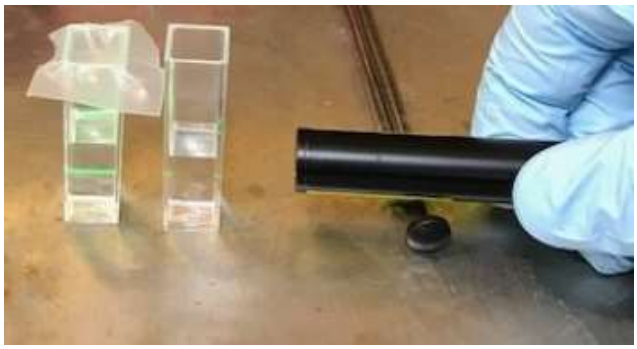

Supplementary Figure S12. Contrast in laser scattering between phosphate buffer (right) and sample containing eluted vesicles (left).

E. Fluorometric kinetic hydrazine diffusion measurement: Under Ar stream, 1.0 mL of hydrazine buffer was dispensed into a 4mL polyacrylamide cuvette pre-filled with Ar and capped with Parafilm. Under an Ar stream, vesicles were mixed by aspirating with a 1 mL micropipette 3x, then 1.0 mL vesicles were added to the 1.0 mL of hydrazine buffer. After mixing the contents by aspirating with the 1 mL micropipette 3x under Ar stream, the cuvette was carefully sealed with Parafilm and inserted into a fluorimeter with excitation wavelength 335 nm, excitation wavelength 525 nm, slit widths 5 nm, data interval 0.04 min, experiment length 300 min. The first 5 min of acquisition were discarded to allow for equilibration of the sample.

F. Data analysis: Data were fit to the equation $y = a - b * \exp(c * x)$ using the cftool module in Matlab. The constant c represents the rate constant k_{obs}; the half-life $t_{1/2}$ was calculated using the equation $t_{1/2} = \ln(2)/k_{obs}$.

Effect of pH on hydrazine transmembrane diffusion

Given that the pH of the interior of the anammoxosome is thought to be approximately 6.3, we repeated the hydrazine transmembrane diffusion assay at pH = 6.3.[15] The results are summarized in Supplementary Table S2. At pH = 6.3, transmembrane diffusion rates are slowed. Lowering the pH decreases the fraction of neutral hydrazine molecules, which likely diffuse across the bilayer faster than protonated hydrazine. While absolute transmembrane diffusion rates change with pH, the trend does not: at both pH levels, ladderane PC bilayers have transmembrane diffusion half-lives that are similar to those of conventional straight chain PCs.

Lipid	N_2H_4 Diff. $t_{1/2}$ (min) pH = 7.40	N_2H_4 Diff. $t_{1/2}$ (min) pH = 6.30
18:0-18:1 PC (SOPC)	50.5 ± 0.5	96 ± 23
di22:1 PC (DEPC)	98.9 ± 6.0	583 ± 25
[3][3]PC	71.5 ± 2.0	265 ± 5

Supplementary Table S2. Comparison of hydrazine transmembrane diffusion rates at pH = 7.40 and 6.30. Transmembrane diffusion rates are slower at pH = 6.30, but the trend remains the same. **[3][3]PC**'s hydrazine transmembrane diffusion $t_{1/2}$ falls between those of SOPC and DEPC at both pHs.

11. Dynamic Light Scattering (DLS)

The size of SUVs for hydrazine diffusion measurements was characterized by DLS. 1 mL of the SUV solution collected from the size exclusion column was mixed with 1 mL 500 mOsM phosphate buffer (pH = 7.40 ± 0.02) and the mixture was analyzed with a NanoBrook Omni (Brookhaven Instruments Corp., Holtsville, NY) <5 hours after vesicles were obtained from the size exclusion column. The DLS particle size measurement was obtained with the sample cell at 20 °C at an angle of 90 ° for 90 s.

Results

Lipid	Eff. Diam. (nm)	Polydispersity
di16:1 PC	94.90 ± 1.77	0.105 ± 0.024
di18:1 PC (DOPC)	96.80 ± 1.23	0.090 ± 0.012
di22:1 PC (DEPC)	98.65 ± 1.99	0.112 ± 0.011
18:0-18:1 PC (SOPC)	91.87 ± 0.74	0.074 ± 0.026
di18:2 PC	91.51 ± 0.52	0.126 ± 0.017
[3][3]PC	122.33 ± 0.73	0.124 ± 0.016
[5][3]PC	120.47 ± 5.19	0.136 ± 0.040
[3][3]PC (2x 100 nm + 2x 50 nm)	98.12 ± 2.72	0.129 ± 0.003

Supplementary Table S3. Summary Statistics from DLS data acquired with SUVs hydrated with 440 μM HS in phosphate buffer, vortexed, extruded 31 times through a 50 nm-pore polycarbonate membrane, and purified with a size exclusion column. Each DLS data set was acquired in triplicate. In the bottom entry, the suspension was extruded 31 times through two stacked 100 nm-pore membranes, followed by extrusion through two stacked 50 nm-pore membranes.

12. Small-Angle X-Ray Scattering (SAXS)

A. Sample preparation:

1 mg of PC lipid dried into a thin film was hydrated with 250 µL water, vortexed, and then extruded through two stacked 100 nm-pore membranes 31 times. The resulting suspension was then extruded through two stacked 50 nm-pore membranes 31 times for straight-chain PCs and 51 times for **[5][3]PC** and **[3][3]PC** to ensure unilamellarity.[16] The resulting suspension was aliquoted into small centrifuge tubes at volumes of 30 µL each.

B. SAXS data collection:

Synchrotron SAXS data were collected at beamLine 4-2 of the Stanford Synchrotron Radiation Lightsource (SSRL), Menlo Park, CA.[17] The sample to detector distance was set to 1.1 m with and X-rays wavelength of λ = 1.127 Å (11 keV). Using a Pilatus3 X 1M detector (Dectris Ltd, Switzerland) the setup covered a range of momentum transfer $q \approx 0.017 - 1.17$ Å^{-1} where q is the magnitude of the scattering vector defined as $q = 4\pi \sin\theta / \lambda$, with θ the scattering angle and λ the wavelength of the X-rays. Aliquots of 30 µl of freshly extruded vesicles were loaded onto the automated sample loader at the beam line.[18] Consecutive series of sixteen 2 s exposures were collected first from the buffer blank followed by the vesicle samples. Solutions were oscillated in a stationary quartz capillary cell during data collection to maximize the exposed volume in order to reduce the radiation dose per exposed sample volume. The collected data was radially integrated, analyzed for radiation damage and buffer subtracted using the automated data reduction pipeline at the beam line. To improve statistics and check for repeatability the measurements were repeated with different aliquots 8 to 10 times per sample. As no significant differences were found between the repeat measurements, the different data sets for each sample were averaged.

C. SAXS data analysis:

The buffer-subtracted and averaged data were fit using the model for unilamellar vesicles,[19] which is based on approximating the electron density of the bilayer by three Gaussian peaks corresponding to the inner and outer phosphate peak and a negative trough at the center. The following Equation 1 was used for the fits:

$$I(q) = I_0 q^{-2} \sum_{i,j}^{n=3} (R_0 + \varepsilon_i)(R_0 + \varepsilon_j)\rho_i\rho_j\sigma_i\sigma_j \exp[-q^2(\sigma_i^2 + \sigma_j^2)/2] \cos[q(\epsilon_i - \epsilon_j)] + a_0 + a_1 q \quad (1)$$

where R_0 is the mean radius of the vesicle measured at the center of the bilayer, ε is the peak displacements from the bilayer center, σ the Gaussian width of the peak and ρ its amplitude. I_0 is the overall intensity of the measured profile. A background term was added, consisting of a constant a_0 and a linear term a_1, to take into account the contribution from possible lateral correlations. The measured data were fit in the q-region between $q = 0.02 - 0.6$ Å^{-1} (depicted as colored regions in Supplementary Fig. S12). First the data were fit using a simulated annealing routine and the results were then further optimized using a non-linear least square algorithm, both by using code from the open source GNU scientific library project (https://www.gnu.org/software/gsl/). The fit parameters including the final χ^2 value of the fits and the resulting bilayer thickness (measured as distance between the inner and outer leaflet peak in the electron density) are summarized in Supplementary Table S4.

D. SAXS data discussion:

When comparing the measured data of the straight chain lipids with the ones from the ladderanes, the most striking difference is the behavior of the signal at low q. While the straight chains lipids all have a rather large pronounced first lobe centered around q ~ 0.12 $Å^{-1}$ (when compared to the higher order lobes) the first lobe of the ladderane lipids is much smaller and shifted to slightly higher q. The resulting fits using the above model convincingly described the measured data for all the lipids as can be seen in Supplementary Fig. S13. The resulting electron density profiles are depicted in Supplementary Fig. S14. Within the model used the smaller first lobe of the SAXS data for the ladderane lipids can only be accounted for by reducing (and almost eliminating) the central dip in the electron density resulting in a flat central region of the ladderane bilayer electron density. This is likely caused by the increased electron density of the ladderane chains and a possible slight interdigitation of the leaflets at the bilayer center. The thickness of the ladderanes (that is the distance between the peaks) is in both cases ~40 Å and is close to the thickness measured for the di20:1 PC straight chain lipid.

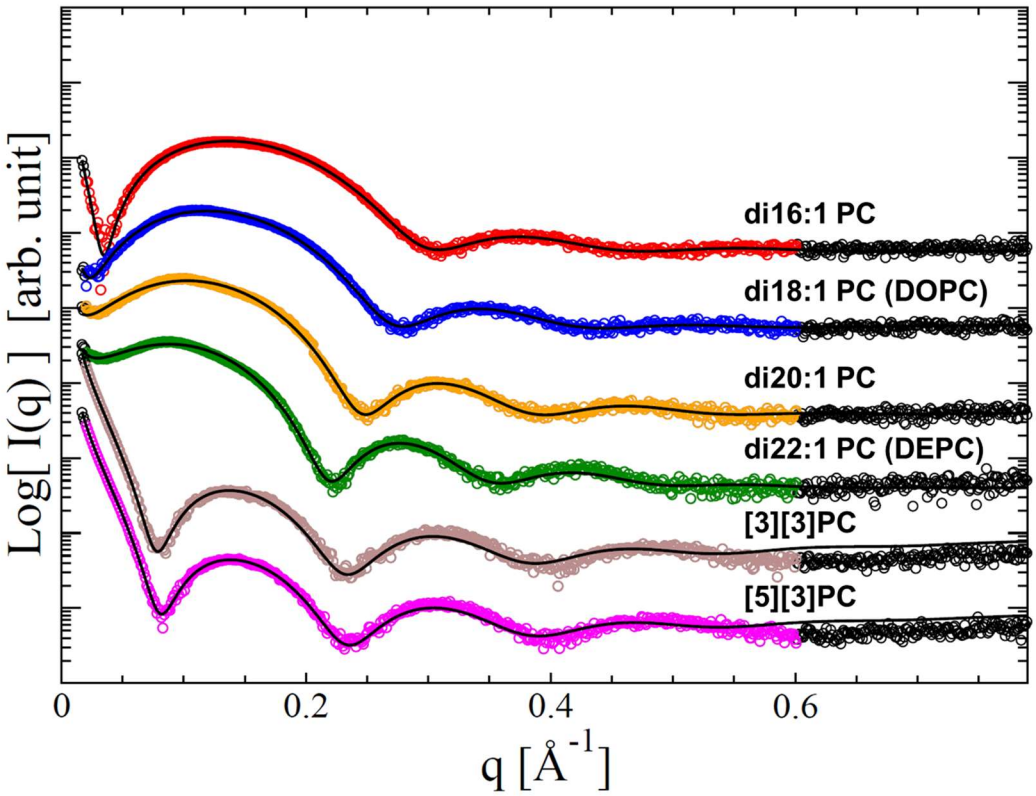

Supplementary Figure S13. The small angle scattering intensities for the unilamellar vesicles of the straight chain lipids and the ladderanes. The black lines are the fits to the model. The colored regions are the part of the data used for the fitting routines.

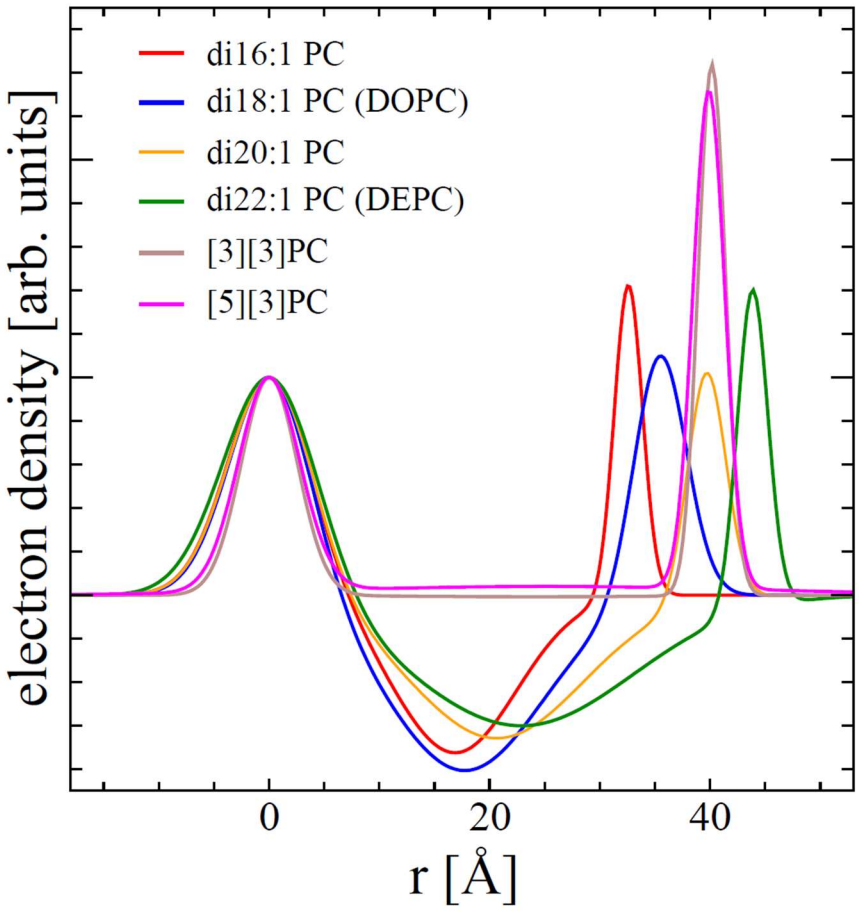

Supplementary Figure S14. The electron density profiles resulting from the fits to the unilamellar vesicle model. The profiles are scaled in height and horizontally shifted to overlay on the inner (left) peak of the electron density. The thickness of the bilayers as defined by the peak to peak distance can thus be read off directly from the position of the outer (right) peak.

Lipid	ρ_1	ε_1	σ_1	ρ_2	σ_2	ρ_3	ε_3
di16:1 PC	1.39 ± 0.04	-16.8 ± 0.04	3.75 ± 0.02	-1.00 ± 0.01	5.58 ± 0.01	1.98 ± 0.03	15.7 ± 0.01
di18:1 PC	1.28 ± 0.05	-17.6 ± 0.06	3.71 ± 0.01	-1.00 ± 0.01	7.04 ± 0.01	1.41 ± 0.03	17.7 ± 0.01
di20:1 PC	1.56 ± 0.05	-20.5 ± 0.05	3.80 ± 0.01	-1.00 ± 0.01	7.86 ± 0.01	1.60 ± 0.07	19.1 ± 0.01
di22:1 PC	1.74 ± 0.04	-22.7 ± 0.04	4.29 ± 0.02	-1.00 ± 0.01	10. ± 0.03	2.4 ± 0.06	21.0 ± 0.01
[3][3]PC	3.59 ± 0.07	-22.3 ± 0.07	2.66 ± 0.02	-0.04 ± 0.30	1.5 ± 0.60	6.52 ± 0.07	17.7 ± 0.02
[5][3]PC	0.54 ± 0.08	-25.1 ± 0.08	2.78 ± 0.02	0.02 ± 0.37	19.2 ± 0.4	1.25 ± 0.06	14.7 ± 0.01

Lipid	σ_3	I_0 [x10^{-7}]	R_0	a_0	a_1	χ^2	$D = \varepsilon_3 - \varepsilon_1$
di16:1 PC	1.27 ± 0.01	1.57 ± 0.01	39.5 ± 0.8	0.33 ± 0.01	0.26 ± 0.01	0.906	32.5 ±0.04
di18:1 PC	2.37 ± 0.01	7.09 ± 0.02	50.3 ± 0.5	0.33 ± 0.01	0.33 ± 0.01	1.205	35.3 ± 0.06
di20:1 PC	1.74 ± 0.01	6.13 ± 0.01	51.2 ± 0.5	0.22 ± 0.01	0.21 ± 0.02	1.720	39.6 ± 0.05
di22:1 PC	1.38 ± 0.01	5.23 ± 0.01	50.2 ± 0.3	0.20 ± 0.04	0.21 ± 0.02	2.199	43.7 ± 0.04
[3][3]PC	0.83 ± 0.03	1.08 ± 0.01	48.6 ± 0.5	0.07 ± 0.01	0.67 ± 0.01	1.170	40.0 ± 0.07
[5][3]PC	1.42 ± 0.04	1.69 ± 0.01	172 ± 2	0.04 ± 0.01	0.99 ± 0.01	1.247	39.8 ± 0.08

Supplementary Table S4. Fit results for the different lipids and the resulting thickness. The bilayer center, ε_2, was kept at 0 for all fits.

E. Investigation of multilamellarity of vesicles:

We also used the SAXS data to estimate the unilamellarity of the SUVs as SAXS is a highly sensitive method for detecting multilamellarity in vesicles.[19,20] The model used in the analysis of the SAXS data of the SUV preparations does not take into account the potential presence of multilamellar vesicles (MLVs) in the sample.[19] The preparation method for the SUVs used in this study has, however, previously been shown to produce vesicles that are predominantly unilamellar. In order to confirm that the vast majority of vesicles were unilamellar and that the model used was appropriate for the sample, we performed a more careful analysis of potential scattering contribution from multilamellar vesicles. We show that multilamellarity can be limited to levels below 5% for any number of lamellae above one and to below 2% for MLVs with 5 lamellae or more.

We can extend the model used in Equation 1 to include additional layers of lipid bilayers by increasing the number of Gaussians, *n*, in the equation. In order to calculate the scattering curves for MLVs, we describe the electron density of each bilayer in a multibilayer stack with a set of three Gaussians, increasing n in Equation 1. The displacement ε of the Gaussians with respect to the vesicle radius R_0 were chosen assuming a constant bilayer thickness and a 25 Å water layer between each bilayer (see Supplementary Fig. S15).

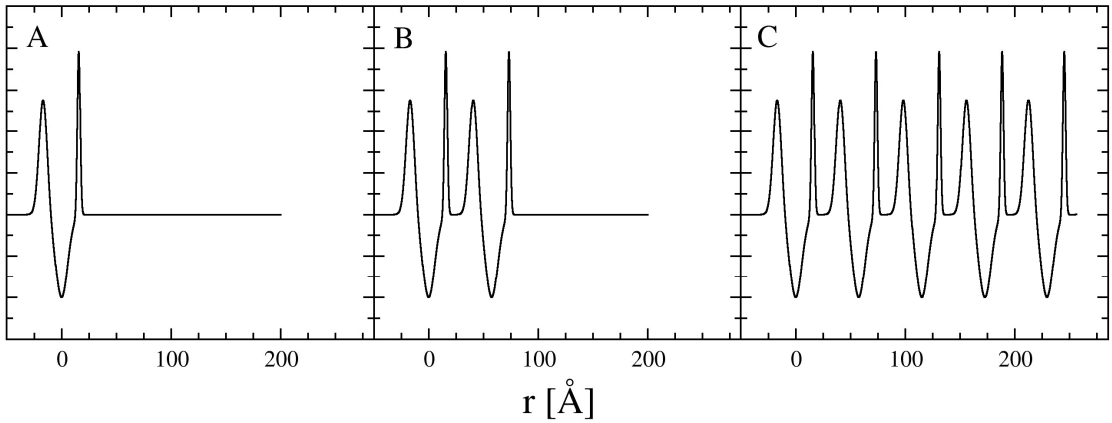

Supplementary Figure S15: Electron density for unilamellar (A), two-lamellae (B) and five-lamellae (C) vesicles using the parameters of the unilamellar fit to the di16:1 PC data including a water layer separation between neighboring bilayers of 25 Å.

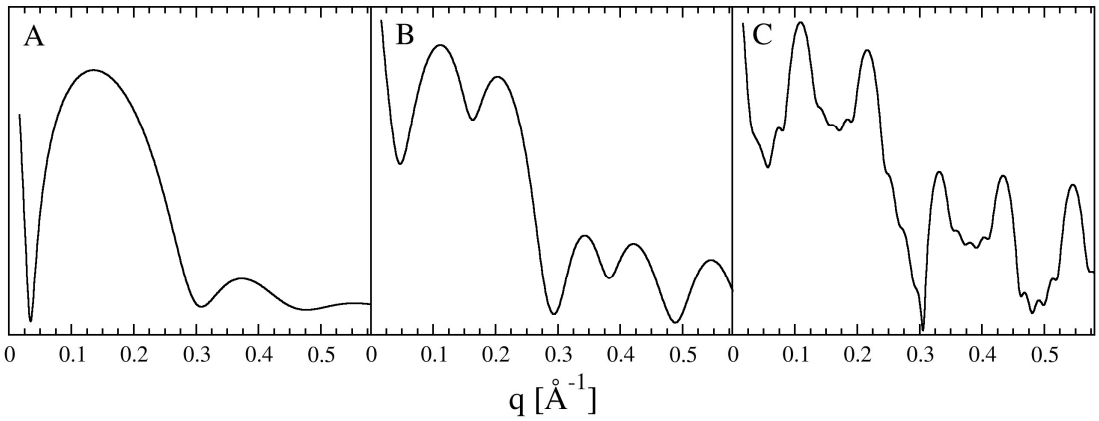

Supplementary Figure S16: Calculated solution scattering intensities for unilamellar (A), two-lamellae (B) and five-lamellae (C) vesicles corresponding to the electron densities displayed in Supplementary Fig. S15 for di16:1 PC.

We then calculated the scattering curves for vesicles with 1, 2, and 5 lamellae, shown in Supplementary Fig. S16. The calculated scattering profiles of the stacked membranes clearly show the effect of the interference between the bilayers appearing as higher frequency maxima on the rather broad intensity curve originating from the single bilayer electron density. These interference maxima are stronger and more pronounced the higher the multilamellarity. In order to assess the potential contribution of multilamellar vesicles to the measured scattering data we first used the above calculated scattering intensities for vesicles with different numbers of lamellae to calculate predicted intensities for samples of unilamellar vesicles with 2 %, 5 % and 10 % of contamination from either two-lamellae vesicles or five-lamellae vesicles. Supplementary Figs. S17 and S18 show a comparison of the pure unilamellar case with addition of double and five lamellae vesicles at the three different levels of contamination. The comparison shows that the scattering profiles for the contaminated samples are mostly identical to that of the pure unilamellar case except for small regions where the interference between the bilayers cause significant deviation of the scattering intensities from the unilamellar case. The largest deviations from the unilamellar case can be found within the approximate q-range between 0.1 and 0.25 $Å^{-1}$. The figure also shows that the deviation from the unilamellar case are getting stronger (as the same level of contamination) the higher the multilamellarity of the vesicles.

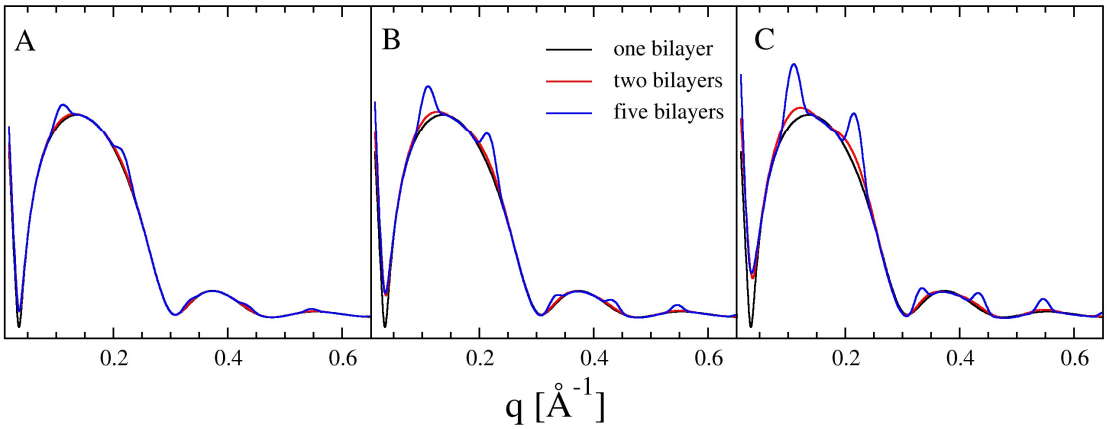

Supplementary Figure S17: Comparison of calculated scattering intensities of di16:1 PC SUV samples (black line) with the scattering intensities of samples that have small amount of MLV contamination (red line: 2 lamellae, blue line: 5 lamellae). (A) 2% contamination, (B) 5% contamination and (C) 10% contamination.

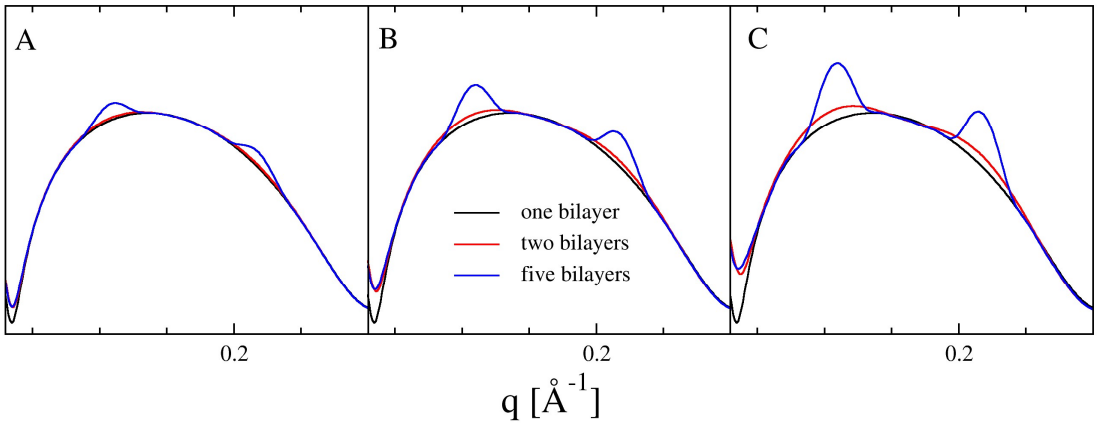

Supplementary Figure S18: Detailed view of the scattering in the q-range between 0.1 and 0.25 $Å^{-1}$ from Supplementary Fig. S17 to more clearly show the deviation from the pure unilamellar scattering. (black line: unilamellar, red line: 2 lamellae, blue line: 5 lamellae). (A) 2% contamination, (B) 5% contamination and (C) 10% contamination.

In order to estimate the changes in the scattering profile caused by the multilamellar contributions and to assess the possible contamination with multilamellar vesicles in the original data, we calculated the mean square deviation, χ^2, of the calculated scattering curve from the experimental scattering curves at the three levels of contamination (2%, 5% and 10%) with either the 2-lamellae vesicles or the 5-lamellae vesicles. As the deviations are largest in the q-range between 0.1 and 0.25 $Å^{-1}$, we limited the calculation to that range.

Lipid	Contamination with 2-lamellae vesicles			Contamination with 5-lamellae vesicles		
	2%	5%	10%	2%	5%	10%
di16:1 PC	1.13	6.40	28.32	31.20	213.37	881.58
[5][3]PC	1.05	1.65	9.12	1.25	6.67	7.41
[3][3]PC	0.92	1.53	1.57	2.59	14.72	62.13

Supplementary Table S5: Relative mean square deviations, χ^2, between the calculated scattering curves with different levels of 2- and 5-lamellae MLVs and the pure unilamellar fit to the experimental data (from Supplementary Table S4) within the q-range between 0.1 and 0.25 $Å^{-1}$.

We calculated the relative χ^2 values by computing the ratio of the χ^2 value for the calculated scattering curves fit to the experimental data to χ^2 value for the unilamellar fit to the experimental data. Any relative $\chi 2$ value less than 1 indicates that the χ^2 value is smaller for the fit with the indicated multilamellar contribution than the purely unilamellar fit with Equation 1. In other words, the calculated scattering curve with multilamellarity is a better fit to the experimental than the purely unilamellar curve. Similarly, any relative χ^2 value greater than 1 indicates that χ^2 is larger for the multilamellar fit than for the unilamellar fit, and the

multilamellar fit is worse than the unilamellar fit. The relative χ^2 values listed in Supplementary Table S5 show that even small levels of contributions from 5-lamellae vesicles significantly increase the relative χ^2 values when comparing the experimental data to the calculated scattering curves. As the relative χ^2 values We can rule out any contribution of vesicles with 5 bilayers and more beyond the 2% level as the relative χ^2 values become large. For the 2-lamellae case, the changes in scattering intensity due to MLV contamination are more gradual and smaller as the percentage of contamination increases. As the relative χ^2 values are larger than 1 at 5% 2-lamellae contamination and higher, we can rule out any contamination higher than 5%. As we used the same extrusion methods to create SUVs for proton and hydrazine transmembrane diffusion assays, this provides further evidence that those SUVs were indeed highly unilamellar (> 95%).

13. pH Equilibration Assay

Procedure

Rates of pH equilibration across membranes of SUVs were measured according to the method of Koyanagi, *et al*.[21] Commercial POPC was also subjected to the same purification protocol to conform that the purification itself did not introduce contaminates that alter pH equilibration rates. Rates of pH equilibration were found to be highly sensitive to lipid purity. A lipid film was formed from 0.5 or 1 mg of each phospholipid by evaporating a chloroform solution under a gentle stream of argon while rotating the vial containing the lipid solution. Residual solvent was removed by placing lipid films under vacuum for at least four hours. 250 μL of 4 mM carboxyfluorescein (CF) in Buffer A was added to the vial with the lipid film. 4 mM was chosen as the CF concentration in order to maximize fluorescence signal as it produces the maximum fluorescence before self-quenching decreases fluorescence intensity. The vial was vortexed and sonicated until the lipid film was completely resuspended, and the solution appeared cloudy. The vesicle solution was then extruded through a membrane with 50 nm pores 31 times to produce uniform SUVs encapsulating 4 mM CF. Extravesicular dye was removed by size exclusion chromatography with Sepharose® CL-4B resin. The column was equilibrated with Buffer A, and Buffer A was used to elute SUVs. SUVs with CF encapsulated were collected as the first fluorescent band to elute from the column. SUVs were then used immediately for pH equilibration assays. Fluorescence time courses were recorded with a Perkin Elmer LS 55 fluorescence spectrometer. The excitation was set to 485 nm, emission to 517 nm, and the excitation and emission slits to 5 nm. The fluorescence intensity was recorded every second, and it was confirmed that this level of light exposure did not lead to any measurable photobleaching over the course of the experiment. The volume of SUV solution needed to begin the assay with a fluorescence signal that is high but does not saturate the detector was determined empirically. Portions of a few μL of SUV solution were added to 4 mL of Buffer B in a PMA cuvette until the fluorescence intensity reached near the maximum signal. Then, that volume of SUV solution was added to 4 mL of Buffer B in a PMA cuvette, the contents of the cuvette were mixed gently, and the fluorescence intensity was recorded until the fluorescence signal stopped decreasing. It was confirmed that the pH had fully equilibrated by adding Triton X-100 to break up the vesicles or by adding nigericin to break down the pH gradient. pH equilibration curves were fit to single exponential decays.

Purification of Ladderane PCs

During optimization of the assay, we noted that batches of **[5][3]PC** and **[3][3]PC** purified only by flash column chromatography on silica gel exhibited inconsistent (but generally faster) pH equilibration rates. A reverse-phase high-performance liquid chromatography purification step was added (see chemical synthesis procedure, Supplementary Section 4), which ensured consistency in pH equilibration rates between different batches of ladderane PCs. **[5][3]PC** and **[3][3]PC** used in all other experiments were also purified by HPLC, but little difference was observed relative to material purified only by silica gel chromatography. Presumably the pH equilibration assay is sensitive to minor impurities which have little effect in other experiments.

Effects of Membrane Potential on Rates of Transmembrane pH Equilibration

Diffusion of protons/hydroxide across lipid bilayers is much faster than the diffusion of other ions across bilayers. As a result, a membrane potential builds up across a lipid bilayer as protons/hydroxide ions diffuse across the bilayer to equilibrate a pH gradient. The buildup of this membrane potential opposes the transmembrane diffusion of protons and can cause the measured

rate of pH equilibration to be lower than it would be without a membrane potential. In order to prevent the buildup of membrane potential during the course of a pH equilibration experiment, the ionophore valinomycin and a potassium-containing buffer were used.[22] At low concentrations, valinomycin is selective for transporting potassium across lipid bilayers versus protons or other ions. In order to confirm that the slow proton/hydroxide transmembrane diffusion we observed for vesicles of ladderane PCs was not due to the buildup of membrane potential, we repeated the pH equilibration experiment with vesicles of **[5]|[3]PC** and 10 nM valinomycin. We added 50 mM K_2SO_4 to both Buffer A and Buffer B so that potassium would diffuse across the vesicle bilayer via valinomycin to prevent the buildup of membrane potential as the pH gradient equilibrates. We observed that the valinomycin actually somewhat decreased the rate of pH equilibration ($t_{1/2}$ = 76 ± 2 min). This relatively small change in pH equilibration rate may be due to the addition of K_2SO_4 to the buffer, effects of membrane potential on the structure of the bilayers, or effects of valinomycin on the structure of bilayers. Regardless, these experiments show that the extremely slow transmembrane diffusion of protons/hydroxide ions in ladderane PC bilayers vs straight-chain PC bilayers is not due to a buildup of membrane potential during the experiment. We also note that we are only comparing relative proton permeabilities, so our conclusions would not be affected by factors that affect the absolute proton permeabilities.

Confirmation of Valinomycin Insertion into Ladderane Bilayers and its Functionality

Given the highly dense lipid packing in ladderane bilayers, we thought it possible that valinomycin would not insert into them or not transport K^+. We performed a K+ transmembrane diffusion assay to assess whether valinomycin can incorporate into ladderane vesicles and transport K^+. The potassium-sensitive dye PBFI was encapsulated in SUVs and its fluorescence was used to assess whether K^+ had been transported across the bilayers by valinomycin. 455 μM PBFI was encapsulated in **[5]|[3]P**C and POPC SUVs using the same procedure used to encapsulate other water-soluble dyes (see Sections 10 and 13). Briefly, 455 μM PBFI in 200 mM Hepes (pH = 7.3) was used to resuspend films of 0.8 mg of lipid. Then, SUVs were separated from extravesicular dye with a size exclusion column. 200 μL of the SUVs were then added to 3 mL osmotically-balanced 50 mM KCl, 100 mM Hepes (pH = 7.3) buffer in a fluorescence cuvette. The fluorescence was monitored for 1 min., and then 4 μL of a 1 mM solution of valinomycin in DMSO was added to yield a final concentration of 10 nM. The contents of the cuvette were gently mixed, and the fluorescence was monitored for approximately 6 min. As a control 4 μL of DMSO without valinomycin was also added to POPC SUVs in order to test whether DMSO can induce K^+ leakage. In order to lyse the vesicles and obtain the maximum PBFI signal, 10 μL of 10% Triton X-100 was added to the cuvette. The percentage of K+ equilibration after valinomycin treatment was calculated as the percentage of maximum fluorescence signal reached before Triton X-100 addition (see Supplementary Fig. S19A-B).

No change in PBFI fluorescence was observed for 1 min. after addition of SUVs into buffer containing potassium. Like most other small ions, K^+ diffuses very slowly across bilayers without a pore or channel. Upon addition of valinomycin, PBFI fluorescence increases rapidly for both **[5]|[3]PC** and POPC SUVs. This indicates that valinomycin can indeed incorporate into ladderane bilayers and is able to transport K^+ in these bilayers. Upon Triton X-100 addition, the PBFI fluorescence either remains the same or increases a small amount, consistent with full equilibration of K^+ across the bilayers and unilamellar structure for both POPC and **[5]|[3]PC**. These results demonstrate that, despite the dense packing and high viscosity of ladderane bilayers, valinomycin is still active and can be used to dissipate membrane potential in the proton transmembrane

diffusion assay.

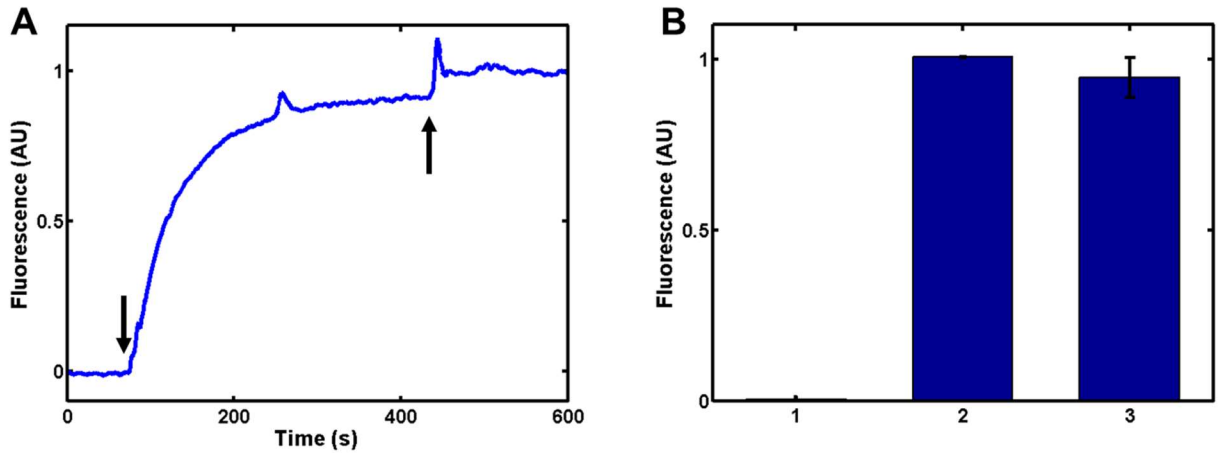

Supplementary Figure S19. Valinomycin activity in POPC and **[5][3]PC** SUVs. (A) Example of fluorescence data for PBFI in **[5][3]PC** SUVs. The first arrow marks the time of valinomycin addition, and the second arrow marks the time of Triton X-100 addition. The initial fluorescence of PBFI is set to 0 and the fluorescence after Triton X-100 addition is normalized to 1. (B) PBFI fluorescence after valinomycin addition and equilibration, normalized to fluorescence intensity after Triton X-100 addition. Entry 1 is the DMSO control, Entry 2 is POPC SUVs, and Entry 3 is **[5][3]PC** SUVS. Valinomycin causes rapid, full K^+ equilibration across bilayers composed of both lipids.

Confirmation of Unilamellarity of Ladderane SUVs

We also performed experiments to confirm that our vesicles were indeed unilamellar. The protonophore gramicidin was added to the vesicle solution so that inserted into the outermost bilayer of the vesicles and dissipated the proton gradient. If vesicles are multilamellar, the gramicidin would only rapidly insert into the outermost bilayer, and some of the CF fluorescence will not rapidly decrease. On the other hand, if the vesicles are unilamellar, gramicidin will cause the CF fluorescence to rapidly decrease to the same level that is reached after the pH fully equilibrates. 20 µL of 100 µM gramicidin in ethanol was added to 4 mL of Buffer B in a fluorescence cuvette. **[5][3]PC** vesicles encapsulating CF were added, quickly mixed, and the fluorescence intensity at 515 nm was recorded. The fluorescence of the same volume of **[5][3]PC** vesicles without gramicidin in Buffer A was also measured in order to assess the extent of proton leakage. Vesicles were the lysed with 20 µL of 10% Triton-100X, and the fluorescence intensity was recorded in order to measure full pH equilibration. As shown in Supplementary Fig. S20, gramicidin causes rapid full influx of protons into the **[5][3]PC** vesicles, indicating that they are

indeed unilamellar. Further evidence of unilamellarity is provided by SAXS in Section 12.

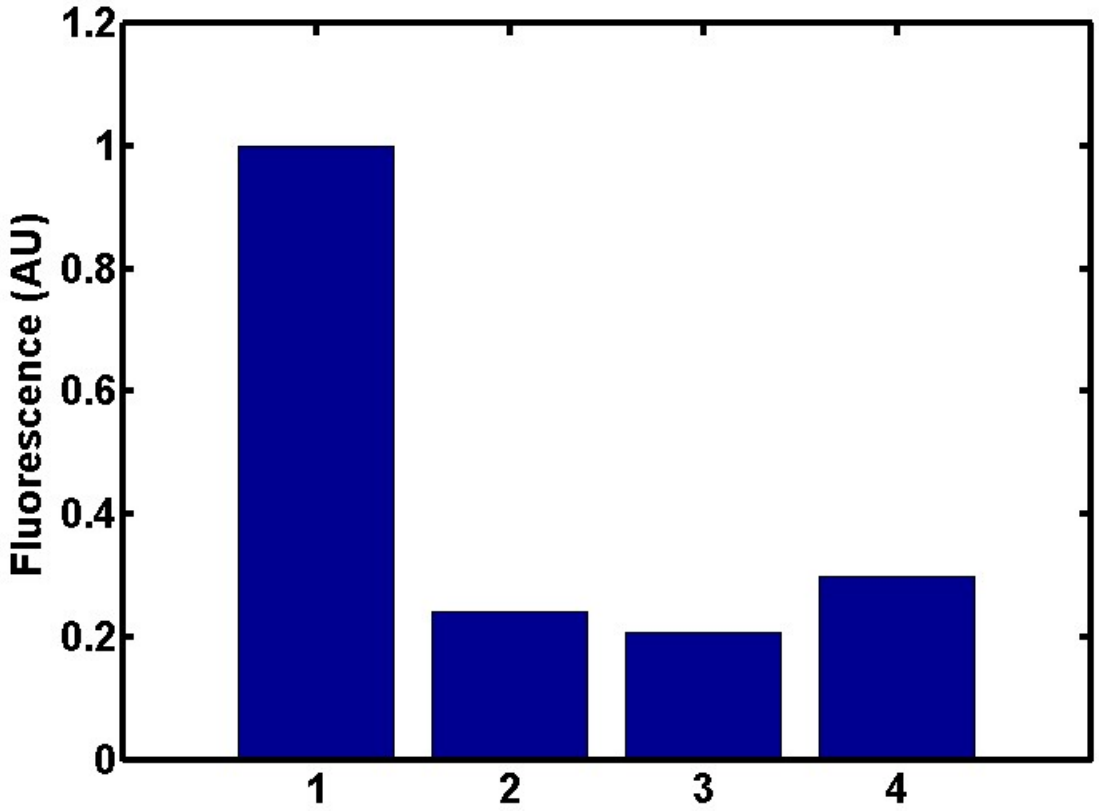

Supplementary Figure S20. pH equilibration in **[5][3]PC** SUVs encapsulating **CF** at pH = 7.2 spiked into pH = 5.8 buffer by transmembrane diffusion, Triton X-100 treatment and gramicidin treatment. 1) Initial fluorescence intensity, normalized to 1. 2) Fluorescence intensity after pH has fully equilibrated. 3) Fluorescence intensity after extravesicular gramicidin treatment. 4) Fluorescence intensity after Triton X-100 treatment. Fluorescence was measured seconds after mixing for conditions 2 and 3. Conditions 2, 3, and 4 show similar fluorescence decrease, indicating that they all result from full pH equilibration.

CF Leakage

It was confirmed that the decrease in CF fluorescence upon addition of SUVs encapsulating CF at pH = 7.2 to Buffer B at pH = 5.8 was due to proton/hydroxide transmembrane diffusion rather than CF leaking from SUVs with a simple dye leakage assay. Self-quenched CF at 25 mM in Buffer A or B was encapsulated in either POPC or **[5][3]PC** SUVs and separated from free dye via size exclusion chromatography as previously described. With a pK_a of 6.5, most of the CF molecules are doubly negatively charged in Buffer B and triply negatively charged in Buffer A. SUVs encapsulating CF in Buffer A or B were added to 4 mL of the same buffer, and the fluorescence was monitored for 10000 s. As dye diffuses out of the SUVs, it dequenches and the fluorescence signal increases. As shown in Supplementary Fig. S21, triply negatively charged CF leaks very slowly from SUVs made of both conventional phospholipids and ladderanes, with only 4-7% leaking during the course of even the longest pH equilibration assay (300 min.). On the other

hand, CF at pH = 5.8 leaks more rapidly, with a leakage half-life of 1747 s for **DOPC** SUVs, 1949 s for **[5][3]PC** SUVs, and 2841 s for **[3][3]PC** SUVs. It is not clear from these experiments if it is the doubly negatively charged CF or the small amounts of singly negatively charged and neutral CF that exist at equilibrium at pH = 5.8 that are the species leaking from the vesicles. Interestingly, CF at pH = 5.8 leaks 1.6 times more slowly from **[3][3]PC** SUVs than **DOPC** SUVs. Reduced transmembrane diffusion rates of small molecules across ladderane bilayers might be another biological function of ladderanes that was not previously hypothesized. The leakage of CF from the SUVs during the pH equilibration assays could affect the apparent rate of pH equilibration. As the leakage rate of CF at pH = 5.8 from SUVs of conventional PCs is much slower than the measured rate of pH equilibration, any effect on the measured pH equilibration rate would be very small. However, since the measured pH equilibration rate for ladderane SUVs is much slower and close to the rate of CF leakage at pH = 5.8, our measured pH equilibration rates may somewhat underestimate the true proton/hydroxide transmembrane diffusion rate. As CF only leaks at any appreciable rate at pH = 5.8 during the course of the pH equilibration assay, and the fluorescence of the doubly negatively charged CF should not change much when it leaks out of the vesicle into Buffer B, this effect should be small.

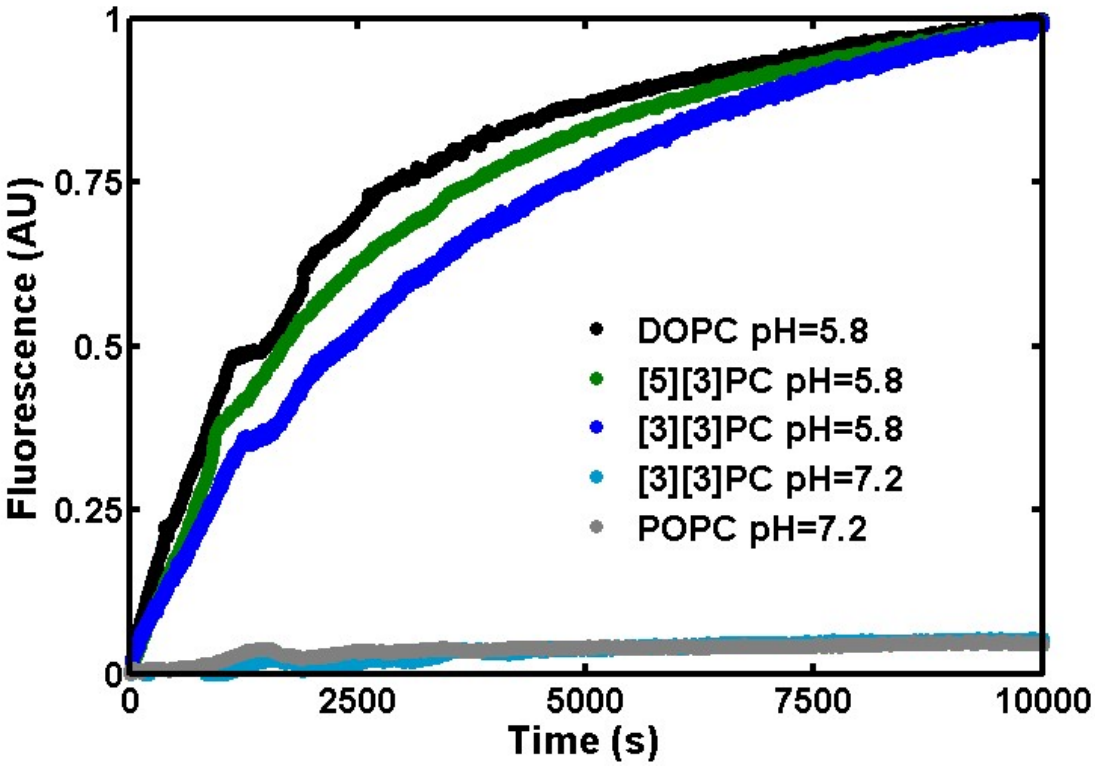

Supplementary Figure S21. CF leakage measured by fluorescence dequenching at pH = 7.2 and pH = 5.8, where CF is mostly triply negatively charged and doubly negatively, respectively.

pH Equilibration in SUVs Composed of a Mixture of Lipids

In order to further probe how ladderanes slow proton transmembrane diffusion and to examine a multicomponent bilayer, we also measured the transmembrane pH equilibration rate for an equimolar mixture of POPC and **[3][3]PC**. One might expect that the interactions between the ladderane motifs would be cooperative, and thus, the properties of bilayers composed of ladderane

PCs would be highly sensitive to the mol fraction of ladderane PCs. We tested this hypothesis by measuring the rate of transmembrane pH equilibration in SUVs composed of a 1:1 mixture of POPC and **[3][3]PC**. As shown in Supplementary Fig. S22, the rate of transmembrane pH equilibration falls halfway between those of POPC and **[3][3]PC**. This observation suggests that proton permeability scales linearly with **[3][3]PC** mol fraction and is not the result of cooperative interactions between ladderane motifs. This result also has implications for more complex membrane compositions. It demonstrates that pure, single-component ladderane bilayers are not required to achieve the low proton permeability we report in this work. While this two-component membrane is still very simple compared to the anammoxosome membrane, it shows that it is possible to increase the complexity of the membrane without sacrificing the physical effects of the ladderane PCs.

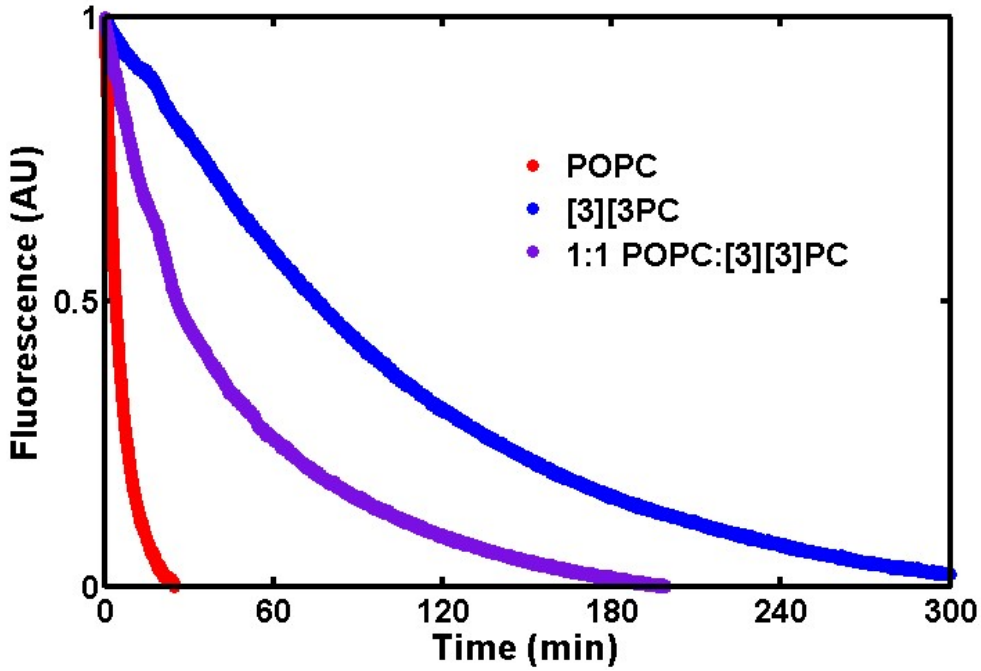

Supplementary Figure S22. pH equilibration in SUVs composed of POPC, **[3][3]PC**, and a 1:1 mixture of POPC and **[3][3]PC**. pH equilibration across 1:1 POPC:**[3][3]PC** bilayers occurs at a rate intermediate between pure POPC and pure **[3][3]PC** bilayers.

Correlation Between pH Equilibration Rates and Lateral Diffusion Rates

As shown in the main text, the pH equilibration rate deviates from the trend of conventional phospholipids when plotted vs. T_m. This indicates that the T_m does not reflect the intermolecular interactions that result in slow pH equilibration for ladderane SUVs vs conventional PC SUVs. On the other hand, the lipid lateral diffusion rates from FRAP measurements (see Supplementary Information Section 15) are approximately 10 times slower for ladderane SLBs than conventional PC SLBs. When the log of the pH equilibration $t_{1/2}$ is plotted vs. the lateral diffusion coefficient, both the ladderanes and conventional PCs appear to follow the same trend (Supplementary Fig. S23). This means that lipid lateral diffusion rates may more accurately report on the intermolecular interactions and lipid packing properties that affect proton/hydroxide transmembrane diffusion

rates.

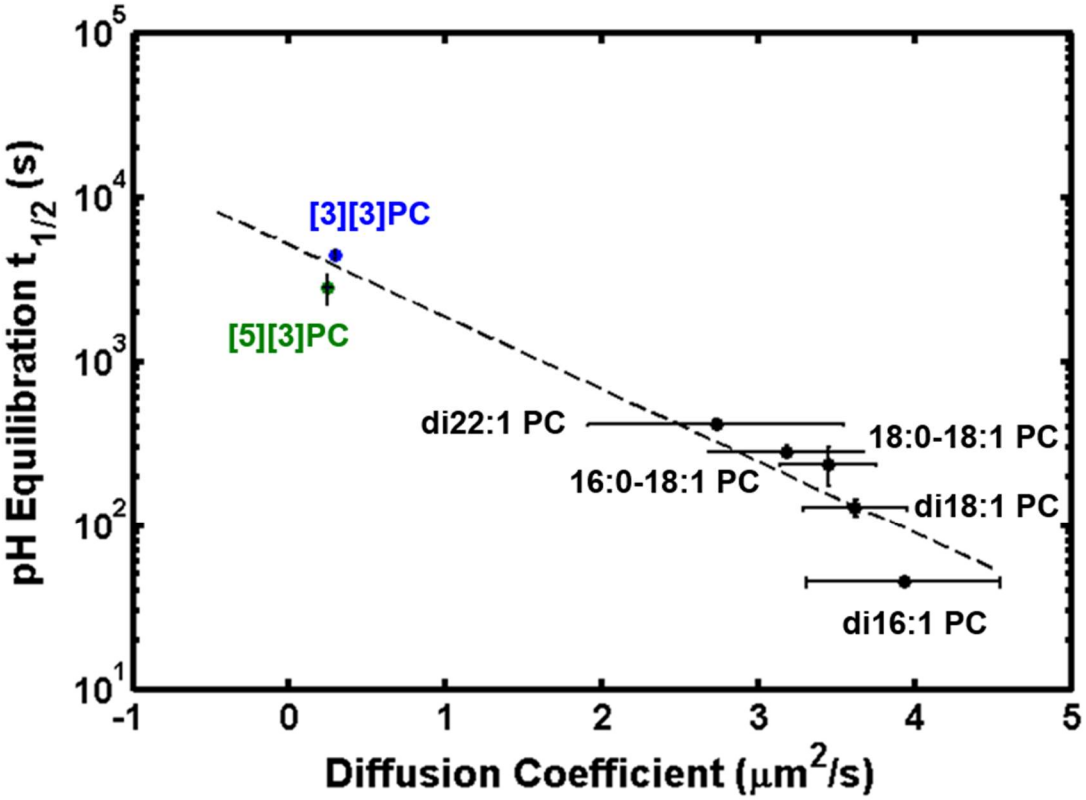

Supplementary Figure S23. Lateral diffusion of Oregon Green-DHPE correlates exponentially with pH equilibration $t_{1/2}$. This is consistent with the hypothesis that pH equilibration relies on the formation of water wires or protonated water clusters. Both formation of water wires/clusters and diffusion of lipids require breaking disrupting lipid-lipid interactions, and they correlated experimentally. Because they have much slower rates of transmembrane proton/hydroxide diffusion and lipid lateral diffusion, ladderanes appear to have stronger lipid-lipid interactions.

14. Pressure-Area Isotherms of Langmuir Monolayers

Langmuir pressure-area isotherms were recorded on a KSV NIMA KN 2002 (Biolin Scientific, Stockholm, Sweden) Langmuir trough equipped with a 273 cm^2 Teflon® trough and symmetric Delrin® barriers. Surface pressure was monitored with a Wilhelmy plate made of filter paper. 25 µL of lipids dissolved in chloroform at 1 mM were spread on the water subphase with a glass microsyringe, and the chloroform was allowed to evaporate for 10 minutes. The barriers were compressed at a rate of 10 mm/min at room temperature (22°C) while recording the surface pressure. Isotherms for each lipid were repeated at least three times to ensure reproducibility. Isothermal compressibility at 32 mN/m was calculated with Equation 2. 32 mN/m is chosen as the surface pressure at which to report MMAs and *C* because the molecular packing at this surface pressure approximates the molecular packing in conventional phospholipid bilayers.[23]

$$C = -\frac{1}{A}\left(\frac{dA}{d\Pi}\right)_T \quad (2)$$

A is the molecular area and Π is the surface pressure.

Lipid	T_m (°C) (Bilayer)	MMA at 32 mN/m	*C* at 32 mN/m
DSPC (di18:0)	57.1	45 ± 0.1	0.0056 ± 0.0003
DAPC (di20:0)	67.8	48 ± 3	0.0051 ± 0.0006
DLPC (di12:0)	-2.0	63 ± 2	0.0121 ± 0.0004
POPC (16:0/18:1)	-4.83	72 ± 2	0.0103 ± 0.0001
SOPC (18:0/18:1)	4.1	78 ± 2	0.0113 ± 0.008
DOPC (di18:1)	–10.9	70 ± 4	0.0128 ± 0.0007
di18:2 PC	–52.7	70 ± 1	0.0130 ± 0.0016
di16:1 PC	–33.1	74 ± 1	0.0114 ± 0.0004
DEPC (di22:1)	15.9	69 ± 2	NA
[3][3]PC	15.2	58 ± 3	0.0058 ± 0.0005
[5][3]PC	11.8	52 ± 1	0.0064 ± 0.0001

Supplementary Table S6. Mean molecular areas (MMAs) and compressibilities (*C*) of Langmuir monolayers at 32 mN/m. Uncertainties represent the standard deviations of three separate measurements.

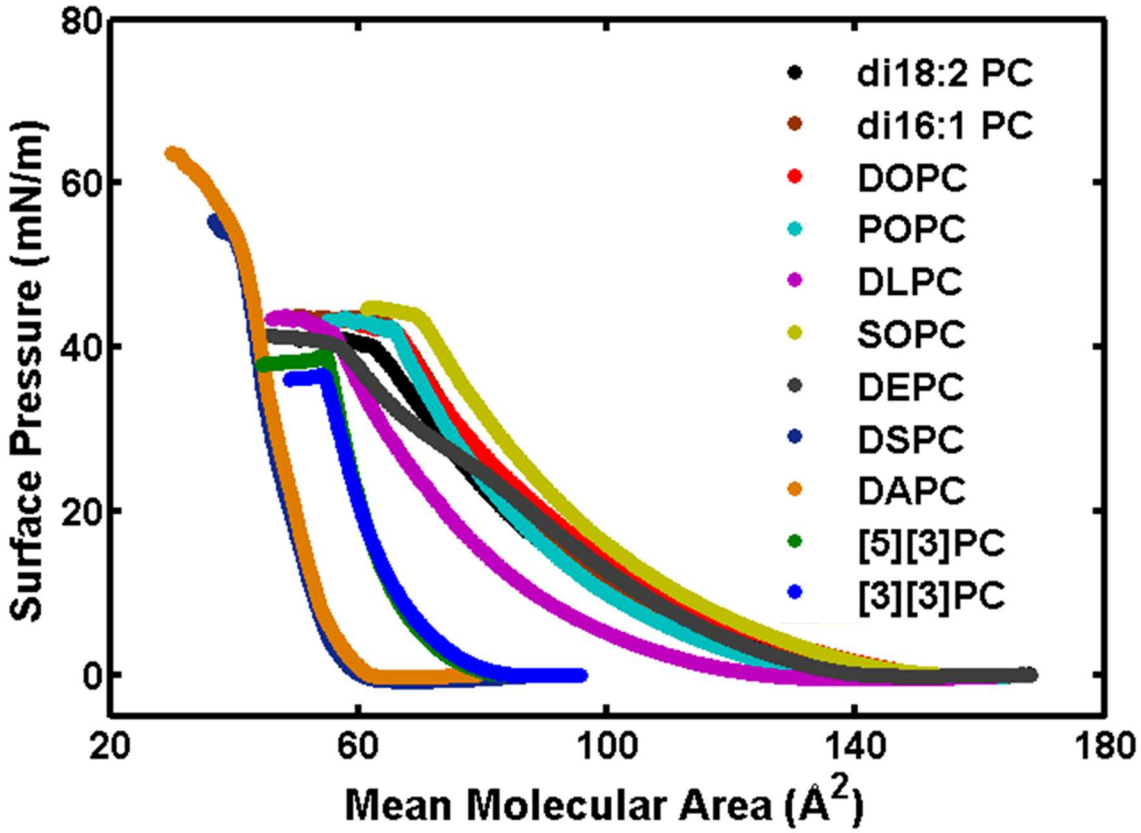

Supplementary Figure S24. Representative pressure-area isotherms of all lipids studied.

15. Fluorescence Recovery After Photobleaching (FRAP)

Supported lipid bilayers (SLBs) for fluorescence recovery after photobleaching (FRAP) experiments were formed by fusion of GUVs to clean glass. GUVs were formed by gentle hydration of lipid films (see Supplementary Information Section 7 for more details on formation of GUVs). Films of 100 nmol of each lipid with 0.1 mol% OG-DHPE were prepared in glass vials with the same procedure as preparing lipid films for gentle hydration. Lipid films were hydrated with 500 mM sucrose overnight at either 37º C or 70º C GUVs were formed by gentle hydration as described in the previous section. PDMS gaskets with holes punched in them were bonded to plasma-cleaned #1.5 glass coverslips. Solutions of GUVs mixed 1:1 with hydration buffer (240 mM NaCl, 10 mM NaH_2PO_4, pH = 7.4) were added to each well and incubated for 10 minutes. The wells were then rinsed thoroughly with water to remove excess vesicles. FRAP was performed on the same inverted microscope that was used to visualize GUVs. An aperture was used to rapidly bleach an approximately 20 μm spot on the SLB. Then, the fluorescence recovery was monitored by acquiring an image every 5 seconds, 10 seconds, 30 seconds, or 1 minute until fully recovered (see Supplementary Fig. S25). The frequency of image acquisition and light intensity was optimized for each lipid to minimize background photobleaching while acquiring enough data points for a good FRAP curve.

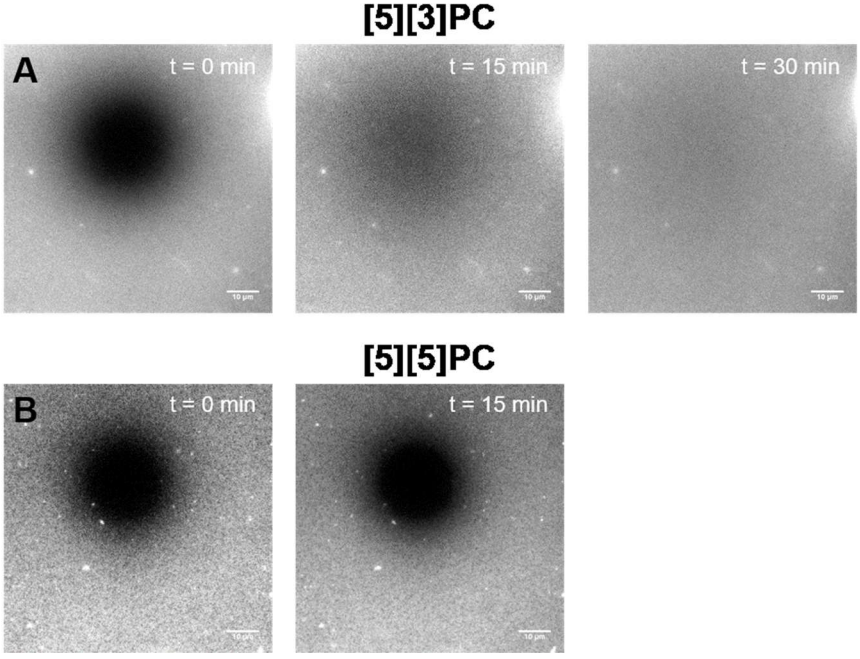

Supplementary Figure S25. Fluorescence recovery after photobleaching **[5][3]PC** and **[5][5]PC** SLBs. (A) The fluorescence has mostly recovered 15 minutes and completely recovered at 30 minutes for SLBs of the **[5][3]PC**. (B) No fluorescence is recovered in the bleached spot for the gel phase **[5][5]PC** after 15 minutes. All scale bars represent 10 μm.

In addition to monitoring the fluorescence within a bleached spot, fluorescence outside the bleached spot was monitored to correct for bleaching during the recovery period. The fluorescence

recovery was calculated according to Equation 3.[24]

$$I = \frac{I_{spot} - I_{background}}{I_{ref} - I_{backround}} \quad (3)$$

I_{spot} is the average intensity inside the bleached spot, $I_{background}$ is the average intensity inside the bleached spot immediately after full photobleaching (to account for background signal), and I_{ref} is the average intensity of a spot of the SLB outside the bleached area. The time to half recovery, $t_{1/2}$, was determined empirically by fitting the fluorescence recovery curves to the single exponential Equation 4.

$$I(t) = A(1 - \exp(-K * t)) \quad (4)$$

A is the mobile fraction. Then, $t_{1/2}$=ln(2)/K.

The diffusion coefficient of the dye in the SLB was calculated with Equation 5.

$$D = \frac{r_e^2}{4t_{1/2}} \quad (5)$$

D is the diffusion coefficient, r_e is the radius of the bleached spot, $t_{1/2}$ is the time to half fluorescence recovery, and r_e is the radius of the bleached spot.

16. Comparison to Biophysical Analyses of Ladderane Mixtures

Previously, Boumann, *et al*. characterized some of the physical properties of bilayers and monolayers of a mixture of PCs with a variety of ladderane and non-ladderane chains from an enrichment culture of anammox bacteria.[25] Langmuir monolayers and fluorescence anisotropy experiments indicated that lipids in this mixture were densely packed in monolayers and bilayers, but further analysis was complicated by the lack of pure ladderanes. As is often the case for lipid mixtures with a wide variety of molecular species, no phase transition is observed in the fluorescence polarization anisotropy experiments. In lipid mixtures, phase transitions are broadened until they are not easily observed. In this work, we measure the melting points of some of the major ladderane lipids in their mixture. We show that the most abundant natural ladderane lipids are fluid at room temperature, consistent with the finding that the PC extract is fluid at room temperature. Our extensive biophysical characterization also shows that ladderane bilayers are densely packed as is observed for the ladderane mixture with fluorescence anisotropy. Our FRAP and Langmuir monolayer work indicate that pure ladderane PCs also form dense bilayers, indicating that this property is not the result of a specific lipid mixture. Our Langmuir isotherms for **[5][3]PC** and **[3][3]PC** are qualitatively similar to the one previously published for the ladderane PC mixture. The MMAs and collapse pressures are similar for the pure ladderanes and mixture, but the compressibility appears to be higher for the mixture than pure ladderanes (approximately 0.009 vs. 0.006 mN/m). This difference is likely due to the presence of non-ladderane chains or lipid impurities in the ladderane PC fraction (anammox bacteria constitute approximately 75% of the bacterial culture employed in their study, and they estimate that the lipid purity is 85%). Structure-function relationships (especially with respect to thermotropic behavior) could also not be investigated in the ladderane mixture, while these relationships have been explored in our chemically defined system. Additionally, we have linked these physical properties to the proton permeability of lipid bilayers.

17. References

[1] Chen LL, Pousada M, Haines TH (1976) The Flagellar Membrane of *Ochromonas danica*: Lipid Composition. *J Biol Chem* 251(6):1835–1842.

[2] De Rosa M, Gambacorta A, Bu'Lock JD (1974) Effects of pH and Temperature on the Fatty Acid Composition of *Bacillus acidocaldarius*. *J Bacteriol* 117(1):212–214.

[3] Deinhard G, Saar J, Krischke W, Poralla K (1987) *Bacillus cycloheptanicus* sp. nov., a New Thermoacidophile Containing ω-Cycloheptane Fatty Acids. *System Appl Microbiol* 10(1):68–73.

[4] Sinninghe Damsté JS, Schouten S, Hopmans EC, van Duin ACT, Geenevasen JAJ (2002) Crenarchaeol: the characteristic core glycerol dibiphytanyl glycerl tetraether membrane lipid of cosmopolitan pelagic crenarchaeota. *J Lipid Res* 43(10):1641–1651.

[5] Pitcher A, Hopmans EC, Mosier AC, Park SJ, Rhee SK, Francis CA, Schouten S, Sinninghe Damsté JS (2011) Core and Intact Polar Glycerol Dibiphytanyl Glycerol Tetraether Lipids of Ammonia-Oxidizing Archaea Enriched from Marine and Estuarine Sediments. *Appl Env Microbiol* 77(10):3468–3477.

[6] Mercer JAM, Cohen CM, Shuken SR, Wagner AM, Smith MW, Moss FR, III, Smith MD, Vahala R, Goncalez-Martinez A, Boxer SG, Burns NZ (2016) Chemical Synthesis and Self-Assembly of a Ladderane Phospholipid. *J Am Chem Soc* 138(49):15845–15848.

[7] Johns MK, Yin MX, Conway SJ, Robinson DE, Wong LS, Bamert T, Wettenhall RE, Holmes AB (2009) Synthesis and biological evaluation of a novel cardiolipin affinity matrix. *Org Biomol Chem* 7(18):3691–3691.

[8] Sun M, Guo J, Yang Q, Xiao N, Li Y (2014) A new fluorescent and colorimetric sensor for hydrazine and its application in biological systems. *J Mater Chem B* 2:1846–1851.

[9] Paulick MG, Wise AR, Forstner MB, Groves JT, Bertozzi CR (2007) Synthetic Analogues of Glycophosphatidylinositol-Anchored Proteins and Their Behavior in Supported Lipid Bilayers. *J Am Chem Soc* 129(37):11543–11550.

[10] Patel KM, Morrisett JD, Sparrow JT (1979) The Conversion of Phosphatidylethanolamine into Phosphatidylcholine Labeled in the Choline Group Using Methyl Iodide, 18-Crown-6 and Potassium Carbonate. *Lipids* 14(6):596–597.

[11] Kong L, Yang JX, Chen QY, Zhang Q, Ke WD, Xue ZM, Zhou H, Wu JY, Jin BK, Tian YP (2014) Blue-shift of photoluminescence induced by coupling effect of a nanohybrid composed of fluorophore–phenothiazine derivative and gold nanoparticles. *J Nanopart Res* 16:2324–2335.

[12] Rodriguez N, Pincet F, Cribier S (2005) Giant vesicles formed by gentle hydration and electroformation: a comparison by fluorescence microscopy. *Colloids Surf B* 42(2):125-30.

[13] Lewis RN, Sykes BD, McElhaney RN (1988) Thermotropic phase behavior of model membranes composed of phosphatidylcholines containing cis-monounsaturated acyl chain homologues of oleic acid: differential scanning calorimetric and 31P NMR spectroscopic studies. *Biochem*istry 27(3):880-887.

[14] Silvius JR (1982) Thermotropic Phase Transitions of Pure Lipids in Model Membranes and Their Modifications by Membrane Proteins. *Lipid-Protein Interactions*, John Wiley & Sons, Inc., New York.

[15] Van der Star, W. R. L.; Dijkema, C.; de Waard, P.; Picioreanu, C.; Strous, M.; van Loosdrecht, M. C. M. An intracellular pH gradient in the anammox bacterium *Kuenenia stuttgartiensis* as evaluated by 31P NMR. *Appl. Microbiol. Biotechnol.* **2010**, ***86***, 311–317.

[16] MacDonald RC, MacDonald RI, Menco BP, Takeshita K, Subbarao NK, Hu LR (1991) Small-volume extrusion apparatus for preparation of large, unilamellar vesicles. *Biochim Biophys Acta* 1061(2):297-303.

[17] Smolsky IL, Liu P, Niebuhr M, Ito K, Weiss TM, Tsuruta H (2007) Biological small-angle X-ray scattering facility at the Stanford Synchrotron Radiation Laboratory. *J App Cryst* 40:S453-S458.

[18] Martel A, Liu P, Weiss TM, Niebuhr M, Tsuruta H (2012) An integrated high-throughput data acquisition system for biological solution X-ray scattering studies. *J Synchrotron Radiat* 19(Pt 3):431-434.

[19] Brzustowicz MR, Brunger AT (2005) X-ray scattering from unilamellar lipid vesicles. *J App Cryst* 38:126-131.

[20] Pabst G, Rappolt M, Amenitsch H, Laggner P (2000) Structural information from multilamellar liposomes at full hydration: full q-range fitting with high quality x-ray data. *Phys Rev E* 62(3 Pt B):4000–4009.

[21] Koyanagi T, Leriche G, Onofrei D, Holland GP, Mayer M, Yang J (2016) Cyclohexane Rings Reduce Membrane Permeability to Small Ions in Archaea-Inspired Tetraether Lipids. *Angew Chem Int Ed* 55(5):1890–1893.

[22] Schroeder TBH, Leriche G, Koyanagi T, Johnson MA, Haengel KN, Eggenberger OM, Wang CL, Kim YH, Diraviyam K, Sept D, Yang J, Mayer M (2016) Effects of Lipid Tethering in Extremophile-Inspired Membranes on H^+/OH^- Flux at Room Temperature. *Biophys J* 110(11):2430-2440.

[23] Stottrup BL, Stevens DS, Keller SL (2005) Miscibility of ternary mixtures of phospholipids and cholesterol in monolayers, and application to bilayer systems. *Biophys J* 88(1):269–276.

[24] Kang M, Day CA, Kenworthy AK, DiBenedetto E (2012) Simplified equation to extract diffusion coefficients from confocal FRAP data. *Traffic* 13(12):1589–1600.

[25] Boumann HA, Longo ML, Stroeve P, Poolman B, Hopmans EC, Stuart MCA, Sinninghe Damsté JS, Schouten S (2005) Biophysical properties of membrane lipids of anammox bacteria: I. Ladderane phospholipids form highly organized fluid membranes. *Biochim Biophys Acta* 1788(7):1444–1451.